DEVELOPMENT AND VALIDATION OF POLARIMETRIC-MCSCENE 3D ATMOSPHERIC RADIATION MODEL

PHASE I FINAL TECHNICAL REPORT

Prepared by
Alexander Berk, Fred Hawes, and Marsha Fox
Spectral Sciences, Inc.
4 Fourth Avenue
Burlington, MA 01803-3304

Principal Investigator: Dr. Alexander Berk

Prepared for
Office of Science
U.S. Department of Energy
1000 Independence Ave.
Washington, DC 20585-1290

Under Phase I Contract No. DE-SC0013984

March 2016

TABLE OF CONTENTS

LIST OF FIGURES

SUMMARY

Polarimetric measurements can substantially enhance the ability of both spectrally resolved and single band imagery to detect the proliferation of weapons of mass destruction, providing data for locating and identifying facilities, materials, and processes of undeclared and proliferant nuclear weapons programs worldwide. Unfortunately, models do not exist that efficiently and accurately predict spectral polarized signatures for the materials of interest embedded in complex 3D environments. Having such a model would enable one to test hypotheses and optimize both the enhancement of scene contrast and the signal processing for spectral signature extraction.

The Phase I set the groundwork for development of fully validated polarimetric spectral signature and scene simulation models. This has been accomplished

1. by (a) identifying and downloading state-of-the-art surface and atmospheric polarimetric data sources, (b) implementing tools for generating custom polarimetric data, and (c) identifying and requesting US Government funded field measurement data for use in validation;
2. by formulating an approach for upgrading the radiometric spectral signature model MODTRAN to generate polarimetric intensities through (a) ingestion of the polarimetric data, (b) polarimetric vectorization of existing MODTRAN modules, and (c) integration of a newly developed algorithm for computing polarimetric multiple scattering contributions;
3. by generating an initial polarimetric model that demonstrates calculation of polarimetric solar and lunar single scatter intensities arising from the interaction of incoming irradiances with molecules and aerosols;
4. by developing a design and implementation plan to (a) automate polarimetric scene construction and (b) efficiently sample polarimetric scattering and reflection events, for use in a to be developed polarimetric version of the existing first-principles synthetic scene simulation model, MCScene; and
5. by planning a validation field measurement program in collaboration with the Remote Sensing and Exploitation group at Sandia National Laboratories (SNL) in which data from their ongoing polarimetric field and laboratory measurement program will be shared and, to the extent allowed, tailored for model validation in exchange for model predictions under conditions and for geometries outside of their measurement domain.

1. INTRODUCTION

1.1 Overview

Multi- and Hyper-Spectral Imaging (MSI/HSI) is an invaluable tool for detecting the proliferation of weapons of mass destruction, providing data for locating and identifying facilities, materials, and processes of undeclared and proliferant nuclear weapons programs worldwide. The basic concept is straightforward; effluent gases and surface contaminants generated in processing of nuclear materials exhibit unique spectral signatures. Spectral detection of incongruously located storage containers and/or facility operations can also provide clues to covert activities. These signatures can, in principle, be extracted directly from the infrared (IR) and visible (VIS) spectral imagery. The difficulty is that signal strength is often weak, or signatures are hard to distinguish from the ambient background. Contrast is increased and the extraction process enhanced, especially for man-made objects and perturbed backgrounds, by analyzing the polarimetric components of MSI/HSI data. Unfortunately, there are no radiative transfer (RT) models that efficiently and accurately predict spectral channel polarized signal radiances, *i.e.*, the vector Stokes parameters, for materials of interest within complex 3D environments. Having such a model would enable one to test hypotheses and optimize both the enhancement of scene contrast and the signal processing for spectral signature extraction.

Developing a 3D polarization model for generating accurate, synthetic MSI/HSI data cubes is challenging due to the large number of model components that must be vectorized, optimized for processing speed, validated against measured data, and integrated into a cohesive toolkit (see Figure 1). One must build models for generating molecular and particulate (cloud / aerosol) optical data that feed into the RT algorithm. One must also generate structurally and physically accurate 3D environmental components including detailed ground surface topography, temperature maps and angular reflectances/emissivities, and a wide range of embedded objects such as water clouds, gas plumes, and faceted vehicles and buildings.

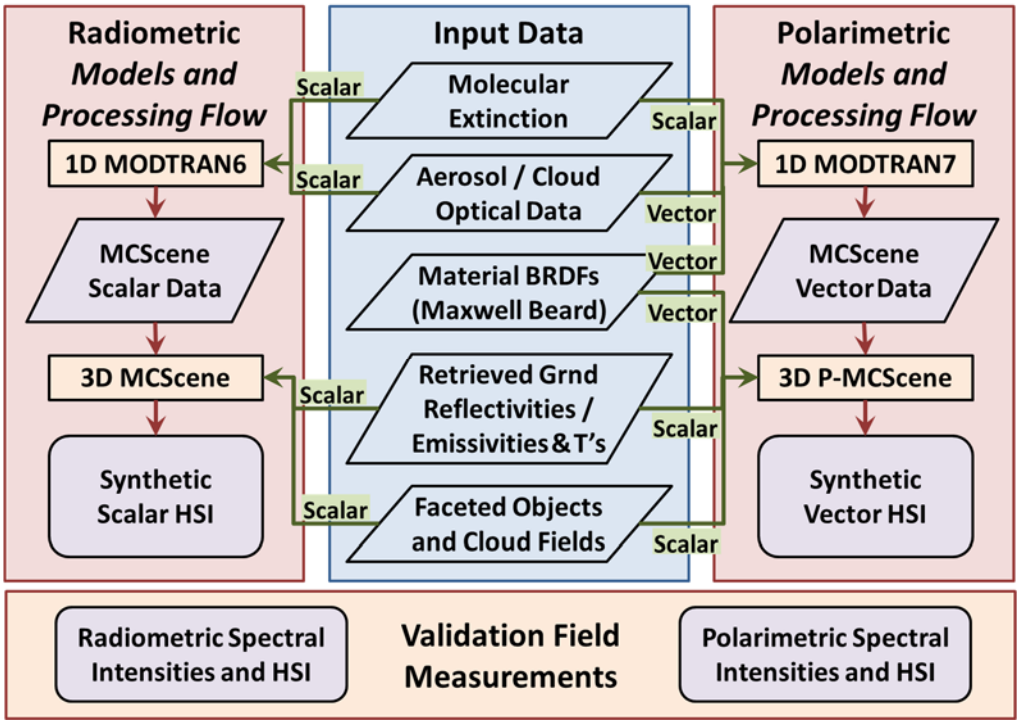

Figure 1. Evolution from 1D and 3D Radiometric (left) to Polarimetric (right) Models. Inputs, processing, and predictions must all be vectorized and validated.

In response to these requirements, Spectral Sciences, Inc. (SSI) proposes to develop P-MCScene, a validated, polarimetric 3D simulation capability. This will be accomplished by generalizing SSI's Monte-Carlo (MC) based synthetic Scene simulation model, MCScene [Richtsmeier *et al.*, 2001; 2004] to include calculation of all 4 Stokes components. The radiometric MCScene model already generates accurate synthetic MSI/HSI radiance data cubes, providing full thermal plus solar spectral coverage (0.2 – 500 μm) and modeling spherical Earth geometry; 3D cloud fields; natural terrain and turbid water backgrounds; chemical plumes; day, night, and twilight conditions; and both man-made and natural materials/objects. MC photon trajectories are tracked, summing radiance contributions at randomly sampled atmospheric scattering and surface reflection points along multiple-segmented lines-of-sight (LOS's). MCScene vectorization will require introducing polarimetric surface and particulate models and upgrading to polarimetric RT.

The innovative MCScene approach invokes first-principles radiative physics to generate spectral channel radiances without requiring computationally prohibitive and RAM demanding on-the-fly monochromatic spectral sampling. This feature, which is equally applicable in the polarimetric regime, is critically important for modeling HSI systems. The spectral coverage of typical visible through short-wave (Vis/SWIR) HSI sensors spans > 20,000 cm^{-1}. Monochromatic (line-by-line, LBL) calculations would require tens of thousands of spectral polarimetric images to construct a synthetic HSI data cube; MCScene directly computes a single image for each spectral channel.

MCScene utilizes databases generated by the US government-standard band model RT algorithm, MODTRAN®[1] [Berk *et al.*, 2016], to characterize spectral channel optical properties. For this reason, MODTRAN7, a polarimetric version of MODTRAN6, will also be developed as part of the SBIR effort to generate the vectorized optical data that MCScene will require to model polarimetric signatures and to provide polarimetric spectral signatures for verification of MCScene simulations. MODTRAN6 [Berk *et al.*, 2016] is an Air Force Research Laboratory (AFRL) funded mixed Fortran 95/2003 and C/C++ language modernization of MODTRAN, which includes, modular partitioning, improved I/O schemes (API, GUI, JSON), line-by-line (LBL) and parallel computing options, and automated coupling to the NASA scattering codes for computing custom aerosol/cloud optical data [Mishchenko and Travis, 1998]. This NASA code will be utilized to generate the vectorized particulate optical data.

Validation of MODTRAN7 and P-MCScene is vital to a successful program. Colleagues in the Remote Sensing and Exploitation (RSE) group at Sandia National Laboratories (SNL) were contacted both to discuss leveraging their existing Vis/SWIR polarimetric measurement program to provide validation data and to coordinate mutually beneficial future measurement and modeling activities. In addition, SSI has contacted Dr. Joao Romano at the US Army Armament Research, Development and Engineering Center ARDEC and Dr. Tom Caudill at AFRL to discuss access of their thermal IR (TIR) measurement data. Dr. Romano worked in collaboration with the Army Research Laboratory on a 24/7/365 field program designed to measure target variability due to weather, diurnal, and seasonal changes. Dr. Caudill led an effort to measure material polarimetric Bidirectional Reflectance Distribution Functions (pBRDFs) in the laboratory and subsequently measure and model spectral signatures of these materials placed in the field. These collections of polarimetric measurements provide a wealth of potential validation data.

The Phase I effort focused on gathering relevant polarimetric databases and on initiating MODTRAN7 development. A design and implementation plan for P-MCScene was generated. Validation field measurements were planned. The Phase II effort will culminate with the development of validated MODTRAN7 and P-MCScene polarimetric models.

[1] The MODTRAN trademark is being used with express permission of the owner, the United States of America, as represented by the United States Air Force.

Anticipated Public Benefits

Numerous significant benefits will arise from the successful completion of the proposed Phase II development and Phase III product commercialization of MODTRAN7 and P-MCScene. These include technical, economic, social, and national security benefits. The technical benefit pertains to the development of greatly improved physics-based models and software tools to support the design and development of polarimetric optical sensors and their associated analysis algorithms for remote sensing applications. The economic benefit pertains to the potential time and cost savings that can be realized when sensor requirements and candidate designs can be rapidly and accurately evaluated using sensor/scenario simulation tools. The social benefit pertains to an improved capability to identify and monitor potential WMD production activities and facilities. Tools developed under this program will enable design of improved sensors for WMD facilities monitoring. This in turn will provide our national decision makers and military commanders with more accurate and timely assessments of the status of our adversaries' WMD programs. The technology developed under this SBIR program will be of direct benefit to all commercial and Federal Government groups involved in the design and development of polarimetric optically-based remote sensors for virtually any application, most notably, surveillance.

1.2 Program Objectives

The overall objective of this effort was to provide tools for generating accurate polarimetric LOS spectral radiances and polarimetric synthetic MSI/HSI data cubes. Phase I was designed to set the groundwork for vectorizing MODTRAN6 and MCScene, demonstrating a clear pathway to the ultimate Phase II goal of fully validated polarimetric models. The specific Phase I tasks were to

6. assess the accuracy and applicability of current available polarimetric databases;
7. formulate the approach for upgrading MODTRAN6 to compute polarization;
8. integrate polarimetric-MODTRAN4 (MODTRAN4P) components into P-MODTRAN6;
9. develop a design and implementation plan for P-MCScene; and
10. plan a validation field measurement program.

Each of these tasks were successfully completed, as detailed in Section 2: Phase I Work.

Questions to be answered by the Phase I effort were:

1. Which MODTRAN4P strategies, routines and data are applicable to MODTRAN7?
2. What changes to MCScene and its MODTRAN-generated databases are needed to accommodate polarization?
3. What is the availability of polarimetric aerosol and surface data?
4. All results and findings from the Phase I effort are described in this final report.

2. PHASE I WORK

The work under this Phase I program was performed at SSI in Burlington, MA. The Phase I work plan consisted of 5 major tasks that mirrored the Phase I technical objectives. The Phase I deliverable is this final report. Before delving into the description of the individual tasks, a short review of polarization is provided to motivate the effort, and the scalar models that are being vectorized to model the full set of Stokes parameters are described.

Review of Polarization

A light beam consists of packets of photons, each of which defines a pair of perpendicular plane waves, (E_x, E_y) oriented orthogonal to the direction of propagation. The light is characterized by the amplitudes of the plane waves and their relative phase shift. The decomposition of the wave into orthogonal components can be defined for any set of perpendicular planes containing the photon propagation direction. By convention, the terrestrial atmosphere meridian (vertical) plane of propagation is defined to contain E_x and the perpendicular plane of propagation contains E_y. The light is *unpolarized* if the time averaged amplitudes are equal and the phase shift varies randomly.

Amplitudes and the relative phase shift cannot be measured directly. Instead Stokes intensity parameters, related to the square of the amplitudes, specify polarization state. The Stokes parameters are a column 4-vector of intensities, $[I, Q, U, V]^T$, that fully characterizes the light. The first element, I, is the total light intensity as measured by standard radiometers or interferometers. The second and third elements define the linear polarization, with Q being the excess of vertically polarized intensity over horizontally polarized intensity and U being the excess of 45º linearly polarized intensity over 135º linearly polarized intensity. The circular polarization, V, is the excess of right circularly polarized intensity over left circularly polarized intensity. These components and a standard measurement strategy are illustrated in Figure 2. In this figure, the green and white striped trapezoids represent perfect linear polarizers, which only transmit the light wave in a specific orientation. As the figure illustrates, the total intensity equals the sum of the vertically and horizontally transmitted light. The Q intensity is a measurement of the signed difference between these components. Rotating the polarizers by 45º enables measurement of U. Circular polarization is measured by transmitting light through ±45º retarders. Retarders transmit light of one orientation faster than the perpendicular orientation, providing directional indices of refraction.

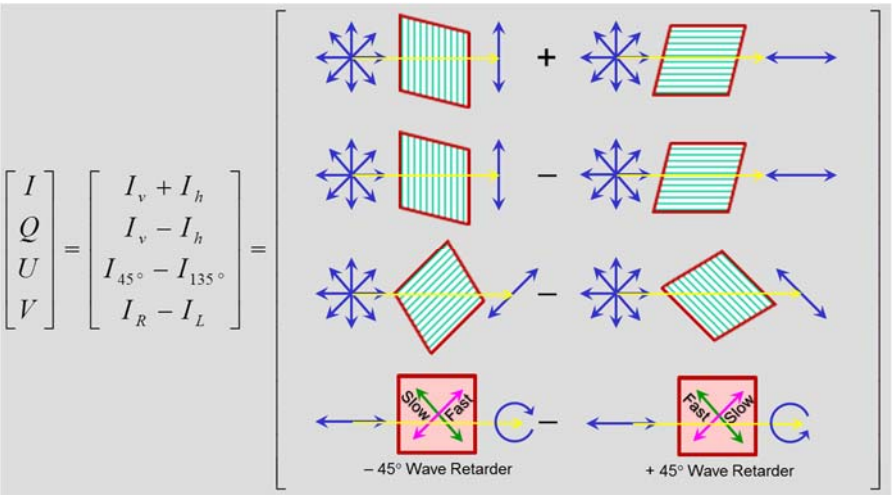

Figure 2. Stokes Components and Measurement Strategy.

An Overview of MODTRAN and its Treatment of Surface Reflectance/Emission and Atmospheric Scatter

The primary sources of ambient radiation in the ambient atmosphere, the top-of-atmosphere (TOA) solar irradiance and most atmospheric and bottom of atmosphere (BOA) thermal emission, are unpolarized, with a Stokes vector of the form $[I, 0, 0, 0]^T$. Light becomes polarized in the terrestrial environment predominantly by undergoing a surface reflection or an atmospheric scattering event [Thermal emissions from smooth surfaces (water bodies and many man-made materials) can also be polarized, and lunar irradiances that arise from reflection of solar irradiances by the moon's surface are linearly polarized]. Fresnel specular reflections off surfaces produce distinct parallel (p) and perpendicular (s, from the German *senkrecht*) polarized components. Here, parallel denotes the electric field component in the plane containing the reflected photon and the surface normal; the perpendicular electric field is orthogonal to that plane. When an atmospheric scattering event occurs, the intensity of light in the scattering plane, defined to contain the incident and scattering ray, differs from the electric field intensity perpendicular to the scattering plane. Since surface reflections and atmospheric scattering are the primary sources of polarization in the terrestrial atmosphere, vectorizing the MODTRAN and MCScene radiometric models requires that the modeling of these interactions be upgraded to determine the polarimetric state of the products. The next two sub-sections provide a brief description of the MODTRAN and MCScene models, highlighting their approaches to computing scalar surface reflection and atmospheric scatter.

The current (March 2015) public release version of MODTRAN, MODTRAN5.4, solves the atmospheric radiative transfer equation (RTE) to determine path transmittances, radiances and fluxes using a statistical band model approach. This is to be distinguished from monochromatic (line-by-line, LBL) algorithms which solve the RTE at one spectral frequency at a time. The LBL algorithms provide the highest fidelity, but thousands, or even tens of thousands, of spectral points need to be considered within each 1 cm^{-1} frequency bin when spectral band results are required. These calculations are painstakingly slow, especially if scattered radiances are to be modeled.

The MODTRAN band model avoids the time-consuming monochromatic calculations by statistically representing the true temperature and pressure dependent distribution of molecular transitions in a spectral band (0.1, 1.0, 5.0, or 15.0 cm^{-1} wide). The MODTRAN pseudo distributions are defined to contain n_s randomly distributed strong lines of strength S_s and n_w randomly distributed weak lines of strength S_w. A pictorial representation is provided in Figure 3. A formula [Plass 1958; 1960] expresses the transmittance arising from the collection of randomly distributed identical lines.

MODTRAN defines the atmosphere via molecular, aerosol and cloud vertical profiles above a locally spherical Earth surface. Built-in (aerosol and cloud) particulate models, and latitude and season dependent atmospheres, are provided to facilitate general calculations. For more detailed analysis, options are provided to insert radiosonde data, and user-defined particulate densities and optical properties. MODTRAN5.4 also introduces modeling of localized gas (chemical) clouds, based on an SBIR effort funded by DOE [Contract No. DE-FG02-08-ER85132]. Optical data for the local cloud is derived from the Pacific Northwest National Laboratory (PNNL) Infrared Spectral Library IRSL [Sharpe *et al.*, 2004].

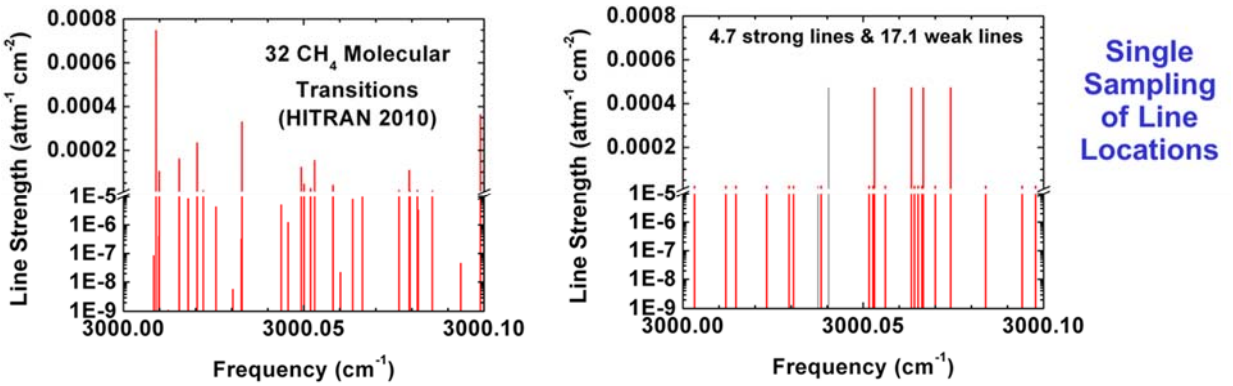

Figure 3. (left) The 32 Methane Molecular Transitions from the HITRAN [Rothman *et al.*, 2009; 2013] Data Base at 296 K and 0.1 atm Pressure. (right) MODTRAN statistically represents this distribution as arises from 4.7 randomly distributed strong lines of strength 0.0005 cm^{-2}/atm and 17.1 randomly distributed weak lines of strength 0.00002 cm^{-2}/atm. The actual transition frequencies on the right were chosen randomly for illustrative purposes; MODTRAN does not assign line positions.

Scattering is most accurately modeled using the DISORT N-Stream discrete ordinate model developed by K. Stamnes and co-workers [Stamnes *et al.*, 1988; 2000]. DISORT provides a first-principles solution to the plane-parallel atmosphere RTE. MODTRAN includes a statistical Correlated-*k* (C*k*) algorithm, which recasts the band model calculations into a handful of weighted monochromatic calculations; this is necessary because DISORT is a monochromatic model. The standard DISORT algorithm is modified significantly for integration into MODTRAN. In particular, DISORT plane-parallel atmosphere single scatter solar and thermal emitted radiances are replaced with the MODTRAN spherical refractive geometry values. Furthermore, DISORT line-of-sight radiance outputs have been replaced by segment radiances, which are defined for each of MODTRAN's spherical refraction path segments. These modifications are necessary to fit the DISORT plane-parallel "peg" into the MODTRAN spherical refractive "hole".

SSI recently completed a major overhaul and modernization of MODTRAN, culminating with the delivery of MODTRAN6 [Berk *et al.*, 2016] to AFRL in February 2016. MODTRAN6 retains the full functionality of MODTRAN5.4. As illustrated in Figure 4, the new model provides a modular partitioning of the software utilizing mixed Fortran 95/2003 and C/C++ code. The core model remains in Fortran; C/C++ is introduced to provide an Application Program Interface (API) for MATLAB, Python, IDL, Fortran and C/C++ third party software. A graphical user interface (GUI) and a JavaScript Object Notation (JSON) based text input option facilitates running of MODTRAN. A MODTRAN toolbox includes utilities for generating day-of-year and latitude/longitude based atmospheres, and for generating custom aerosol or cloud models. The latter tool, illustrated in Figure 5, uses NASA's software [Mishchenko *et al.*, 2002] to generate MODTRAN compatible optical data for homogeneous spherical (Mie) and more general axisymmetric particles. Either radiometric or polarimetric data can be generated. An MPI (Message Passing Interface) tool enables the parallel execution of several instances of MODTRAN with stepped values of the input parameters, for problem space sweeping calculations. In addition, a LBL capability has been integrated into MODTRAN [Berk *et al.*, 2016] to facilitate validation of the statistical band model approach and to enable the highest spectral resolution modeling. The new software documentation includes a detailed user-manual, an Algorithm Theoretical Basis Document (ATBD), source code information generated with ROBODoc® (https://rfsber.home.xs4all.nl/Robo/), and an Interface Control Document (ICD). MODTRAN6 serves as the reference scalar model from which polarimetric MODTRAN (MODTRAN7) will be generated.

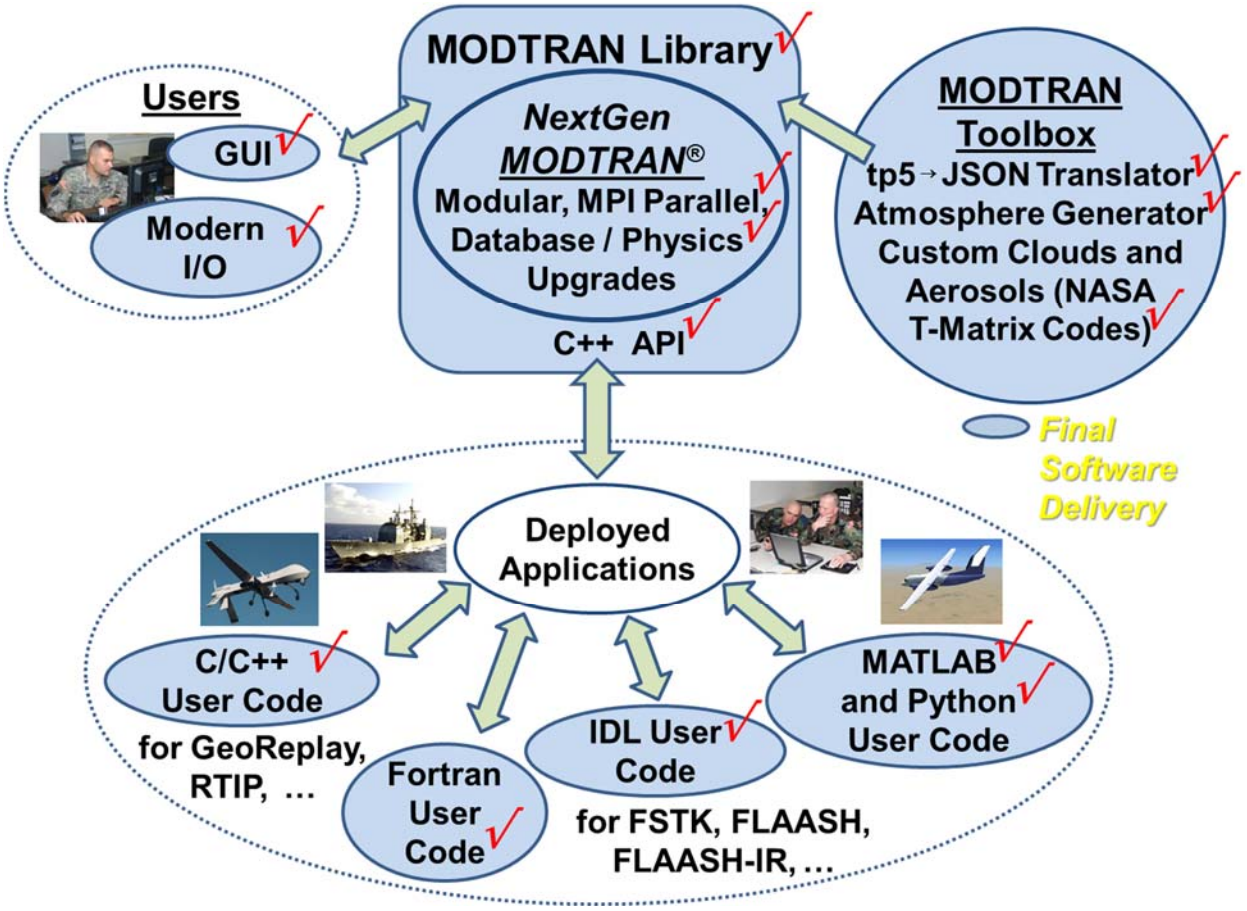

Figure 4. MODTRAN6 Software.

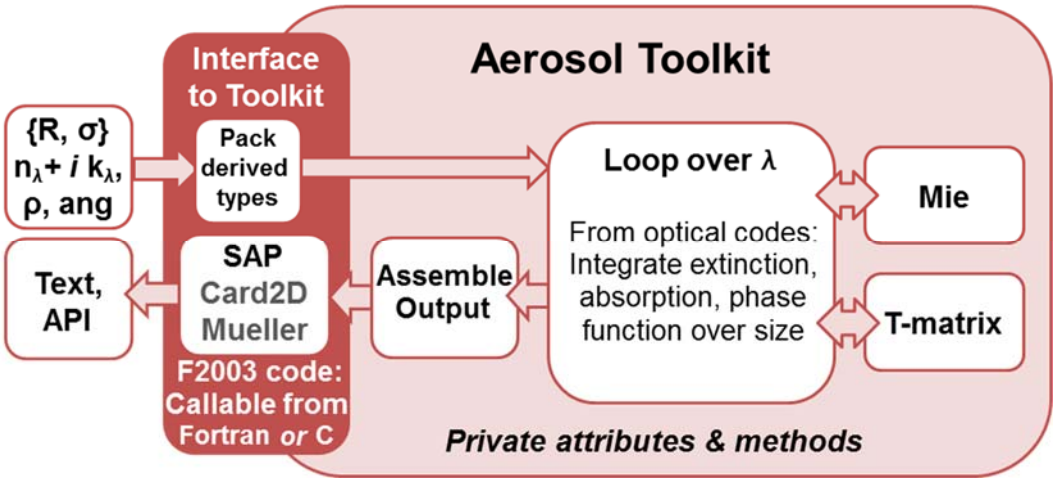

Figure 5. MODTRAN6 Software.

MODTRAN includes the ability to model terrain Bi-direction Reflectance Distribution Functions (BRDFs). The empirical, azimuthally averaged BRDF models provide an analytic expression for the distribution of reflected rays for any given incident direction. Many of the models partition the reflected radiance into specular and volumetric components, as illustrated in Figure 6. As seen in this figure, the specular components include not only incident rays directly reflected into the atmosphere, but also multiple reflections off the roughened surface. The volumetric component describes the photons that reflect back into the atmosphere only after entering the surface medium. The BRDF analytic expressions are used to compute the surface reflected direct solar irradiance and the directional emissivity transmitted directly to the sensor. DISORT is used to model the diffusely scattered radiation that reaches a sensor of interest. Fourier expansions in relative azimuth angle of the parameterized terrain BRDFs must be generated for integration into the DISORT algorithm.

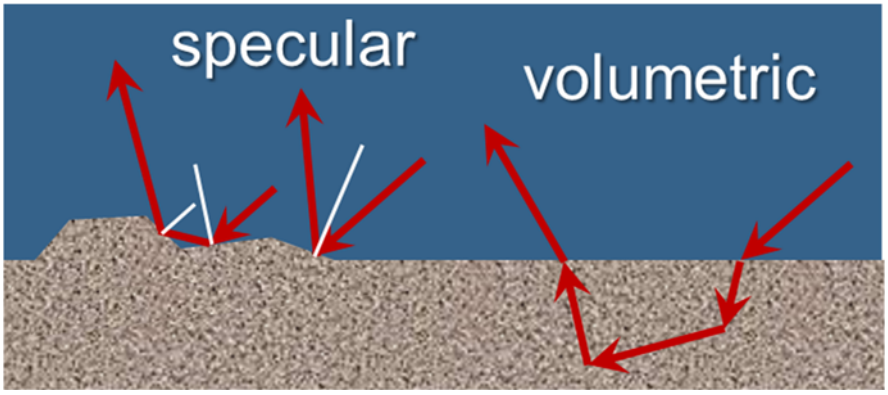

Figure 6. Specular and Volumetric BRDF Components. White lines represent surface normal. Specular incident and reflected angles are equal. Snell's Law dictates the transmitted angles for volumetric scattering.

Atmospheric scatter by particles is modeled in scalar MODTRAN by specifying extinction and absorption coefficients [1/km] and scattering phase functions which define the distribution of scattering angles. Tabulated phase functions that depend on scattering angle are required for modeling single scatter solar radiances. Multiple scatter solar and all thermal scatter are modeled by scalar DISORT, which requires that the phase function be represented in a Legendre expansion. In MODTRAN6, the Legendre expansion of the built-in aerosols is approximated using the Henyey-Greenstein scattering phase function [Henyey and Greenstein, 1941] in which the n^{th} order Legendre expansion coefficient simply equals the asymmetry factor to the n^{th} power (the asymmetry factor is the integral over 4 pi steradians of the product

of the scattering phase function and the cosine of the scattering angle). This simplification can lead to errors, as described in Section 2.3.1. MODTRAN users are provided the option to define their own aerosol or cloud data. In the most general method for specifying particulate properties, dubbed the Spectral Aerosol Profile (SAP) option, spectral extinction and absorption coefficients, and spectral phase function data, are entered as functions of altitude.

Both the surface reflection/emission and the atmospheric scattering models of scalar MODTRAN must be vectorized for MODTRAN7. However, the current capabilities provide a good basis for the polarimetric extension.

An Overview of MCScene and its Treatment of Surface Reflectance/Emission and Atmospheric Scatter

The Monte-Carlo Scene (MCScene) simulation software [Richtsmeier *et al.*, 2001; 2004] was developed to generate state-of-the-art synthetic Hyper- and Multi-Spectral Imagery (HSI/MSI) data as an adjunct to measurement data and to provide fully characterized "ground truth". First-principles 3D radiative transfer computes both solar and thermal regime (visible through far-infrared, FIR) radiance maps. In the Direct Simulation Monte-Carlo (DSMC) algorithm, the integrand from the integral form of the RTE is smartly sampled to compute line-of-sight radiances. Separate calculations are performed for each sensor pixel and spectral channel (bandpass). Calculation of spectral band radiances is performed without requiring explicit spectral sampling of molecular absorption; instead, photon trajectories are appropriately weighted using a MODTRAN generated database of spectral channel molecular transmittances.

MCScene images are generated with sensor and solar geometry, atmospheric and aerosol profiles, sensor instantaneous and total field-of-view (FOV), and the number of simulated photon trajectories per pixel all defined by the user. Surface reflectance and emissivity data are derived from MSI/HSI imagery that has been atmospherically corrected. Surface topography is modeled from imported digital elevation maps (DEMs). Any number of faceted embedded objects, such as vehicles and buildings, can be inserted into the MCScene simulation.

Sample MCScene RGB images are illustrated in Figure 7. On the left is a nadir-viewing image of Anna Maria Island and the Robinson Preserve in Tampa, FL; the surface reflectance map was derived from AVIRIS data using FLAASH atmospheric correction [Perkins *et al.*, 2012]. The voxelized cumulus cloud field was retrieved [Adler-Golden *et al.*, 2012] from Landsat data. On the right is a horizon-viewing image of Woomera, Australia; the surface reflectance map and the cirrus cloud (with 8 km base height and maximum optical depth of 2) are both Landsat-derived data products.

The MCScene approach is further detailed in Figure 8. In the reverse propagation DSMC technique, "photons" are launched into the MCScene solution region (nominally, a cube with 50 km sides) from the sensor in a sensor pixel viewing direction. A scattering optical depth τ is set to $-\ln(\beta)$, where β is a random number between 0 and 1. The photon can leave the solution region through the TOA (forbidden for the first leg of the trajectory), scatter within the atmosphere, or hit a surface. When a scattering or surface event occurs, solar and thermal radiance contributions are summed. The contributions include both a scattering albedo weight and a spectral channel molecular absorption weight that accounts for molecular attenuation. Next, a new direction is determined by sampling either the surface BRDF or the scattering phase function. A new scattering optical depth is chosen and the process repeated until the photon either leaves the solution region or its trajectory weight falls below a pre-selected minimum. Biasing and trajectory weighting (also known as importance sampling) preferentially select the most pertinent trajectories. For example, trajectories originating from the solar direction are favored when modeling solar radiances. Side exits are prevented by assuming reflective boundary conditions above a polygonal Earth (similar to a droxtal but with many more sides). The reflective boundary conditions enable horizon and twilight modeling, as illustrated on the right in Figure 7.

Figure 7. MCScene Synthetic RGB Imagery. (left) Nadir simulation of a Landsat derived cloud field inserted above Tampa Bay, FL; North points to the top in the image, and the Easterly sun casts shadows towards the West. (right) Horizon image of Woomera, Australia with a Landsat derived cloud field.

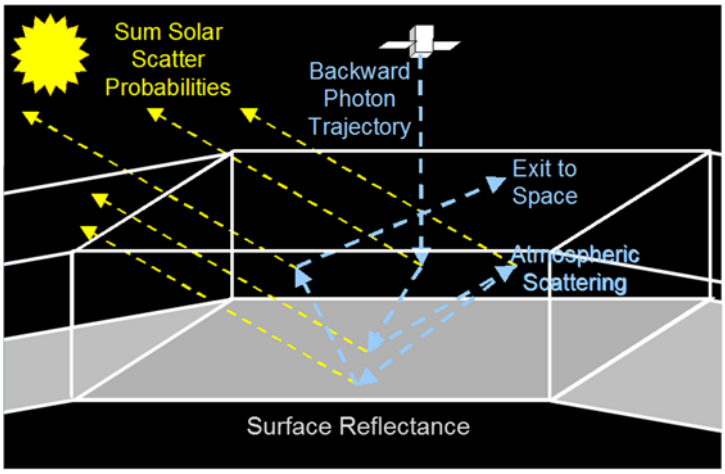

Figure 8. MCScene Reverse Propagation Direct Simulation Monte Carlo (DSMC) Photon Propagation.

The surface parameterized BRDF model in MCScene is rudimentary. A sinusoidal Walthall form [Berk *et al.*, 2016] for the BRDF was introduced into MCScene specifically to facilitate the Monte-Carlo sampling that determines the reflected zenith angle; the chosen BRDF form is easily analytically integrated. Polarization modeling will require a physics-based BRDF model and a method for assigning BRDF data to each surface pixel. Currently, surface pixels are only characterized by their surface topography, their spectral reflectance or emissivity, and their solar illuminated and shaded temperatures (for thermal modeling only).

Modeling of molecular (Rayleigh) scattering within the Monte-Carlo framework is straightforward due to the simple form of the Rayleigh scattering phase function. Scattering by aerosols and clouds within scalar MCScene is modeled with either Henyey-Greenstein or tabulated Mie normalized scattering phase functions. The advantage of the Henyey-Greenstein (HG) form is that it is easily sampled to determine a scattering angle. One can select a random number β between 0 and 1, and then analytically integrate the HG scattering phase function to determine the scattering angle Θ at which the integral from 0 to Θ exactly equals β.

Sampling of scattering phase functions to determine scattering angle is computationally much more time intensive when applied to Mie (spherical) particles. The tabulated Mie phase functions may vary with both altitude and spectral channel, and often exhibit very sharp forward peaks. To accelerate the sampling process, MCScene pre-computes a basis set of endmember phase functions using the Sequential Maximum Angle Convex Cone (SMACC) endmember extraction technique [Gruninger *et al.*, 2004]. Each tabulated Mie scattering phase function is represented as a non-negative linear combination of the basis set functions, which number between 10 and 20. For each of the endmembers, the mapping from random number between 0 and 1 to scattering angle is pre-defined. During the actual DSMC processing, the sampling is quick. One random number is chosen to determine which basis function to use (based on the abundancy coefficients), and a second random number maps to the scattering angle for that endmember phase function. When modeling polarization, the scattering phase function still dictates the angular distribution of scattered photons. Thus, the scalar MCScene method for determining scattering angle will be applicable to the vector code.

2.1 Assess Current Polarimetric Databases

The objective of this task was to assess current polarimetric data. The proposal focused on evaluating the availability and quality of polarimetric particulate data, the data required to model scattering and emission by atmospheric aerosols, clouds, smokes, etc. The decade old polarimetric version of MODTRAN, MODTRAN4P, was designed to compute only atmospheric polarization. The Air Force Research Laboratory (AFRL) requirement was to define the hemisphere of atmospheric polarimetric radiance impingent on a flat plate [Fetrow *et al.*, 2002]. AFRL had measured LWIR polarimetric Bidirectional Reflectance Distribution Functions (pBRDFs) for a large number of materials in a controlled laboratory setting. These materials were subsequently observed in field measurements. The role of the MODTRAN4P software was to define the polarimetric sky radiance impingent on the materials of interest. The goal of the AFRL program was to evaluate the fidelity of the parameterized pBRDF when the material plates were placed in the field.

The goals of our DOE program are very different. While MODTRAN7 and P-MCScene themselves are to model atmospheric scatter and emission, the primary focus of this effort is modeling of reflection and emission from the Earth background and targets located within that background. Costs and logistics associated with field measurements limit the range of conditions and geometries over which surface materials can be measured. The high fidelity polarimetric models being developed under this program will provide accurate predictions under conditions of interest for which measurements are unavailable. As a first step, the models must be able to ingest and process both parameterized surface polarimetric-BRDF (pBRDF) and particulate polarimetric data. Subsequent validation will require direct comparison to polarimetric scene measurements. The following sub-sections describe the form, availability and extent of existing polarimetric surface, particulate and field measurement data that can be used by MODTRAN7 and P-MCScene.

2.1.1 Surface Polarimetric Bi-directional Reflectance Distribution Function (pBRDF) Parameterizations

The goals of this sub-task were to determine (1) the state-of-the-art in pBRDF modeling and (2) the availability of pBRDF data. The Lambertian treatment of surface reflectance, which models all reflected rays as equally probable, is adequate for many radiometric applications, but the reflected radiance and thermal emission from a Lambertian surface are, by definition, unpolarized.

2.1.1.1 Material BRDF Models

Established material BRDF models include Torrance-Sparrow (TS) [Torrance and Sparrow, 1967], Maxwell-Beard (MB) [Maxwell *et al.*, 1973], and Priest-Meier (PM) [Priest and Meier, 2002]. All of these models partition the BRDF into specular and volumetric components as illustrated in Figure 6. The original MB and PM BRDFs both include polarimetric forms; the TS BRDF was generalized to include polarization for a measurement program sponsored by the US Air Force [Fetrow *et al.*, 2002].

The PM BRDF models surface reflections as arising from an angular distribution of micro-facets. The facet distribution approach provides a measure of surface roughness. Shell [Shell, 2005] illustrated that both the polarized TS and a modified MB BRDF can also be formulated in terms of micro-facets. This is important because polarization is introduced into radiometric BRDF models by substituting the specular scalar Fresnel reflection term with the full Fresnel Mueller matrix. The pBRDF parameterizations typically ignore any polarization that may arise from volumetric reflections. In general, the Fresnel equations describe the specular reflection and refractive transmittance of light across a plane separating media with distinct complex indices of refraction. The polarization state of a Fresnel (specular) reflected incident beam is defined as follows [Stamnes and Stamnes, 2015]:

$$\begin{pmatrix} I \\ Q \\ U \\ V \end{pmatrix}_{ref} = \mathbf{R}_{\tilde{n}_1 \Rightarrow \tilde{n}_2}(\beta) \begin{pmatrix} I \\ Q \\ U \\ V \end{pmatrix}_{in} \; ; \tag{1a}$$

$$\mathbf{R}_{\tilde{n}_1 \Rightarrow \tilde{n}_2}(\beta) \equiv \begin{bmatrix} \tfrac{1}{2}\left(|R_s|^2 + |R_p|^2\right) & \tfrac{1}{2}\left(|R_s|^2 - |R_p|^2\right) & 0 & 0 \\ \tfrac{1}{2}\left(|R_s|^2 - |R_p|^2\right) & \tfrac{1}{2}\left(|R_s|^2 + |R_p|^2\right) & 0 & 0 \\ 0 & 0 & \mathrm{Re}\left(R_s R_p^*\right) & \mathrm{Im}\left(R_s R_p^*\right) \\ 0 & 0 & -\mathrm{Im}\left(R_s R_p^*\right) & \mathrm{Re}\left(R_s R_p^*\right) \end{bmatrix} \; , \tag{1b}$$

where the perpendicular R_s and parallel R_p Fresnel reflectance coefficients are defined by the equations

$$R_s \equiv R_s(\beta; \tilde{n}_1, \tilde{n}_2) = \frac{\tilde{n}_1 \cos\beta - \tilde{n}_2 \sqrt{1 - n_1^2 \sin^2\beta / n_2^2}}{\tilde{n}_1 \cos\beta + \tilde{n}_2 \sqrt{1 - n_1^2 \sin^2\beta / n_2^2}} \; ; \tag{2a}$$

$$R_p \equiv R_p(\beta; \tilde{n}_1, \tilde{n}_2) = \frac{\tilde{n}_1 \sqrt{1 - n_1^2 \sin^2\beta / n_2^2} - \tilde{n}_2 \cos\beta}{\tilde{n}_1 \sqrt{1 - n_1^2 \sin^2\beta / n_2^2} + \tilde{n}_2 \cos\beta} \; . \tag{2b}$$

Here β is the angle of incidence relative to the normal of the surface microfacet, $\tilde{n}_1 = n_1 + i\,\kappa_1$ is the complex index of refraction of the incident ray medium and $\tilde{n}_2 = n_2 + i\,\kappa_2$ is the complex index of refraction of the transmitted ray medium.

2.1.1.2 Maxwell-Beard (MB) Polarimetric BRDF Model

There seems to be little evidence to suggest that the physics of any of the three parameterized pBRDF models (polarized TS, modified MB or PM) is superior to the other two. However, the modified MB pBRDF has one major advantage: a spectral database [Shell, 2005] of over 400 materials has been developed using the MB form. Before describing that database, Shell's expression for the microfacet modified MB pBRDF is presented. As noted earlier, the parameterized pBRDFs contain both specular and volumetric components:

$$\mathbf{F}_{MB} = \mathbf{F}_{MB}^{spec} + \mathbf{F}_{MB}^{vol} = \frac{\mathbf{R}_{\tilde{n}_1 \Rightarrow \tilde{n}_2}(\beta)}{4\mu_i \mu_r} p(\mu_N)\, S_{MB}(\beta, \mu_N) + \mathbf{F}_{MB}^{vol}. \quad \textbf{(3)}$$

In this equation, μ_N is the cosine of the microfacet surface normal angle; as before, β is the angle of incidence relative to the normal of the surface microfacet; and μ_i and μ_r are the cosines of the angles of incidence and reflectance, respectively, relative to the orientation of the *macrofacet*. One can easily derive an equation defining β in terms of μ_i, μ_r and the relative azimuth angle $\Delta\phi$. Let $\hat{\mathbf{s}}_i$ and $\hat{\mathbf{s}}_r$ be both *outward* incident and reflected direction unit vectors. Then

$$\cos(2\beta) = \hat{\mathbf{s}}_i \bullet \hat{\mathbf{s}}_r = \mu_i\ \mu_r + \sqrt{\left(1-\mu_i^2\right)\left(1-\mu_r^2\right)}\cos\Delta\phi \quad \textbf{(4a)}$$

One can also derive a relationship defining μ_N in terms of β, μ_i and μ_r. Let $\hat{\mathbf{s}}$ be the macrofacet unit normal from which the three cosines, μ_N, μ_i and μ_r are all defined. Let $\hat{\mathbf{s}}_N$ be the microfacet unit normal, and for the incident and reflected rays. Since the reflection is specular, $\hat{\mathbf{s}}_N$ must equal the normalized sum of $\hat{\mathbf{s}}_i$ and $\hat{\mathbf{s}}_r$. Taking the dot product with $\hat{\mathbf{s}}$ yields the following relationship

$$\hat{\mathbf{s}}_N = \frac{\hat{\mathbf{s}}_i + \hat{\mathbf{s}}_r}{\sqrt{2\left(1 + \hat{\mathbf{s}}_i \bullet \hat{\mathbf{s}}_r\right)}} \quad \Rightarrow \quad \hat{\mathbf{s}} \bullet \hat{\mathbf{s}}_N = \frac{\hat{\mathbf{s}} \bullet \hat{\mathbf{s}}_i + \hat{\mathbf{s}} \bullet \hat{\mathbf{s}}_r}{\sqrt{2 + 2\cos(2\beta)}} \quad \Rightarrow \quad \mu_N = \frac{\mu_i + \mu_r}{2\cos\beta} \quad \textbf{(4b)}$$

Together, Eqs. (4a) and (4b) verify that the MB pBRDF is indeed only a function of μ_i, μ_r and $\Delta\phi$. The Fresnel Mueller matrix, $\mathbf{R}_{\tilde{n}1 \Rightarrow \tilde{n}2}$, is normalized by the 4 μ_i μ_r term. The microfacet angular probability distribution function, $p(\mu_N)$, is represented with either a Gaussian (G) or Cauchy (C) distribution:

$$p_G(\mu_N) = \frac{B}{2\pi\sigma^2\mu_N^3}\exp\left(-\frac{1-\mu_N^2}{2\mu_N^2\sigma^2}\right) \quad or \quad p_C(\mu_N) = \frac{B\,\mu_N}{\mu_N^2\sigma^2 + 1 - \mu_N^2} \quad \textbf{(5)}$$

Here σ is a surface roughness parameter and B is a bias parameter. The Maxwell-Beard masking function, S_{MB}, corrects for self-shadowing and occultation:

$$S_{MB}(\beta, \mu_N) = \frac{1 + \arccos\mu_N \exp(-2\beta/\tau)/\Omega}{1 + \arccos\mu_N/\Omega} \quad \textbf{(6)}$$

The parameters τ and Ω are chosen to improve the overall fit of the pBRDF. As noted above, the volumetric reflectance is modeled as unpolarized:

$$\mathbf{F}_{MB}^{vol} = \begin{pmatrix} \rho_D + \dfrac{2\rho_V}{\mu_i + \mu_r} & 0 & 0 & 0 \\ 0 & 0 & 0 & 0 \\ 0 & 0 & 0 & 0 \\ 0 & 0 & 0 & 0 \end{pmatrix}. \quad \textbf{(7)}$$

This term contains both a diffuse (Lambertian) component parameter, ρ_D, and a volumetric scattering parameter, ρ_V.

2.1.1.3 The Nonconventional Exploitation Factors (NEF) Data System

Parameters for the modified MB pBRDF have been measured for over 400 materials, and collected into the Nonconventional Exploitation Factors (NEF) Data System. Although this is a limited distribution database, SSI does have the latest version and has used it in previous US Government efforts. Very little open literature information is available on the database; however, public release information is included in the Shell dissertation. The description here is limited to the information available from that document.

The NEF Data System groups their materials into 12 classes: asphalt, brick, camouflage, composite, concrete, fabric, water, metal, paint, rubber, soil, and wood. The $\mathbf{F}_{MB}$ parameters are typically measured as five laser wavelengths: 0.325, 0.6328, 1.06, 3.39, and 10.6 μm. Sample data for a white paint is shown in Table 1. All the parameters from the generalized MB pBRDF are listed plus the Directional Hemispherical Reflectance, ρ'_{DHR}:

$$\rho'_{DHR}(\mu_i,\phi_i) = \int_0^1 \left[\int_0^{2\pi} f_{11}^{macro}(\mu_i,\phi_i;\mu_r,\phi_r)\, d\phi_r \right] \mu_r\, d\mu_r \quad . \tag{8}$$

Here μ_i (μ_r) equals the cosine of θ_i (θ_r), respectively, and both ρ'_{DHR} and the scalar BRDF, f_{11}, are spectral functions, but the wavelength dependence has been suppressed for notational simplicity. The NEF Data System provides higher resolution spectral data for the Directional Hemispherical Reflectance at a fixed angle of incidence for use in spectrally interpolating the scalar BRDF.

Table 1. NEF Data System Parameters for a Sample White Paint.

Sample	λ [μm]	n	κ	B	σ	τ	Ω	ρ_D	ρ_V	ρ'_{DHR}
White Paint	0.352	1.5810	0.0685	0.0040	0.0035	78.21	0.6125	3.279e-3	2.201e-3	0.0358
	0.6328	1.5150	0.1122	0.0222	0.0079	0.1345	1.459	0.3638	-0.05010	0.9756
	1.06	1.4960	0.1169	0.0306	0.0081	0.1710	1.483	0.3761	-0.04860	1.0300
	3.39	1.6270	0.1345	0.0011	0.0015	43.55	1.847	1.307e-4	6.875e-5	0.0064
	10.6	1.5990	0.1568	0.0007	0.0013	752.9	343.9	3.992e-4	2.343e-4	0.0071

The complex index of refraction spectral curve, $\tilde{n}_\lambda = n_\lambda + i\ \kappa_\lambda$, for each material in the NEF Data System is required to define the spectral Maxwell-Beard pBRDF, $\mathbf{F}_{\mathrm{MB}}(\lambda)$, since the scalar-to-vector transformation is based on knowing the Fresnel Mueller matrix, $\mathbf{R}_{1 \Rightarrow \tilde{n}\lambda}$. One approach to obtaining the index of refraction spectral curves is to simply interpolate the laser wavelength data. Certainly, the dimensionless extinction coefficients, κ_λ, in solids do not vary spectrally as drastically as molecular gas extinction data. However, measurements of refractive indices at finer spectral resolution are encouraged. In the end, the role of MODTRAN7 and P-MCScene is to provide a mechanism to model polarimetric signatures given the best available material data. The simulation models will provide the capability to input high spectral resolution indices of refraction when that data is available, but they will also interpolate coarse spectral resolution data when necessary.

There is another issue regarding use of the NEF Data System to describe polarimetric BRDFs. The primary focus of the database development has been characterization of scalar BRDFs. Polarimetric measurements may have been used to derive some of the BRDF parameters. For example, the material indices of refraction are often determined from Brewster angle measurements; the Brewster angle is the reflection angle at which the parallel (p) reflected intensity is at a minimum. However, it is somewhat disconcerting that the polarimetric BRDF is being defined without explicitly requiring measurements of the polarimetric response; instead it is being computed by mapping the Fresnel scalar response to the Fresnel Mueller matrix. As noted in the previous paragraph, the primary role of MODTRAN7 and P-MCScene is to model material polarimetric signatures given the best available data. This discussion simply points to the fact that higher quality polarimetric BRDF measurements are warranted.

2.1.1.4 Utilization of MODTRAN7 and P-MCScene to Refine Parameterized pBRDFs

MODTRAN7 and P-MCScene will enable refinement of pBRDF characterizations. Discrepancies between simulated results and direct measurements can be used to correct pBRDF parameterizations. This is especially true in controlled (laboratory) environments, where measurement conditions are well characterized. Furthermore, the proposed Phase II MODTRAN7 effort includes an option to model the

material sub-surface. This capability will enable MODTRAN to calculate the polarimetric state of volumetric reflections and thereby improve the current pBRDF parameterizations.

2.1.1.5 Surface Polarimetric Emission

All the discussion in this section has thus far focused on the surface reflected polarimetric signature. Fresnel emission from a flat surface is polarized with distinct parallel and perpendicular components:

$$\begin{pmatrix} I_p \\ I_s \\ U \\ V \end{pmatrix}_{em} \equiv \tfrac{1}{2} \begin{pmatrix} I+Q \\ I-Q \\ U \\ V \end{pmatrix}_{em} = \begin{pmatrix} 1-\left|R_p(\beta)\right|^2 \\ 1-\left|R_s(\beta)\right|^2 \\ 0 \\ 0 \end{pmatrix} B_\lambda(T) = \begin{pmatrix} \varepsilon_p(\beta) \\ \varepsilon_s(\beta) \\ 0 \\ 0 \end{pmatrix} B_\lambda(T) \quad . \tag{9}$$

Here, $B_\lambda(T)$ is the Planck blackbody emission at wavelength λ and temperature T. On the right in the above equation, parallel and perpendicular emissivities, $\varepsilon_p(\beta)$ and $\varepsilon_s(\beta)$, have been introduced, which depend on the emission angle β relative to the surface normal, and on the complex indices of refractive of the two media (not labeled). Generalizing to the MB surface, the parallel and perpendicular emissivities must be defined for each microfacet:

$$\varepsilon_p(\mu;\beta) = \int_0^1 \left\{ \int_0^{2\pi} \left[\frac{\left|R_p(\beta)\right|^2}{4\mu\,\mu'} p(\mu_N)\, S_{MB}(\beta,\mu_N) + \frac{\rho_D}{2} + \frac{\rho_V}{\mu+\mu'} \right] d\phi' \right\} \mu'\, d\mu' , \tag{10a}$$

$$\varepsilon_s(\mu;\beta) = \int_0^1 \left\{ \int_0^{2\pi} \left[\frac{\left|R_s(\beta)\right|^2}{4\mu\,\mu'} p(\mu_N)\, S_{MB}(\beta,\mu_N) + \frac{\rho_D}{2} + \frac{\rho_V}{\mu+\mu'} \right] d\phi' \right\} \mu'\, d\mu' \tag{10b}$$

Here, μ is the cosine of the macrofacet emission zenith angle. To compute the macrofacet thermal emission Stokes vectors, the I_p and I_s components from each microfacet must be rotated into the macrofacet reference plane. This will create non-zero I_p, I_s, and U components. For the MB surface, the distribution of microfacets is assumed to be azimuthally symmetric. Since principal plane mirror imaged facets produce U components of opposite signs, only the I_p and I_s thermal emission Stokes components will be non-zero after integrating over the distribution of microfacets. Here a difference between MODTRAN7 and P-MCScene arises. The ground in MODTRAN is always modeled as flat or horizontal. Thus, the MODTRAN7 surface emissions will only contain I_p and I_s (equivalently, I and Q) components. That is not true with MCScene, which imports digital elevation maps to describe the surface topography. With a reference meridian plane, MCScene surface emissions will include non-zero I, Q, and U components.

2.1.2 Aerosol and Cloud Data

In radiometric (scalar) models, particulate scattering and absorption are characterized by spectral extinction and scattering cross-sections, $\beta_e \equiv \beta_e(\mathbf{r})$ and $\beta_s \equiv \beta_s(\mathbf{r})$, respectively [units of area], and by spectral normalized scattering phase functions $f(\mathbf{r}, \Theta)$ [sr^{-1}], as in the upper left in Figure 9. In these expressions, $\mathbf{r}$ is a position vector, and Θ is the scattering angle between incident and scattered directions. Although the cross-sections and the phase function are spectrally varying, the spectral label has been suppressed for notational simplicity. The normalized scattering phase function defines the angular distribution of scattered radiation. A path length ℓ integral over the product of the extinction [scattering] cross-section and the particulate density $\rho(\mathbf{r})$ defines the particulate spectral extinction [scattering] optical depth $\tau_e \equiv \tau_e(\mathbf{r}_0 \rightarrow \mathbf{r}_L)$ [$\tau_s \equiv \tau_s(\mathbf{r}_0 \rightarrow \mathbf{r}_L)$] for a path of length L:

$$\tau_e(\mathbf{r_0} \to \mathbf{r}_L) = \int_0^L \beta_e(\mathbf{r}_\ell)\rho(\mathbf{r}_\ell)\, d\,\ell \quad and \quad \tau_s(\mathbf{r_0} \to \mathbf{r}_L) = \int_0^L \beta_s(\mathbf{r}_\ell)\rho(\mathbf{r}_\ell)\, d\,\ell \quad , \tag{11}$$

where $\mathbf{r}_\ell$ is the position vector a distance ℓ along the line-of-sight (LOS). The particulate transmittance t_v falls off exponentially with optical depth:

$$t_e = \exp(-\tau_e) \quad and \quad t_s = \exp(-\tau_s) \quad . \tag{12}$$

The dependence of transmittance on position has been omitted for notational simplicity.

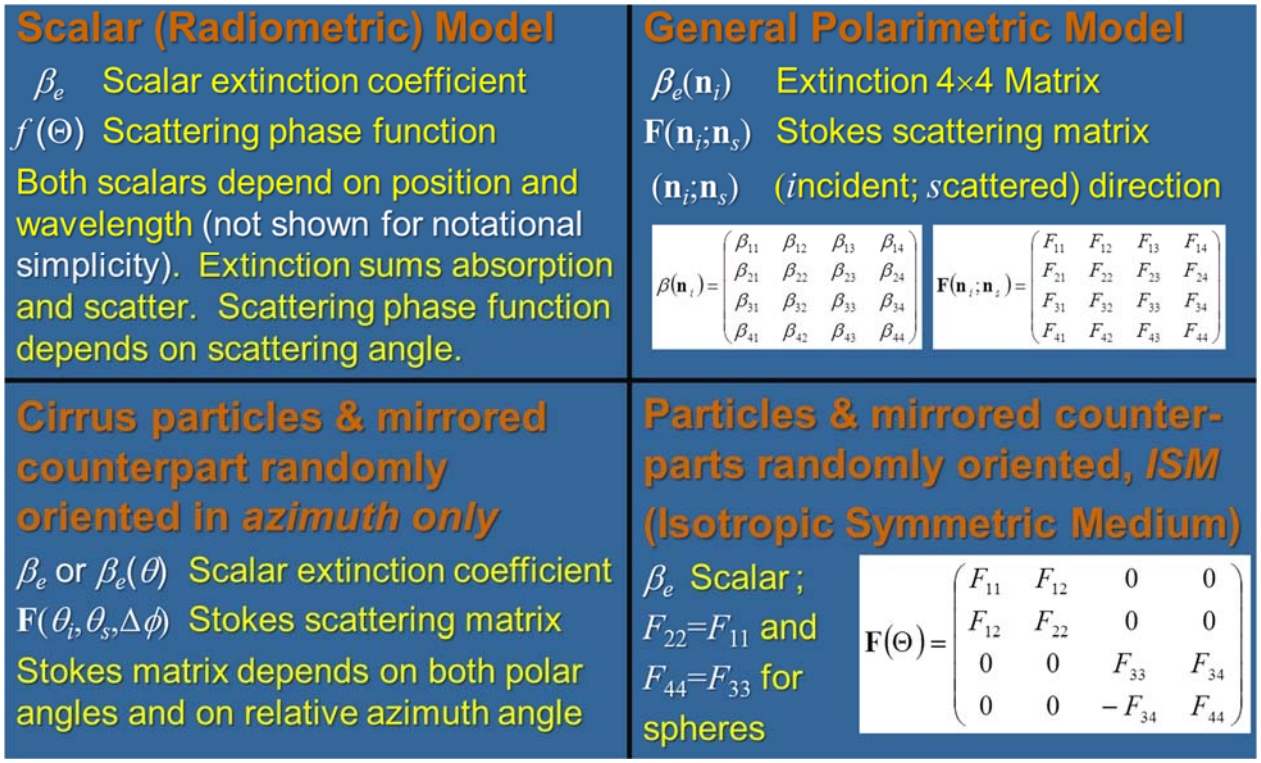

Figure 9. Particulate Data Forms under Varying Scattering Model Assumptions.

2.1.2.1 Polarimetric Stokes Scattering Matrices and Cross-Sections

As described in the *Review of Polarization* sub-section of the Section 2 introduction, polarimetric state can be defined by a Stokes intensity column 4-vector, $[I, Q, U, V]^T$. In general, the scalar scattering phase function used in radiometric calculations must be replaced by a 4 × 4 Stokes scattering matrix for polarimetric calculations, as in the upper right in Figure 9. Each Stokes incident component is partitioned into its 4-vector scattered components via the matrix $\mathbf{F}(\mathbf{n}_i; \mathbf{n}_s)$.

$$\begin{pmatrix} I \\ Q \\ U \\ V \end{pmatrix}_s = \mathbf{F}(\mathbf{n}_i;\mathbf{n}_s) \begin{pmatrix} I \\ Q \\ U \\ V \end{pmatrix}_i \quad ; \quad \mathbf{F}(\mathbf{n}_i;\mathbf{n}_s) = \begin{pmatrix} F_{11} & F_{12} & F_{13} & F_{14} \\ F_{21} & F_{22} & F_{23} & F_{24} \\ F_{31} & F_{32} & F_{33} & F_{34} \\ F_{41} & F_{42} & F_{43} & F_{44} \end{pmatrix} \quad . \tag{13}$$

The 16 matrix elements depend on the incident $\mathbf{n}_i$ and scattered $\mathbf{n}_s$ directions and on particle orientation (not labeled). The extinction and scattering cross-sections also depend on incident and particle orientation directions (most generally, the cross-sections are also 4 × 4 matrices as shown in Figure 9; this generality will not be modeled as its importance to IR through visible atmospheric and surface modeling of polarimetric signatures is negligible).

2.1.2.2 Isotropic and Symmetric Medium

In the Phase I proposal, the polarimetric signature modeling problem was simplified by indicating that only media containing randomly oriented particles and their mirror images (Isotropic and Symmetric Medium or ISM) would be considered. Under this approximation, the Stokes scattering matrix is 2 × 2 block diagonalized with only 6 non-zero elements, as in the lower right in Figure 9. Furthermore, these elements only depend on the scattering angle Θ:

$$F(\Theta) = \begin{pmatrix} F_{11}(\Theta) & F_{12}(\Theta) & 0 & 0 \\ F_{12}(\Theta) & F_{22}(\Theta) & 0 & 0 \\ 0 & 0 & F_{33}(\Theta) & F_{34}(\Theta) \\ 0 & 0 & -F_{34}(\Theta) & F_{44}(\Theta) \end{pmatrix} . \quad \textbf{(14)}$$

Spheres are a special case for which the diagonal matrix elements in each of the two 2 × 2 blocks are equal, *i.e.*, $F_{22}(\Theta) = F_{11}(\Theta)$ and $F_{44}(\Theta) = F_{33}(\Theta)$. The ISM extinction and scattering cross-sections are scalars and independent of direction as indicated in Figure 9.

2.1.2.3 Particles and Their Mirrored Counterparts Randomly Oriented Azimuthally

The primary focus of the DOE effort is to enable modeling of the polarimetric signature of ground reflected targets and backgrounds. With this in mind, it is sufficient to model the atmosphere as an ISM medium. That being said, it would be unfortunate to not at least consider, as part of the Phase II effort, providing the flexibility to import Stokes scattering matrices that arise from modeling ice crystals that tend to align their major axis horizontally. This horizontal alignment in cirrus cloud leads, for example, to the linear polarization of their thermal emission, whereby the vertical (parallel), $I_v \equiv (I + Q)/2$, and horizontal (perpendicular), $I_h \equiv (I - Q)/2$, Stokes parameters differ. Measurement of this linear polarization can be used to distinguish water droplet, super-cooled water, and ice clouds. This is important because flying into super-cooled clouds with hovering aircraft (helicopters) can cause catastrophic icing.

This relaxing of the ISM requirement does impact the form of the Stokes scattering matrices and cross-sections that MODTRAN7 and P-MCScene could ingest. MODTRAN's 1D, spherical shell geometry would require that particles and their mirrored counterparts be randomly oriented azimuthally, but not with respect to polar angle. Under these conditions (lower left in Figure 9), the Stokes scattering matrix is no longer 2 × 2 block diagonal, and the generalized matrix elements are functions of the incident and scattered polar (off-nadir) angles, θ_i and θ_s, and the relative azimuth, $\Delta\phi \equiv \phi_i - \phi_s$, between the incident and scattered directions (recall that the IMS Stokes scattering matrix elements are only functions of the scattering angle, $\Theta = \arccos[\cos\theta_i \cos\theta_s + \sin\theta_i \sin\theta_s \cos(\phi_i - \phi_s)]$). Furthermore, the extinction and scattering cross-sections depend on the incident or scattered polar angle. K.N. Liou notes that "for all practical purposes, we may use the scalar β_e for applications to ice crystals cases," [Liou, 2002], which significantly simplifies the particulate description. It should be noted, however, that there is some controversy regarding this issue [Mishchenko, 1994; Takano and Liou, 1994].

2.1.2.4 Available Particulate Databases

Major efforts within the radiative transfer community have produced high quality databases of dust-like aerosol and cirrus cloud polarimetric data. Both sets of data cover essentially the entire MODTRAN/MCScene spectral range, from the ultraviolet (0.2 μm) into the far-infrared (~100 μm). Both of these databases have been generated for randomly oriented particles and their mirrored counterpart, ISM conditions.

The mineral dust aerosol database [Meng *et al.*, 2010] models spheres, randomly oriented prolate spheroids (two minor axes equal), oblate spheroids (two major axes equal) and tri-axial ellipsoids (see Figure 10) with aspect-ratios, $\varepsilon_{a/c} \equiv a/c$ and $\varepsilon_{b/c} \equiv b/c$, ranging from 0.3 to 1.0; here the semi-axis lengths

are denoted by $a \le b \le c$. All particles are assumed homogeneous. The optical parameters are tabulated as functions of 5 parameters: the two aspect ratios, $\varepsilon_{a/c}$ and $\varepsilon_{b/c}$, the size parameter, $x \equiv 2\pi c / \lambda$ where λ is the wavelength, and the complex index of refraction, $\tilde{n} = n + i\,\kappa$. Based on dust particle refractive index measurements, data was generated for $1.10 \le n \le 2.10$ with $0.0005 \le \kappa \le 0.5$ for $n < 1.70$ and with $0.1 \le \kappa \le 0.5$ for $n \ge 1.70$. The database includes a software package to compute the bulk optical properties for specific aerosol size distributions. SSI has downloaded and previously exercised this database.

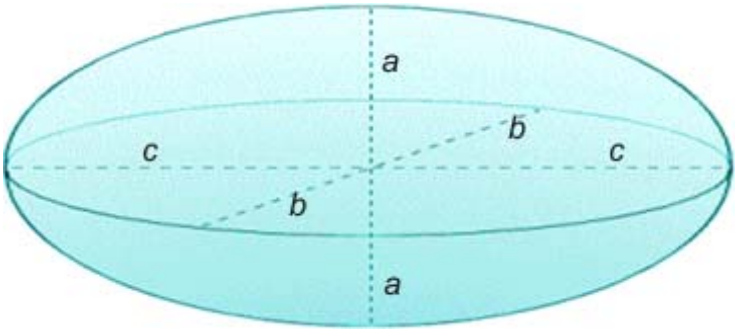

Figure 10. Image of a Tri-Axial Ellipsoid, the Particle Shape Used in the Mineral Dust Aerosol Database [Meng *et al.*, 2010].

The state-of-the-art ISM cirrus data library for the radiative transfer and remote sensing community is extremely impressive. The most recent description was published in 2013 [Yang *et al.*, 2013]. As illustrated in Figure 11 (left), ice crystal data have been generated for 11 different habits (shapes and arrangements), each modeled with smooth, moderately roughened, and severely roughened surfaces. Bulk properties are defined for habit dependent size distributions with maximum sizes varying between 2 μm and 1 cm. For each habit and surface roughness, scattering properties are generated for 445 wavelengths between 0.2 and 100.0 μm and for 189 particle sizes. The 6 Stokes scattering matrix elements are generated at 498 scattering angles. Clouds are defined by habit mixtures; four groupings from MODIS Collection 5 are illustrated on the right in Figure 11 [Baum *et al.*, 2005]. A request to download the data will be completed when logistics have been worked out.

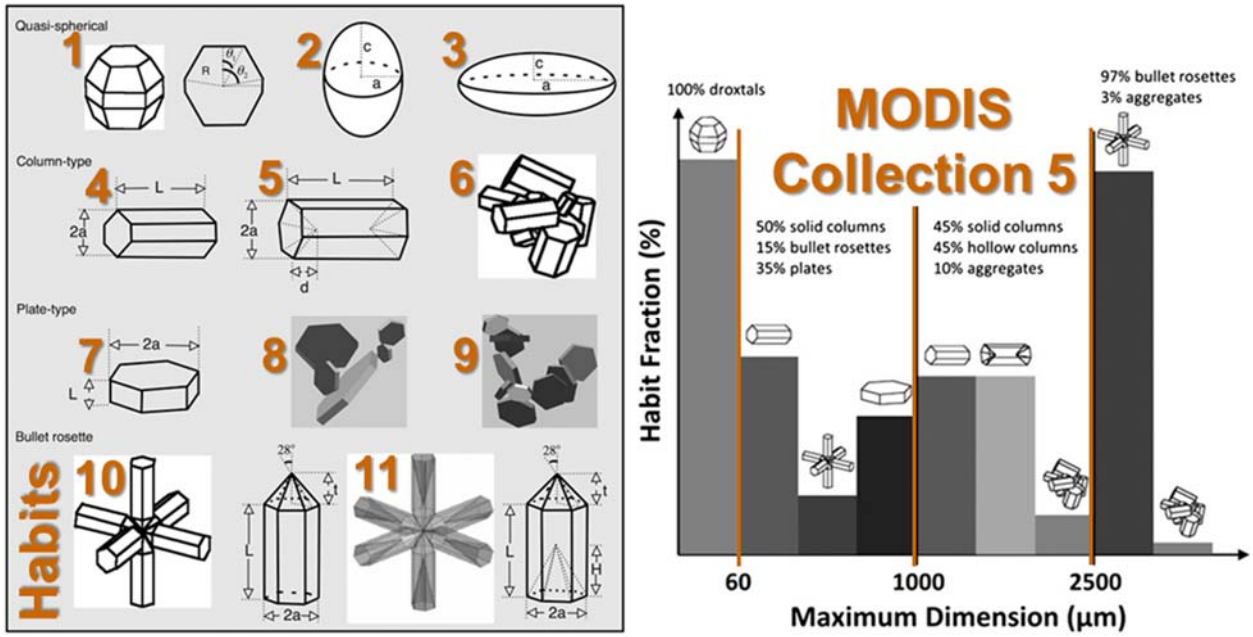

Figure 11. At left, Habits Included in the Atmospheric Ice Crystal Data Library [Yang *et al.*, 2013]. At right, Habit mixture used in the MODIS Collection 5 ice model [Baum *et al.*, 2005].

Both the mineral dust aerosol database and the atmospheric ice crystal data library provide tools to generate the Stokes scattering matrix elements at a very fine angular resolution. This is precisely the scattering distribution data that will be required by the P-MCScene Monte-Carlo based radiative transfer to model atmospheric scatter, and required by MODTRAN7 to model single solar scatter. However, the vector discrete ordinate model that will be integrated into MODTRAN7 to calculate multiple scatter (more precisely, multiple scatter solar and all thermal scatter), VDISORT3, requires that the Stokes scattering matrix elements be expanded in generalized spherical functions [Mishchenko *et al.*, 2002; 2006]. MODTRAN7 will either obtain or develop a module for generating the generalized spherical function coefficients from the tabulated matrix elements.

2.1.2.5 MODTRAN4P Polarimetric Aerosol Data

A polarimetric version of MODTRAN4, dubbed MODTRAN4P, was developed for the US Air Force [Robertson *et al.*, 2007]. The primary focus of this effort was computation of atmospheric polarization; no modeling of polarimetric surface reflections was included. However, databases of Stokes scattering matrices and their generalized spherical function expansion coefficients were generated for several of the MODTRAN model aerosols. These will be integrated into MODTRAN7. A description of the MODTRAN4P database generation task, adapted from the final report, follows.

2.1.2.5.1 Data Description and Validation

The optical data for aerosol and cloud models in the scalar MODTRAN were calculated using Mie theory assuming spherical particles. Solutions were obtained that depend on wavelength λ, particle radius, and complex indices of refraction. Integration over size distributions was performed to generate scattering phase functions for a grid of wavelengths and scattering angles for each particulate model. The same approach was used in the development of MODTRAN4P for the polarized calculations.

Stokes scattering matrices were calculated for the MODTRAN Rural, Urban, Maritime, Tropospheric, Stratospheric and Meteorite models. These models cover altitudes from the surface to the top of the atmosphere (100 km for MODTRAN). To maintain backward compatibility, the same properties (size distributions and indices of refraction) as those in the earlier calculations [Shettle and Fenn, 1979] were used. The MODTRAN user maintains options to vary both the surface meteorological range (visibility measured at 0.55 μm) and relative humidity. The aerosol Stokes scattering matrices and absorption/scattering coefficients were calculated for 698 wavelength points from 0.2 to 299.9 μm. The new calculations provide finer resolution than the original calculations in both their angular and wavelength grids. The total intensities were compared to the earlier results, and agreement within the accuracy of the calculations was obtained. Figure 12 compares the phase functions at 1.06 μm.

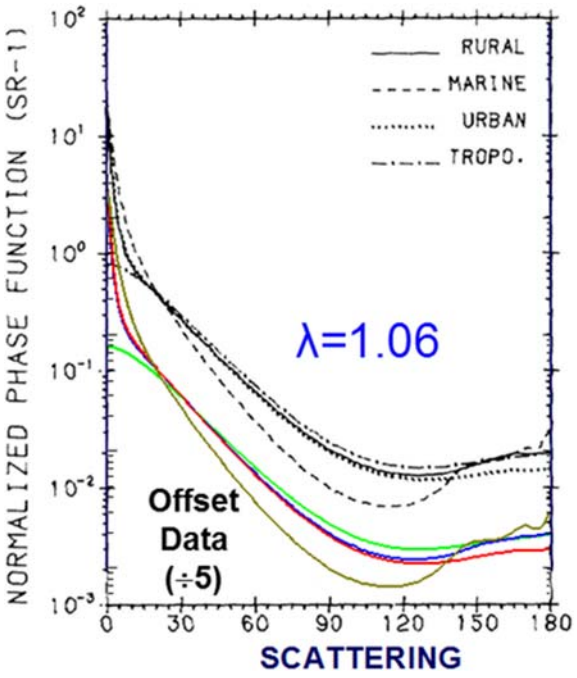

Figure 12. Comparison of Aerosol Phase Functions Calculated with the NASA T-matrix Code [Mishchenko *et al.*, 1998] to the Earlier Ones [Shettle and Fenn, 1979]. The new calculations (solid colored curves) have been offset by a factor of 5 for clarity

2.1.2.5.2 Generalized Spherical Function Expansion Coefficients

MODTRAN4P used an early version of the vectorized discrete ordinate model, VDISORT, to model atmosphere scatter. VDISORT requires an expansion of the Stokes scattering matrix element in generalized spherical functions. For spherical particles, the expansion terms are given by

$$F_{11}(\Theta) = \sum_{l=0}^{2N-1} \alpha_1^l P_{0,0}^l(z) = F_{22}(\Theta) \quad ; \tag{15a}$$

$$F_{44}(\Theta) = \sum_{l=0}^{2N-1} \alpha_4^l P_{0,0}^l(z) = F_{33}(\Theta) \quad ; \tag{15b}$$

$$F_{12}(\Theta) = \sum_{l=2}^{2N-1} \beta_1^l P_{0,2}^l(z) = F_{21}(\Theta) \quad ; \tag{15c}$$

$$F_{34}(\Theta) = \sum_{l=2}^{2N-1} \beta_2^l P_{0,2}^l(z) = -F_{43}(\Theta) \quad , \tag{15d}$$

where Θ is the scattering angle and $z = \cos\Theta$. These generalized spherical functions provide a compact description of the angular or geometric part of the discrete ordinate expansion so that the expansion coefficents (the α^l and β^l) represent the dynamics of the scattering process.

For $m = n = 0$, the generalized spherical functions equal the Legendre polynomials,

$$P_{00}^l(z) = P_l(z) \tag{16}$$

The functions P_{02}^l are related to the associated Legendre functions and Legendre polynomials, by

$$P_{02}^l(z) = -\sqrt{\frac{(l-2)!}{(l+2)!}}\, P_l^2(z) = -\sqrt{\frac{(l-2)!}{(l+2)!}}\,(1-z^2)\,\frac{\mathrm{d}^2}{\mathrm{d}z^2} P_l(z) \quad . \tag{17}$$

2.1.2.5.3 NASA T-Matrix Code Calculations

The T-Matrix code for Lorenz-Mie scattering calculations of polydisperse spherical particles, `spher.f` , was obtained from the NASA Goddard Institute for Space Studies website [Mishchenko *et al.,* 1998; Mishchenko, 2005; www.giss.nasa.gov/staff/mmishchenko/t_matrix.html]. This code generates the expansion coefficients and provides tools to calculate the scattering matrix elements at any scattering angle from the coefficient set. This T-Matrix code performs a series of Mie calculations at one wavelength over a particle size distribution consisting of one particle type.

The MODTRAN boundary layer aerosol models have significant mass density in particles far larger than the mode radii of the distributions. The boundary layer aerosol models also have multiple component materials, and the particle sizes are modeled as bimodal lognormal distributions, with the smaller and larger mode radii dependent on the relative humidity [Shettle and Fenn, 1979; Fenn *et al.*, 1985]. The mode radius for the larger size distribution in each model can be on the order of 1 μm at higher humidities. The smaller aerosols with mean radii of about 0.03 to 0.05 μm are equivalent to the background tropospheric model. The larger ones, with mean radii ranging approximately from 0.1 to 1.0 μm, are illustrative of the boundary layer type (rural, urban, maritime, …). Each aerosol model results from combining several independent Mie calculations. The higher altitude models (stratospheric and meteoric dust) use a single size distribution.

Calculation of the optical properties involves an integration over the size distribution, up to some maximum radius r_{max} which must be chosen large enough to contain most of the volume that would be in the ideal, un-truncated lognormal distribution; for the large particle modes at high humidities, this integration cutoff can be quite large. Since the calculation time grows roughly as the cube of the maximum size parameter $x_{max} = 2 \pi r_{max} / \lambda$, the time to calculate optical properties for the shorter wavelengths in the standard MODTRAN set was quite long. The calculations used r_{max} in the range of 100 to 125 times the mode radius, int(10*r_{max}) subdivisions, and 100 Gauss points per subdivision. The database for MODTRAN4P contains 129 moments (l = 0 to 128).

2.1.2.5.4 Dependence on Relative Humidity

The scattering phase functions for the boundary layer and tropospheric aerosol models in scalar MODTRAN are tabulated at four relative humidity (RH) values: 0, 70, 80, and 99%. However, the original particle optical properties were generated for 8 RH values: 0, 50, 70, 80, 90, 95, 98, and 99% [Shettle and Fenn, 1979]. For MODTRAN4P, data was generated for the full set of 8 values. The RH dependence of the mode radii for the larger particle distributions is shown in Figure 13.

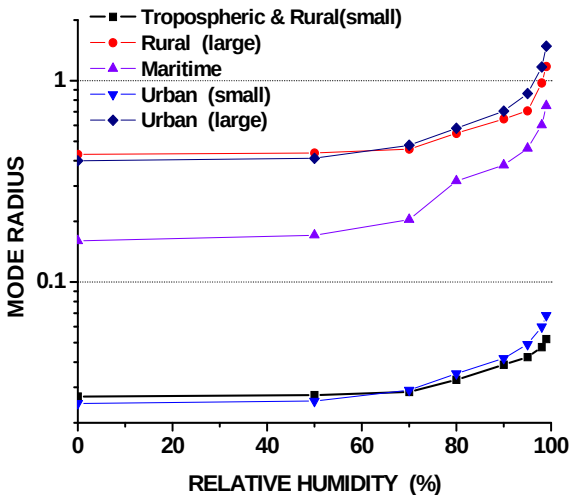

Figure 13. Growth of the Mode Radii for the Larger Particles from Different Boundary Layer Aerosol Models.

2.1.2.5.5 MODTRAN Ingestion of the Aerosol Data File

The six aerosol models (rural, urban, maritime, tropospheric, stratospheric and mesospheric) have been calculated for the full set of wavelengths. They are tabulated in two separate databases, one (`Muel.dat`) containing the angular grid of Stokes scattering matrix elements, and the other (`Tmat.dat`) containing the Stokes scattering matrix generalized spherical function expansion coefficients. In order to reduce computation time, the first four of the aerosol models listed above were calculated on a sparser wavelength grid in the visible and near UV spectral regions (spaced every 0.05 μm from 0.2 to 0.7 μm).

The data files containing angular grids of Stokes scattering matrix elements are used by MODTRAN4P to calculate the single scattering. The expansion coefficients data files, on the other hand, are required for the VDISORT scattering model. MODTRAN4P reads both files and performs consistency checks. There is a list of a number of inequalities that the elements of the ISM Stokes scattering matrices must satisfy [Mishchenko *et al.,* 2002, Eqs. 4.55-4.60]:

$$|F_{22}| \le F_{11}, \quad |F_{33}| \le F_{11}, \quad |F_{44}| \le F_{11}, \quad |F_{12}| \le F_{11}, \quad |F_{34}| \le F_{11} \quad ; \qquad \textbf{(18a)}$$

$$(F_{33} + F_{44})^2 + 4(F_{12}^2 + F_{34}^2) \le (F_{11} + F_{22})^2 \quad ; \quad \textit{and} \qquad \textbf{(18b)}$$

$$|F_{33} - F_{44}| \le F_{11} - F_{22}, \quad |F_{22} \mp F_{12}| \le F_{11} \mp F_{12} \qquad \textbf{(18c)}$$

Each of these conditions is confirmed as the database is being read.

2.1.2.6 MODTRAN6 Aerosol and Cloud Generation Toolkit

The introduction to Section 2 included a short description of the MODTRAN6 aerosol toolkit (ATK) and a flowchart, Figure 5, of the processing. The ATK will be used to generate data for the MODTRAN built-in aerosol and cloud models for which polarimetric data has yet to be generated. These include the desert and navy aerosol models, the cumulus, stratocumulus, altostratus, nimbostratus, and stratus water cloud models, and the standard and sub-visual cirrus models. The toolkit will also enable users to define custom aerosols for use in MODTRAN7, and subsequently, in P-MCScene.

The offline ATK has been developed to calculate optical properties from physical descriptions of aerosols with specified number density vertical profiles. The ATK is a function library which calculates radiometric (scalar) or polarimetric (vector) optical properties; it also writes Spectral Aerosol Profile (SAP) scalar input data files for use by MODTRAN. The format of the SAP files is described in the MODTRAN User's Manual. Since SAP files currently only contain scalar optical data, user codes must be written to link against the library and access the results of polarimetric calculations through the FORTRAN and C/C++ Application Programming Interfaces (APIs). Updated polarimetric SAP files will also be defined to enable their generation using the ATK text interface.

The Toolkit treats an aerosol as a superposition of "components", each component defined as a collection of particles with a specified size distribution, a shape, a set of spectral real and imaginary refractive indices, and a number density vertical profile. The particle size distributions can have one of several functional forms: lognormal, power-law, Modified power-law, Gamma, or Modified Gamma. Calculations are performed with NASA T-Matrix codes either for spherical (Mie) particles or for more general axisymmetric particle shapes. Both the Mie and T-Matrix codes are described in Chapter 5 of the Mishchenko, Travis and Lacis text [Mishchenko *et al.*, 2002].

A sample text interface input file, *ex2_tropo_0rh_tmat_expdec.in*, is presented in Table 2. Although there are only about a dozen inputs, the file itself is quite long because it contains extensive commenting. The reader is encouraged to peruse the input to verify its simplicity.

2.1.3 Polarimetric Field Measurement

Three US Government funded polarimetric field measurement programs were investigated to determine the availability of the measurement data and the utility of that data for validation of MODTRAN7 and P-MCScene. Two of the field measurement programs deployed thermal infrared (TIR) sensors, with one focused on understanding pBRDF effects and the other on studying target environmental variability. The third field measurement recorded solar regime (VNIR) spectral polarimetric signatures. Each of these programs is described in greater detail in the sub-sections that follow.

2.1.3.1 Air Force Research Laboratory (AFRL) Infrared Polarization Study

Dr. Tom Caudill, at the AFRL Space Vehicle Directorate in Kirtland Air Force Base (AFB), was contacted to discuss a thermal infrared polarimetric BRDF measurement program he directed. As described in a SPIE paper [Fetrow *et al.*, 2002], spectral longwave infrared (LWIR) material polarimetric measurements were recorded at various angles and temperatures in the laboratory at Kirtland AFB. Surface roughened pBRDFs were retrieved. Next, the material plates were placed in the field at Eglin AFB and measured under ambient conditions. This program funded development of MODTRAN4P, which was used to simulate the downwelling radiances impingent on the surface. Polarimetric reflected radiances were synthetically generated by coupling the downwelling radiances with the laboratory-derived parameterized pBRDFs. These were compared to the field measurements. The comparisons of synthetic and measurement spectral data showed mixed results, suggesting the need for improved characterization of the materials and the atmosphere.

Table 2. MODTRAN6 Aerosol Toolkit Tropospheric Aerosol T-Matrix Calculation Input File. Comment lines are all italicized and begin with the hash (#) symbol.

```
# Example text input file #2.
#
# Tropospheric aerosol at 0% relative humidity; number densities decrease exponentially with
# altitude. The two components have their own scale heights:
#     800m for component 1 (water-soluble)
#    1200m for component 2 (dust-like)
#
# Oblate spheroidal particles all with aspect ratio 1.1, calculations done by T-matrix code.
#
# NOTES ON FORMATTING AND UNITS:
# ==============================
# Comments begin with a hash-mark (like these lines), and can be either full-line or line-ending.
# They are ignored when the file is processed.
#
# Each line is treated as a sequence of keywords and values; most keywords must be followed
# immediately by the value to be set.
#
# White space is used as the "token separator" in a line, so there should be at least one space
# between successive keywords, numbers, filenames, etc. in a line, but the exact number of spaces
# between successive tokens is not important.
#
# Keywords are not case-sensitive, but directory paths and filenames are.
#
# Colons, commas, and equal-signs are useful for readability, and are converted to spaces when
# the file is processed. For example, a size distribution in the specification of an aerosol
# component may be punctuated as:
#
# BeginComponent 1
#   size_distribution: lognormal, rg=0.02700, logsg=0.80590487, rmin=0.00107489, rmax=0.6782096
#   # lines for the shape, refractive index, etc. here
#   # ...
# EndComponent 1
#
# Blank lines are discarded when processing, but used judiciously they make the file easier for
# humans to read.
#
# INPUT UNITS:
#   Units for particle sizes, integration ranges, and wavelengths are microns.
#   Units for altitudes are meters (above sea level).
#   Units for number densities are particles/cm^3.
#   Units for angles are degrees.
#
BeginInput
#
# Path to the directory where data files reside.
# The keyword  DataDir  requires the directory path immediately following it.
#
# When a filename is specified, e.g., for material refractive index, the program will check both
# the data directory and the current working directory. Specify this first, to be safe.
#
DataDir:  ../data/
#
# Calculation method:  Can be either  Mie  or  Tmatrix .
#
# If  Mie  is selected, the particle shapes for all aerosol components must be spheres – if
# they're not, they will be changed to that.
#
# If  Tmatrix  is selected, and some particle shapes are spheres, they will be changed to oblate
# spheroids with a very small eccentricity.
#
# NOTE  For Tmatrix calculations, it is necessary to specify the maximum and minimum numbers of
#         Gauss points to be used for size integrations.  These are set using the "general"
#         keywords  NGaussMax  and  NGaussMin .  Since there is no heuristic formula for
#         determining the required maximum number of Gauss points in order to get converged
#         solutions, one must generally run an aerosol calculation with different values
#         NGaussMax  and check the convergence of the resulting absorption and extinction
#         coefficients, expansion coefficients, and scattering matrix elements.
```

Table 2 (*cont'd*). MODTRAN6 Aerosol Toolkit Tropospheric Aerosol T-Matrix Calculation Input File.

```
#       The  NGaussMax  and  NGaussMin keywords are ignored when performing Mie calculations.
#         An example is given in the second example input file,  textinput2.in .
#
CalculationMethod:  Tmatrix
#
# Specification of the components in the aerosol model.
#
# An aerosol model consists of several "components".
#
# Each component is a collection of particles with a specified shape (habit), and a size
#   distribution (in one of the supported functional forms), all consisting of the same
#   material, for which spectral refractive index data must be supplied.
#
# Each component will also have an altitude-dependent number density associated with it; that can
#   be given in the component specification, or later, after all components have been described.
#
# The number of aerosol components:  at least 1 but not over 9000.  This must be defined before
# the descriptions of individual components.
#
NComponents:  2
# Descriptions of the individual aerosol components.
#
# These descriptions must come after the specification of  NComponents . There must be
# NComponents  descriptions.
#
# Each component is characterized by a size distribution, a shape (habit), and a set of spectral
#   refractive index data. Each of these must have all its parameters on one line, beginning with
#   the appropriate keyword, as shown below. The set of parameters may be entered in any order
#   within a description.
#
# Most size distribution specifications include the parameters  rmin  and  rmax , which are
#   generally the limits of integration over particle sizes, expressed as "equivalent sphere"
#   radii in microns (Exceptions are described below).
#
# For aerosol components with non-spherical shapes (habits), an "equivalent" sphere may be either
#   one with volume equal to that of a particle in the distribution, or one with equal surface
#   area. The choice of what to use as an equivalent sphere is made in the shape specification;
#   see below.
#
# Size distributions can be:
#
#   "ModifiedGamma" with parameters  alpha, rc, gamma,  rmin, rmax :
#
#                         alpha                   gamma          alpha
#     n(r) = constant * r      * exp( -alpha * r     /(gamma*rc      ) )
#
#
#   "Lognormal" with parameters  rg, logsg,  rmin, rmax :
#
#                            /              2 \
#                            | - log(r / rg)  |
#     n(r) = constant * exp| ------------- | / r
#                            |            2    |
#                            \    2 logsg     /
#
#     Here,   rg     is the mode radius (microns);
#             logsg  is the logarithmic standard deviation.
```

Table 2 (*cont'd*). MODTRAN6 Aerosol Toolkit Tropospheric Aerosol T-Matrix Calculation Input File.

```
#   "PowerLaw" with parameters  reff, veff  (calculates rmin and rmax)
#
#           /              -3
#     n(r) = |  constant * r   ,  rmin <= r <= rmax,
#           \  0              ,  otherwise
#
#     Effective radius  reff , and effective variance  veff , are defined as:
#
#            1     rmax                     2
#     reff = --- Int     dr  n(r) * r * (pi*r ) ,
#           <G>    rmin
#
#               1        rmin                       2        2
#     veff = --------- Int     dr  n(r) * (r - reff)  * (pi*r ) ,
#                   2    rmax
#           <G> reff
#
#       where
#                rmax                 2
#       <G>  = Int     dr  n(r) * (pi*r ) .
#                rmin
#
#
#   "Gamma" with parameters  a, b,  rmin, rmax :
#
#                        (1 - 3*b)/b      / -r  \
#     n(r) = constant * r             * exp| --- |   ,  0 < b < 0.5
#                                          \ a*b /
#
#
#   "ModifiedPowerLaw" with parameters  alpha,  rc, rmax :
#
#           /  constant               ,  0 <= r <= rc
#     n(r) = |                    alpha
#           |  constant * (r/rc)       ,  rc <= r <= rmax
#           \  0                      ,  rmax <  r
#
#     The minimum limit of integration is  r == 0, and the maximum limit is  rmax ;  rc  is the
#       inflection point in the number density.
#
# Particle shapes can be:
#
#   Sphere (doesn't need any descriptive parameters)
#
#   Cylinder    with  eps = diameter/length and either  equal-surface-area  or  equal-volume .
#
#   Spheroid    with  eps = (horizontal_axis)/(rotational_axis) and either  equal-surface-area
#                 or  equal-volume .
#
#   Chebyshev   (followed by an integer degree  n  from 1 through 10), with  eps  related
#                 to the shape by  r(theta) = r0*[1 + eps*T_n(cos(theta))] and either
#                 equal-surface-area  or  equal-volume .
#
# For the non-spherical particle shapes, the  equal-<measure>  keywords specify whether an
#   "equivalent" sphere is one with equal surface area or equal volume as the nonspherical
#   particle.  The default selection is  equal-volume .
#
# Each component also has a number density profile depending on altitude; see later.
#
BeginComponent 1
  shape:  spheroid  equal-surface-area  eps = 1.1
  size_distribution:  lognormal  rg: 0.02700  logsg: 0.80590487 rmin: 0.00107489  rmax: 0.6782096
  refractive_index:  -f  m_wtrsol
EndComponent 1
#
```

Table 2 (*cont'd*). MODTRAN6 Aerosol Toolkit Tropospheric Aerosol T-Matrix Calculation Input File.

```
BeginComponent 2
  shape:  spheroid  equal-surface-area  eps = 1.1
  size_distribution:  lognormal  rg: 0.02700  logsg: 0.80590487 rmin: 0.00107489  rmax: 0.6782096
  refractive_index:  -f  m_dustlike
EndComponent 2
# Number density profiles: Files or inline lists of particle densities (particles/cm^3) at
#   altitudes (meters above sea level), one for each aerosol component.
#
#   These may each be within or immediately after each component description, or all grouped
#     after all the component descriptions. However, there must only be one for each component.
#     If the number density profile is specified *within* a component description, do not follow
#     the keyword with the component number.  However, if it is specified *outside* a component
#     description, the component number is required.
#
#   If the profile is from a file, describe the profile with "-f" and the filename.
#
#   If the profile is an inline table, describe it with "-num" followed by the number of
#     altitudes on the same line, and then one line for each altitude, with the altitude (meters)
#     in the first field, and the number density (particles/cm^3) in the second field.
#
NDensityProfile 1  -f  sap_zprof_tropo1exp
NDensityProfile 2  -f  sap_zprof_tropo2exp
#
# Details of the calculation:
#
#   A  Dimension  entry is required, either  1 (scalar or radiometric) or
#      4 (vector or polarimetric).
#
#     1 (Scalar)        Only the intensity phase function and it Legendre moments are calculated.
#     4 (Polarimetric)  Polarimetric components are calculated for both the scattering matrix
#                         elements and their Generalized Spherical Function (GSF) expansions,
#                         assuming an isotropic, symmetric medium (ISM).
#
#   NOTE  The polarimetric option is currently inactive for text input, since a text file format
#           for output of polarimetric data has not been defined.
#
#   Maximum and Minimum numbers of Gauss points for size integrations; only needed for T-Matrix
#   calculations.
#
#   List of wavelengths (spectral range), from file or inline list.
#
#   List of scattering angles, from file or inline list.
#
#   List of altitudes, from file or inline list.
#
#   Overall maximum order of Legendre/Generalized Spherical Function (GSF) moments to save.
#
Dimension:  1
NGaussMax: 200
NGaussMin:   5
Wavelengths:  -f  sap_wlens
ScatAngles:  -f  scatangles
Altitudes:  -f  sap_alts
MaxMomentSaved:  64
# The  EndInput  line indicates the end of the aerosol description. Upon reading this string, the
# program
#
#       ignores the rest of the file (which may have comments, etc.),
#
#       verifies that inputs have fully specified an aerosol calculation (terminating if it has
#         not), and
#
#       begins calculating the optical properties.
#
EndInput
```

Dr. Caudill has requested that the spectral LWIR polarimetric measurement data from the AFRL program be made available for the proposed DOE SBIR Phase II effort. It is hoped that the retrieved spectral pBRDF data may be useful in evaluating the accuracy of spectral interpolation procedures for the NEF Data System pBRDF data. In addition, the field measurement data can be used to evaluate the MODTRAN7 and P-MCScene simulation capabilities. These simulations will differ from the original AFRL simulations in that the surface materials and the atmosphere will be coupled together into coherent radiative transfer models.

2.1.3.2 The Spectral and Polarimetric Imagery Collection Experiment (SPICE)

Dr. Joao M. Romano, at the US Army Armament Research, Development and Engineering Center ARDEC, was contacted to discuss the Spectral and Polarimetric Imagery Collection Experiment (SPICE) [Romano *et al.*, 2010; Rosario *et al.*, 2014]. The SPICE program was a collaborative effort between ARDEC and the Army Research Laboratory designed to measure target variability due to weather, diurnal, and seasonal changes. LWIR and mid-wave infrared (MWIR) hyperspectral and broadband polarimetric and radiometric imagers were placed on the Precision Armament Laboratory (PAL) tower at Picatinny Arsenal. The instruments were deployed to measure surrogate 2S3 Self-Propelled Howitzer targets embedded in the northern New Jersey terrain continuously (24/7) over a 1 to 2 year period. As illustrated in Figure 14, targets were oriented nose-on (0°), broad-side (90°) and skewed (135°). Data was recorded at detection distances of 0.55 and 1.2 km. The scene included a blackbody to baseline surface temperature, a reflective aluminum panel for characterization of downwelling flux, partially hidden concrete and metal huts, a variety of vegetation, and a dirt road.

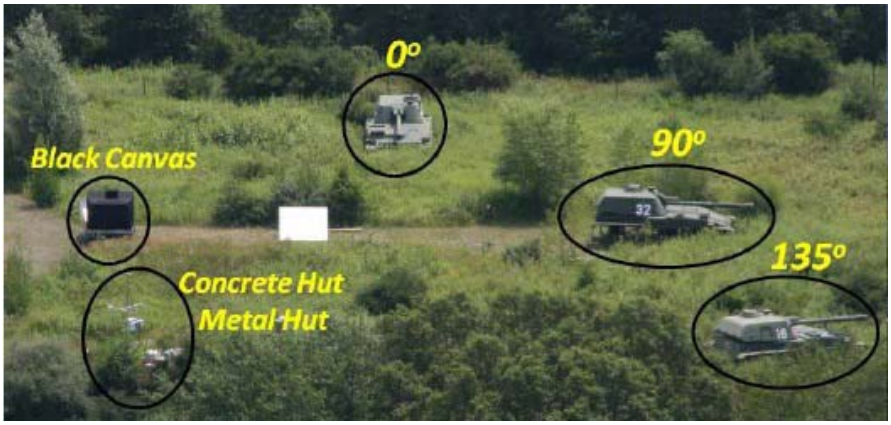

Figure 14. Visual Image of the Mid-range Target Site.

The data is restricted (Distribution B – US Government only); SSI has requested a relaxation of distribution designation to include US Government contractors (Distribution C) for Phase III validations of MODTRAN7 and P-MCScene. The objective of this validation task would be to test the ability of the simulation software to capture the weather, diurnal, and seasonal variability of the bandpass polarimetric signatures. Even if the data distribution designation cannot be changed, SSI will provide the Phase II product software to the US Army to support efforts to use the software broaden the measurement space (providing alternative detection ranges and target views). The original SPICE program was completed in 2014, but a follow-on effort is being planned with a modified instrument suite. If available, data from the follow-on effort will also be incorporated into the Phase III validation efforts.

2.1.3.3 Sandia National Laboratory VNIR Spectral Polarimetry Measurement Program

Dr. Julia Craven, a member of the Remote Sensing and Exploitation (RSE) group at Sandia National Laboratories (SNL), was contacted to discuss a DOE funded measurement program, led by her, designed to evaluate the utility of exploiting signatures arising from material polarimetric BRDFs to reduce target detection false positives. Her team is measuring the spectral linear polarization in materials of interest

using a Headwall Photonics push-broom HSI sensor retrofitted with polarimetric fore-optics. The sensor is mounted on a scissor lift, and target materials are laid flat and viewed from 45° off-nadir between 10 and 25 m above ground level (AGL). The spectral Stokes parameters. I_λ, Q_λ, and U_λ are extracted.

The polarimetric measurements are made as part of a much larger measurement program which constrains viewing geometry flexibility; for instance, there is no opportunity to acquire a greater range of angular data by tilting targets. Angular variability is measured as the sun traverses the sky throughout the day. The scissor lift can also be repositioned to vary target orientation. One goal is to characterize the pBRDF as a function of surface morphology. Controlled laboratory measurements are also performed to better parameterize the material pBRDF's.

SNL is interested in using the MODTRAN7 and P-MCScene simulation capabilities to expand their data beyond the field measurement sampling space. In particular, there is an interest in utilizing the proposed models to generate synthetic data at much larger slant ranges. For materials that are in the NEF Data System and also SNL targets, SSI plans to directly validate the MODTRAN7 and P-MCScene simulations of spectral Stokes parameters against the values derived from the SNL measurements. In addition, the measurements will be used to test VNIR spectral interpolation of NEF Data System pBRDF's. Finally, SNL has suggested that additional polarimetric measurements of the target materials could be made at their facility on Kirtland AFB. These measurements could be made with the targets situated on a 2-gimbal system, to enable greater characterization of angular dependencies.

2.2 Formulate the MODTRAN7 Polarization Approach

MODTRAN6 solves the integral form of the *scalar* radiation transport equation (SRTE) to determine the line-of-sight (LOS) diffuse radiant intensity $I_0(\Omega_0)$ along a refracted path in a direction specified by solid angle Ω_0 [Chandrasekhar, 1960]:

$$I_0(\Omega_0) = t_s\, I_s(\Omega_s) + \int_{t_s}^{1} J_{s'}(\Omega_{s'})\, d\, t_{s'} = \textit{boundary term} + \textit{path radiance}\ (\textit{respectively})\,. \qquad \textbf{(19)}$$

This equation states that the observed spectral radiant intensity at the sensor (path length $s = 0$) equals the sum of two terms. The first term is the spectral radiant intensity directed towards the sensor a distance s away along the refracted path, $I_s(\Omega_s)$, attenuated by the foreground path transmittance t_s. The integrand of the path transmittance integral (the second term) contains the intervening source radiation $J_{s'}(\Omega_{s'})$ directed towards the sensor. The transmittance, radiant intensity, and source terms are all functions of spectral frequency, ν, but the labeling of that dependence has been suppressed for notational simplicity.

The SRTE appears deceptively simple; in truth, it is not. The equation for the source term J depends on the radiant intensity I, so these terms are coupled. Furthermore, if the LOS end point s is a surface (ground or object), then I_s depends on both the emission from that surface and the angular reflectance of the impingent flux; naturally, this flux is itself a function of radiant intensity. Bi-directional Reflectance Distribution Functions, BRDFs, provide the most general description of the surface reflectance, and Section 2.1.1 emphasized the importance of modeling this reflectance with physics-based models such as the Maxwell-Beard parameterization. Finally, although MODTRAN6 introduces a line-by-line capability, MODTRAN has traditionally been a band model algorithm focused on efficiently and accurately computing spectral channel radiances $\langle I \rangle$, not monochromatic values. The MODTRAN band model generates LOS spectral channel transmittances $\langle t \rangle$, but these values cannot be directly substituted for t in the SRTE to calculate $\langle I_0 \rangle$ unless both I_s and J_s do not vary significantly over the spectral channel.

MODTRAN7 will compute the spectral channel Stokes vector intensities, $\langle \mathbf{I} \rangle \equiv [\langle I \rangle, \langle Q \rangle, \langle U \rangle, \langle V \rangle]^{\mathrm{T}}$. The Stokes parameters will be obtained by solving the integral form of the *vector* radiation transport equation (VRTE) for *an atmosphere containing aerosols and clouds with equal numbers of randomly oriented particles and their mirror symmetric counterparts*. Requiring a macroscopically isotropic and mirror-symmetric scattering medium (ISM) greatly simplifies the polarimetric radiation transport. For the

ISM atmosphere, there is no change in polarization state due to extinction, and scattering matrices only depend on scattering angle. The ISM assumption is extremely reasonable for most terrestrial atmosphere applications. BRDF based treatments of surface reflectance and emission from the locally spherical hard Earth will produce the most dominant source of polarization for Earth viewing lines-of-sight.

The monochromatic VRTE under ISM conditions is

$$\mathbf{I}_0(\Omega_0) = t_s\, \mathbf{I}_s(\Omega_s) + \int_{t_s}^{1} \mathbf{J}_{s'}(\Omega_{s'})\, d\, t_{s'} \quad . \tag{20}$$

The Stokes intensities, **I**, and source function, **J**, are 4-element column vectors. The line-of-sight source term has 3 components:

$$\begin{aligned} \mathbf{J}_s(\Omega_s) = \quad & (1-\omega_s) B(T_s)\, \mathbf{I}^{\mathbf{0}} \quad + \omega_s\, \mathbf{Z}_s\left(\Omega_s, \Omega_s^{ET}\right) \mathbf{I}^{ET}\, t_s^{ET}\, I^{ET} \;+\; \omega_s \int_{4\pi} \mathbf{Z}_s(\Omega_s, \Omega')\, \mathbf{I}_s(\Omega')\, d\Omega' \\ & = \textit{local thermal emission} \;+\; \textit{single scatter solar / lunar} \;+\; \textit{multiple scatter solar / lunar} \quad . \end{aligned} \tag{21}$$

The first term, the thermal emission, is the product of the Planck blackbody emission $B(T_s)$ at local temperature T_s, the unit vector $\mathbf{I^0} \equiv [1, 0, 0, 0]^T$ for unpolarized light, and the local emissivity, equal to one minus the single scattering albedo at *s,* ω_s. The latter two terms in the equation for $\mathbf{J}_s(\Omega_s)$ are the path scattered radiance. The single scatter solar/lunar (ET = extra-terrestrial) radiation is the product of the top-of-atmosphere (TOA) solar/lunar irradiance intensity I^{ET}, the scattering point to sun transmittance t_s^{ET}, the source Stokes vector, $\mathbf{I}^{ET}$, the normalized scattering phase matrix, $\mathbf{Z}_s(\Omega_s, \Omega_s^{ET})$, and the single scattering albedo. The solar source is unpolarized, so $\mathbf{I}^{ET} = \mathbf{I^0}$; as discussed in Section 2.3.4, the lunar source is linearly polarized, so that in its most general form, $\mathbf{I}^{ET} = [1, Q^{lunar}/I^{lunar}, U^{lunar}/I^{lunar}, 0]^T$. The multiple scatter radiation is the integral over all directions (4π steradians) of the incoming polarized diffuse radiation scattered into the LOS.

When the line-of-sight terminates at the ground, *s = gnd*, the surface term includes both emissive and reflective components:

$$\mathbf{I}_{gnd}(\Omega_{gnd}) = B(T_s)\, \boldsymbol{\varepsilon}_{gnd}(\Omega_{gnd}) + \int_{2\pi} \mathbf{Z}_{gnd}(\Omega_{gnd}, \Omega')\, \mathbf{I}_{gnd}(\Omega')\, \mu'\, d\Omega' \quad . \tag{22}$$

The MODTRAN7 ground emission 4-vector will include non-zero I and Q (equivalently, I_v and I_h) components. The MODTRAN7 ground phase matrix, $\mathbf{Z}_{gnd}(\Omega_{gnd}, \Omega')$, models the reflections in the direction of the sensor Ω_{gnd} over the hemisphere of down-welling Stokes vectors, $\mathbf{I}_{gnd}(\Omega')$.

The scattering and ground phase matrices, $\mathbf{Z}_s(\Omega_s, \Omega')$ and $\mathbf{Z}_{gnd}(\Omega_{gnd}, \Omega')$, are specified in the *global* or measurement coordinate system, which, for terrestrial atmospheric problems, is defined so that the perpendicular electric field component is directed perpendicular to the vertical plane containing the sensor LOS. The fundamental quantity that describes the ISM molecular and particulate scattering of polarized radiation for scattering angle Θ is the Stokes scattering matrix, which is defined in the *local* scattering plane with 6 non-zero elements (described in Section 2.1.2.2). The fundamental quantity that describes the ground reflectance is the polarimetric BRDF, which is defined in the *local* reflection plane and will be characterized in MODTRAN7 via Maxwell-Beard and ocean surface pBRDF models.

For discrete ordinate methods described in the Section 2.2.2, the elements of the Stokes scattering matrix are expanded in generalized spherical functions. The coefficients in these expansions are computed with a T-matrix scattering model, such as the ones described in Section 2.1.2.6. The surface pBRDF matrix elements must be also be expanded in appropriate series for integration into discrete ordinate scattering models.

The Stokes scattering and pBRDF matrices are related to the phase matrices by the equation $\mathbf{Z}(\Omega, \Omega') = \mathbf{R}(\pi - \beta)\ \mathbf{F}(\Theta)\ \mathbf{R}(\alpha)$, where $\boldsymbol{R}$ is a rotation matrix, and α and β are angles between frames of reference [Mishchenko *et al.*, 2002; 2006]. The method MODTRAN7 and P-MCScene will use to compute the phase matrix from the Stokes scattering elements is described in Appendix A.

2.2.1 Unifying Radiometric (Scalar) and Polarimetric (Vector) Calculations

For the development of MODTRAN4P, the polarimetric version of MODTRAN4, complementary polarimetric versions of each of MODTRAN4's radiometric radiative transfer routines were developed. For example, MODTRAN4P routine `ssrad.f` computed band model single scatter solar radiant intensities, and routine `ssradP.f` computed the band model single scatter solar Stokes vector intensities. The problem with this construct is that the polarimetric algorithm quickly became antiquated as radiometric routines were upgraded and polarimetric routines ignored.

To avoid this divergence, a vector/matrix rank input, NPOLAR, has been introduced into MODTRAN7. Distinct routines will no longer be used to solve the radiometric and polarimetric problems. Instead, single routines will solve

- the radiometric problem when the input rank is NPOLAR = 1,
- the linear polarization problem when the input rank is NPOLAR = 3, or
- the linear plus circular polarization problem when the input rank is NPOLAR = 4.

There is a danger that the processing speed of radiometric calculations may be adversely impacted due to the use of vector/matrix manipulations to perform scalar arithmetic. However, this decrease in computational speed is expected to be negligible, and warranted given the advantage of having unified routines for the radiometric and polarimetric problems.

Unfortunately, this unifying construct will not be fully applicable to the multiple scattering modules. As discussed in the next few sections, MODTRAN6 uses the DISORT2 scattering algorithm to compute thermal scatter and solar multiple scatter segment intensities; MODTRAN7 will use the VDISORT3 scattering algorithm to compute the complementary segment Stokes vector intensities. The good news is that VDISORT3 does include an option to solve either the rank 3 (linear polarization) or the rank 4 (linear + circular polarization) problem.

MODTRAN7 has been set up as a branch of the MODTRAN6 SVN configuration control system [Collins-Sussman *et al.*, 2016]. As MODTRAN7 is developed, upgrades and corrections will undoubtedly be made to the publicly distributed MODTRAN6 model. Having MODTRAN7 as a branch of MODTRAN6 will help insure that these corrections get imported into MODTRAN7.

2.2.2 VDISORT3 Evaluation

MODTRAN6 uses the DISORT model [Stamnes *et al.*, 1988; 2000] to solve the plane-parallel atmosphere scalar multiple scattering problem using an approach originally conceived by Chandrasekhar [1960]. Each atmospheric layer is defined by its nadir optical depth, a single scattering albedo, and a scattering phase function. Temperatures are defined at level boundaries. Solar irradiance enters the top-of-atmosphere (TOA) at a fixed polar (zenith) angle, and the ground or bottom-of-atmosphere (BOA) reflectance and emissivity is modeled via a BRDF that depends on incident and reflected polar angles and on the relative azimuth angle between the incident and reflected directions. The SRTE is an integral differential equation in nadir optical depth τ that also depends on the cosine of the polar (off-nadir) angle μ and on relative solar azimuth angle ϕ. The solution to the SRTE is expanded in a Fourier series in $\cos(m\phi)$, producing a distinct τ- and μ-dependent differential equation for each integer value of m. The dependence on the cosines of polar angles is discretized using a double Gaussian representation on the domain [–1, 1]. Analytic particular and general solutions are derived for the τ-dependent problem in each

layer. Boundary (BOA and TOA) and continuity (between layers) conditions are solved to determine the set of unknowns constants, producing the final solution.

The DISORT procedure was originally vectorized for solving the polarimetric problem in 1999 [Schulz *et al.*, 1999]. Unfortunately, the original VDISORT model, integrated into MODTRAN4, had some limitations that adversely affected its usefulness: (i) the Stokes V component for non-Rayleigh scattering was incorrect, (ii) the lower boundary was modeled as Lambertian, (iii) results at arbitrary polar angles were poorly modeled, and (iv) a bug led to errors mainly in the Q Stokes parameter [Stamnes, 2015]. As part of a US Air Force funded effort, Contract No. FA9453-14-1-0237, led by Knut Stamnes and scheduled to be completed later this year, VDISORT was upgraded and modernized for future integration into MODTRAN. The new software product, dubbed VDISORT3,

- provides significant speed enhancement, reducing the computation time for the algebraic eigenvalue problem by a factor of 8,
- enables solution to either the more rapid linear polarization (I, Q, and U) problem or the full linear plus circular polarization (I, Q, U, and V) problem,
- improves the 4-vector approach providing 'exact' solutions,
- corrects a bug in the original VDISORT treatment of the Lambertian surface,
- agrees with benchmark calculations [Kokhanovsky *et al.*, 2010; Garcia and Siewert, 1989; Siewert, 2000],
- includes a Gaussian rough sea surface pBRDF model, and
- generates output at arbitrary angles.

VDISORT3 validation case results are illustrated in Figures 15 and 16.

For the DOE Phase I effort, SSI evaluated a preliminary distribution (July 2015) of the VDISORT3 software. My comments to Professor Stamnes and his *responses* are paraphrased here:

Comment: I was very pleased to see delta-M phase function expansions, the integral representation of user angle radiances, and a BRDF surface option.

Comment: Are there instructions for defining the polarimetric BRDF surface?

Response: *The definition is provided by the following equation:*

$$\mathbf{I}_{refl}(\tau^*,\mu',\phi') = \int_0^1 d\mu \int_0^{2\pi} d\phi\ \mu\, \mathbf{R}(\mu,\mu',\phi'-\phi)\mathbf{I}_{inc}(\tau^*,\mu,\phi) + \frac{\mu_0}{4\pi}\mathbf{R}(\mu_0,\mu',\phi'-\phi_0)\mathbf{S}_b(\tau^*,\mu_0) \quad ,$$

"*where* μ *and* μ' *are cosines of the polar angles* θ *and* θ'*, and* ϕ *and* ϕ' *are the corresponding azimuth angles. The downward Stokes vector at the surface is denoted* $\mathbf{I}_{inc}(\tau^*, \mu, \phi)$*, and* $\mathbf{S}_b(\tau^*, \mu_0) = F_0[1, 0, 0, 0]^T \exp(-\tau^*/\mu_0)$ *is the attenuated unpolarized solar irradiance of magnitude* F_0 *at the TOA.* $\mathbf{R}$ *is a* 4×4 *reflectance matrix that depends on the surface properties; here we use a rough ocean surface as an example.*"

Comment: Can you provide a polarimetric thermal radiance test case?

Response: *A thermal case will be included in the final delivery*

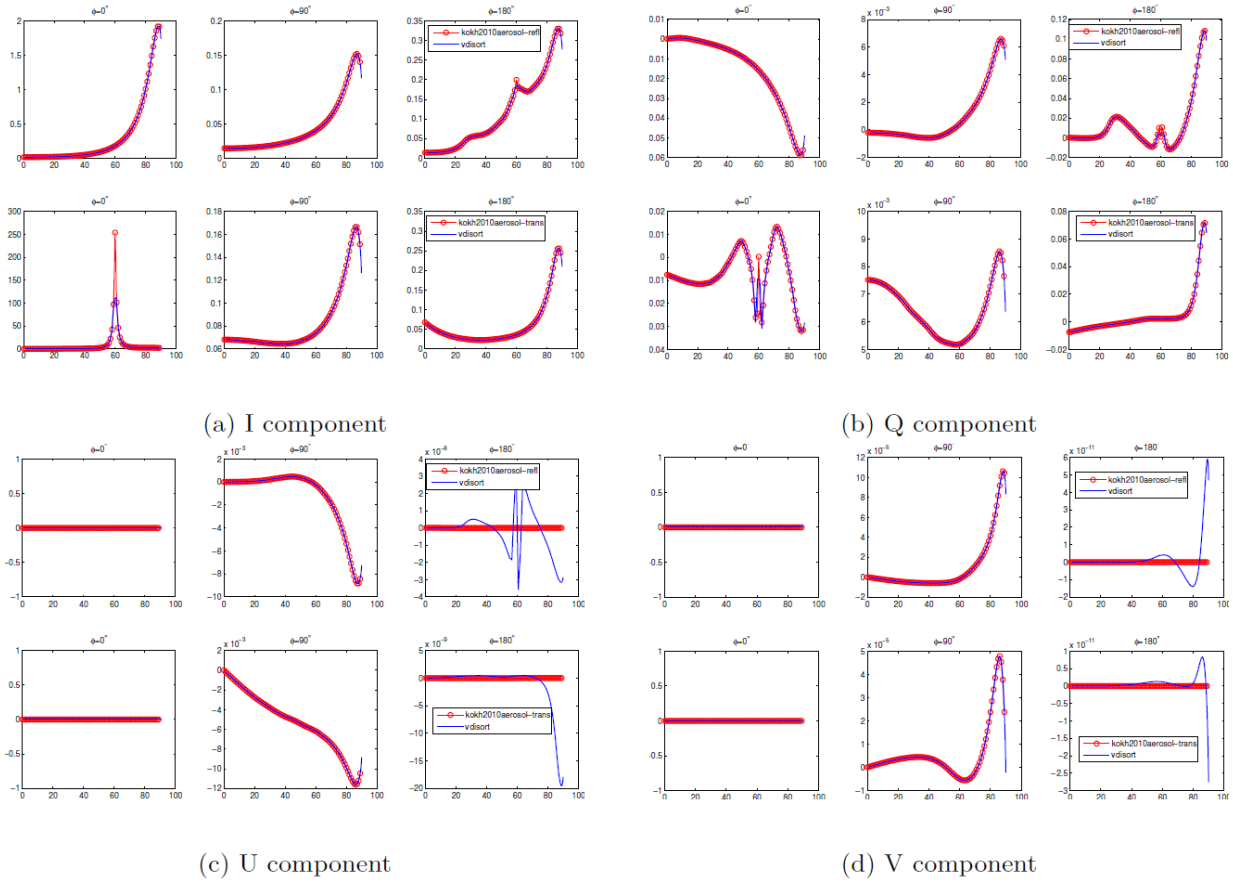

Figure 15. VDISORT3 Comparison to the Mie Particle Aerosol Layer Benchmark Test Case [Kokhanovsky *et al.*, 2010]. The cosine of the solar zenith, the single layer optical depth, the single scattering albedo and the ground surface reflectance were set to 0.5, 0.3262, 1.0, and 0.0, respectively. For each Stokes parameter, the top three plots contain 60° off-nadir views from the top of the layer at relative solar azimuths of 0°, 90°, and 180°; the bottom three plots contain 60° off-zenith views from the bottom of the layer at relative solar azimuths of 0°, 90°, and 180°. Discrepancies only arise when Stokes parameter component intensities are 3 orders of magnitude below the total intensity.

Comment: I modified the two Kokhanovsky *et al.*, [2010] single layer test cases that you delivered (Rayleigh and aerosol), inputting the vertical zenith angles from their Tables A1 - A6 [0°, 20°, 40°, 60°, 80°, and 89°]. Rayleigh comparisons are excellent! Unfortunately, the aerosol test case results were not good.

Response: The arbitrary angle capability was still in development in July 2015. The calculations now agree at all angles, Figure 15.

Comment: Can you add the Kokhanovsky cloud layer case?

Response: The Kokhanovsky cloud layer case will be added to the distribution.

Comment: All test cases are for a single frequency, with no molecular absorption and no more than 2 layers. When we had run the original VDISORT with tens of layers, significant problems with the linear algebra routines were observed.

Response: A new multi-layer test case that simulates an actual atmosphere will be demonstrated.

Based on these responses, SSI is encouraged that VDISORT3 will provide the capabilities required by MODTRAN7.

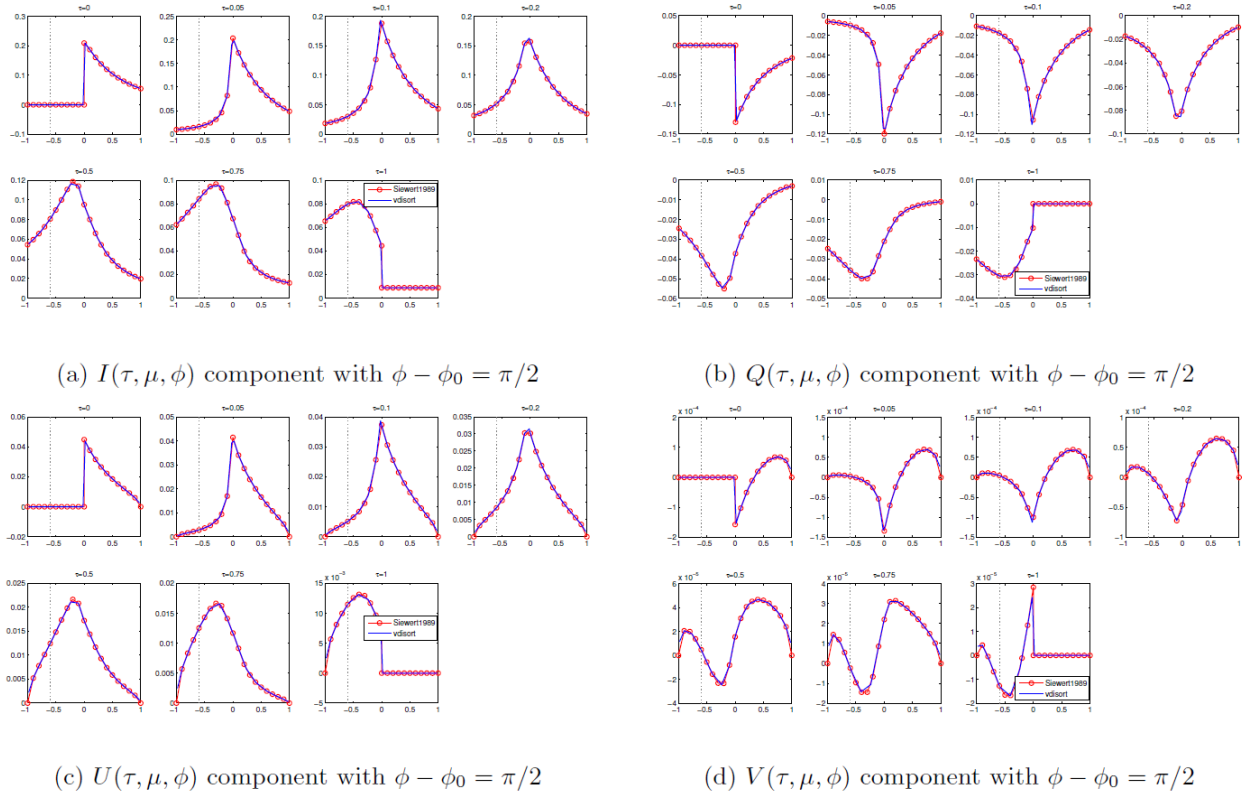

(a) $I(\tau, \mu, \phi)$ component with $\phi - \phi_0 = \pi/2$

(b) $Q(\tau, \mu, \phi)$ component with $\phi - \phi_0 = \pi/2$

(c) $U(\tau, \mu, \phi)$ component with $\phi - \phi_0 = \pi/2$

(d) $V(\tau, \mu, \phi)$ component with $\phi - \phi_0 = \pi/2$

Figure 16. Lambert Surface Benchmark Test [Garcia and Siewert, 1989], the L=13 Problem. The total layer nadir optical depth for this test case was 1.0, the cosine of the solar zenith angle was 0.2, the aerosol single scattering albedo was set to 0.99, and the sensor is placed at nadir optical depths of 0.0 (top of layer), 0.05, 0.1, 0.2, 0.5, 0.75, and 1.0 (bottom of layer). With a relative azimuth of 90°, the cosine of the polar angle is varied from –1.0 (looking straight up) to +1.0 (looking straight down). The Lambertian lower boundary was modeled with a surface albedo of 0.1.

2.2.3 Spherical VDISORT3

Integrating DISORT into scalar MODTRAN6 was not a simple process. The DISORT module was designed to solve the multiple scattering problem for one spectral point at a time, and all arrays were re-initialized to zero each time DISORT was called in the original integration. In addition, the arrays were not dynamically allocated. Before these issues were addressed, the single largest MODTRAN processing bottleneck was the DISORT zeroing of arrays! For MODTRAN6, each DISORT array was analyzed to determine the minimum dynamic allocation and its initialization requirements. An analogous optimization will be required for VDISORT3.

DISORT was also optimized to limit redundant calculations. Array initializations that only need to be defined once are now performed prior to initiation of the spectral loop. In addition, symmetry considerations were exploited to eliminate duplicate calculations. This may be related to the speed up described in Section 2.2.2 (the first bulleted item). If review of VDISORT3 detects redundant calculations similar to those in DISORT, VDISORT3 will be streamlined to eliminate those calculations.

The most significant change made to DISORT for integration into MODTRAN6 is the upgrade to deal with the fact that DISORT is a plane-parallel atmosphere model, while MODTRAN treats the spherical refractive geometry problem. As illustrated in Figure 17, this is a classical square peg in a round hole problem. The most severe issue arises for downward line-of-sight limb paths. In DISORT, all downward paths hit the ground; MODTRAN models limb paths that pass through a tangent altitude before eventually exiting the TOA. To fix this problem, the input of DISORT is generalized to accept

arrays of polar and relative solar azimuth angles for each segment along a line-of-sight. Segment solar and thermal radiances are returned by the upgraded DISORT model. A number of additional modifications are required, but describing those details seems unnecessary here. The point to be made is that VDISORT will also need to be upgraded for compatibility with MODTRAN7's spherical refractive geometry.

Figure 17. Illustration of the Challenge Associated with Integration of the Plane-Parallel Atmosphere DISORT scattering model into MODTRAN's Spherical Refractive Geometry.

2.3 Integrate MODTRAN4P Data/Software

The objective of this task was to incorporate the usable MODTRAN4P data and code into MODTRAN7. As discussed above in section 2.2.1, in MODTRAN4P, the scalar and polarimetric RT routines were entirely separate, whereas MODTRAN7 will have a unified approach in which the calculations and array dimensions are parametrized by the number of Stokes components required in the output. As a result, relatively little of the MODTRAN4P software will be reusable in MODTRAN7. The reusable components are just the polarimetric model aerosol data sets, and the input data checking for scattering Mueller matrices and their GSF expansion coefficients which was built into the MODTRAN4P file reader subroutines. Integration required (1) the definition of a data structure; (2) definition of data files, coding file writers and readers, and modifications to MODTRAN to use the data structure. Test calculations were performed for (3) Solar (unpolarized) and (4) Lunar (partially linearly polarized) single scattered radiance in the visible spectral range. Each of these activities will be discussed in a subsection below.

2.3.1 Data Structure for Particulate Data

The polarimetric aerosol data described above in section 2.1.2.5 were aggregated into two ASCII data files (one for scattering matrix elements and one for expansion coefficients), each containing data for all six of the aerosol models treated. Each file is over 300 Mbytes in size. MODTRAN4P read both these files as part of the initializations for any polarimetric RT calculation, and stored the data in a Fortran named common block. Since MODTRAN6 is structured with Fortran-95 modules and derived types, a different method of storage is required.

When reviewing the MODTRAN4P aerosol data for use in MODTRAN7, one concern was the sheer size of the data, and some ways to decrease the data storage requirements were considered. For example, for non-polarimetric RT, the data required to describe an aerosol or cloud include the extinction and absorption coefficients, the phase function on a set of 146 scattering angles, and the Legendre expansion moments for the phase function, up to some specified degree. These must be given for a grid of spectral points, for interpolation to the spectral frequencies in an RT calculation. For the humidity-dependent boundary layer and tropospheric aerosols, these arrays have another dimension: data must be saved for

eight different relative humidity values in order to interpolate to the local relative humidity. For a polarimetric RT calculation, the data requirements are larger: in addition to the extinction and absorption coefficients, four (or six) nonzero scattering matrix elements, and six sets of Generalized Spherical Function expansion moments, must be saved.

One could consider eliminating the tabulated phase function data, and calculating the phase function from the Legendre expansion. If the Legendre moments are saved up to a high enough degree to give an accurate representation of the phase function, then the phase function is redundant; however the number of moments needed may be quite large. This will be true for aerosols with large particle size distributions compared to the range of wavelengths in an RT calculation, or for aerosols with only moderately large size distributions but complex particle shapes. Multiple calculations of the phase functions will be prohibitively slow. Alternatively, one may truncate the Legendre expansion at some manageable degree and calculate an approximate phase function, either directly from the aerosol data or using the delta-M approximation [Wiscombe, 1977]. However, for aerosols that require high-degree Legendre expansions, the resulting approximate phase function may be a poor approximation to the original, or may be ill-behaved and unphysical.

As an example, Figure 18 illustrates the unit-normalized scattering phase function and some lower-degree approximations for a water cloud, with a size distribution of spherical water droplets having mode radius 12 μm, in the near-infrared (7050 cm^{-1}, λ = 1.418 μm). The original scattering data are from [Macke, 2001], spectrally interpolated to the calculation wavelength, with Legendre moments up to maximum degree 512. The black curve shows the phase function itself. The full Legendre expansion is not shown, as it is nearly indistinguishable from the raw phase function. The red curve is generated from the Legendre moments truncated to degree < 32; the green curve is the delta-M approximation with truncation degree M = 8; and the blue curve is the delta-M approximation with M = 32. The delta-function contribution in the forward direction is not shown in either of the delta-M curves. The y-axis scale is logarithmic, so that wherever an approximate phase function is negative, it is not shown. None of the truncated Legendre approximations represent the phase function accurately. The 32-term Legendre approximation (without delta-M) has significant ringing, with unphysical negative values over almost half the angular range, and is often an order of magnitude larger than the actual phase function. Even the 32-term delta-M approximation has much larger oscillations in value than the phase function, and is negative in a small region around 101° scattering angle. Unfortunately, this exercise verifies that both representations of the scattering matrix are needed.

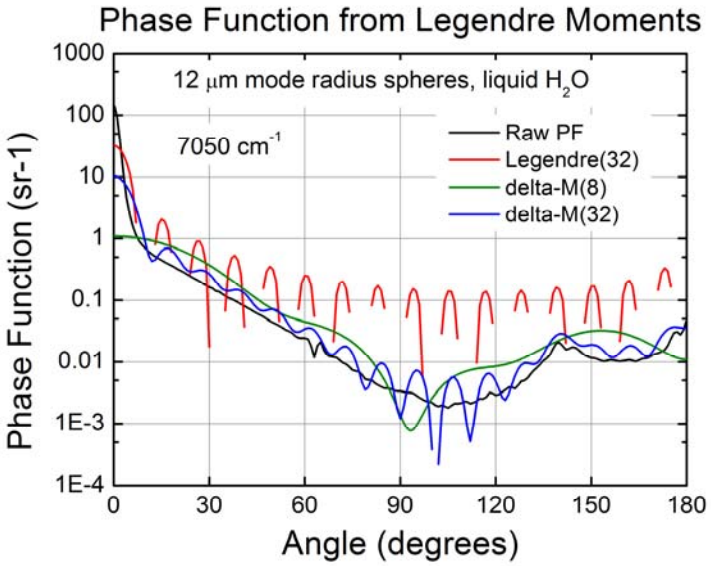

Figure 18. Comparison of Scattering Phase Function with Truncated Legendre Approximations.

A preliminary version of the data structure for scattering properties of the built-in aerosol and cloud models was designed. The requirements were that it should contain the scattering matrix elements and GSF expansion coefficients required for a calculation, which could be scalar, polarimetric with only linear polarization, or fully polarimetric; aerosol properties might either depend on relative humidity (with a set of eight tabulation values), or be independent of it. Aerosol data were assumed to be tabulated on a fixed grid of 788 wavelengths from 0.2 to 299.9 μm (the standard MODTRAN wavelengths for built-in aerosol and cloud spectral optical properties). Aerosols were assumed to be ISM (macroscopically Isotropic and Symmetric scattering Media), with data either from Mie or T-matrix calculations, so that there may be either 4 or 6 unique nonzero elements in the full Mueller scattering matrix. The extinction and absorption coefficients as functions of wavelength and relative humidity were not required to be saved in the data structures, as these data for the built-in model aerosols are already saved in arrays in the aerosol data module in the MODTRAN code.

The built-in MODTRAN model aerosols are each assigned to a specific altitude region in the atmosphere, but within that region an aerosol's optical properties do not vary with altitude. Further, since the aerosols are assumed to be ISM, the scattering matrix depends only on the included scattering angle, and not on the incident and scattered polar and azimuthal angles with respect to any fixed direction. (Note that both of these assumptions may need to be relaxed as part of the work in Phase II. In particular, as discussed in subsection 2.1.2.3, scattering must depend on the incident and scattered polar angles, and at least on the difference in azimuth angles, when treating cirrus clouds where the ice crystals tend to be horizontally oriented.)

The current version of the data structure is as shown in Figure 19. All the array components of the data type are allocatable; arrays for the scattering matrix elements and expansion coefficient sets can be left un-allocated if they are not required for a calculation. For instance, for a scalar multiple scattering calculation, only arrays `a11` (the intensity phase function) and `alp1` (the phase function's Legendre expansion) need be allocated. For a single scattering calculation with only linear polarization considered, scattering matrix arrays `a11, b12, a22` (if needed), and `a33` will be allocated, but `b34` and `a44`, and all the T-matrix coefficient arrays, will be left un-allocated.

```
! Derived type for aerosol scattering data, with or without
! relative humidity dependence.
! For aerosols that do not depend on relative humidity,
! allocate the arrays with the relative-humidity dimension = 1.
type builtinaer
  ! Set of angles used for scattering matrix elements.
  real, allocatable :: angles_deg(:)
  real, allocatable :: cosines(:)

  ! Scattering matrix elements.
  ! Indexing order is  (angle, %rh, wlen) .
  real, dimension(:,:,:), allocatable :: a11, b12,a22,a33,b34,a44

  ! Maximum degree with nonzero components for T-matrix expansion
  ! coefficient sets, limited by max degree used.
  ! Indexing order is  (%rh, wlen) .
  integer, dimension(:,:), allocatable :: nlmxnz

  ! T-Matrix (Generalized Spherical Function) expansion
  ! coefficient sets.
  ! Indexing order is  (l, %rh, wlen) ,
  ! where  l  is expansion degree (beginning at ZERO).
  real, dimension(:,:,:), allocatable :: alp1, alp2,alp3,alp4, &
          bet1,bet2
end type builtinaer
```

Figure 19. Fortran Derived Type for Aerosol Scattering Data, Optionally Scalar or Polarimetric.

2.3.2 Code Modifications

A structure was defined for the aerosol data files, and off-line programs were written, to convert the Mueller matrix and T-matrix coefficient data. A module for the aerosol data type was written, and the MODTRAN7 code was modified in order to use the new data type.

One design choice in MODTRAN4P that may have affected its performance was that the polarimetric aerosol data for *all* the aerosols were in two text files, one for the scattering matrix elements and one for the expansion coefficients. Both these files had to be read from the beginning, as part of the setups for each polarimetric calculation; unused aerosols had to be read and skipped, and the aerosols used in the calculation had to be read from the beginning of the data spectral range, discarding text lines until the beginning of the calculation spectral range was reached. MODTRAN7 will use two Fortran direct-access binary files for each aerosol, one for scattering matrix elements and one for expansion coefficients. Each file begins with a header record containing overall information about the file: the record size, numbers of wavelengths, relative humidities, scattering angles, and polarization components, lists of the wavelengths, percent relative humidities, and angles, and a descriptive character string. For Mueller matrix files, the data for each successive spectral point are in a separate record; data records are in ascending order of wavelength, beginning in the second record (immediately after the header record). For T-matrix expansion coefficient files, data for one wavelength occupy six successive records, one for each coefficient set (α_1, α_2, α_3, α_4, β_1, and β_2); these groups of records are in ascending order of wavelength. The advantages of using direct-access binary files are that the data need not be converted from ASCII text to machine words, and that individual file records are directly addressable, so that the reader only needs to read the file header record and the data records that cover the current calculation's spectral range. Since each model aerosol's data will reside in its own pair of files, there is no need to skip over unused aerosols; only the aerosols used in the calculation need be read. The data conversion programs deal with the difference between the MODTRAN4P and MODTRAN7 spectral grids for aerosol data, by interpolating the scattering matrix elements and the expansion coefficients at short wavelengths, from the sparser MODTRAN4P spectral sampling points to the MODTRAN7 points. The conversion of the existing text data files takes some time, but only needs to be done once, in order to create the binary data files.

A Fortran-95 module, `builtinaer_mod`, was written, to manage the `builtinaer` derived type and to provide support routines. In addition to the type definition, it contains readers for both files, a routine to return the scattering matrix for a given wavelength, humidity, and scattering angle, a routine to return T-matrix expansion coefficients, and a cleanup routine to deallocate arrays in an object of the type.

As a test of the data conversion code and the MODTRAN7 code modifications, and in order to perform test calculations, the data for the Rural aerosol were converted to two files, `ruralmuel.bin` with the scattering matrix elements, and `ruraltmat.bin` with the GSF expansion coefficients.

An instance of the data structure was added to the MODTRAN7 aerosol module, for the boundary layer aerosol, with the plan being to replace this with an allocatable array, with one element for each aerosol region. Preliminary modifications were made to the code, to read and use the new polarimetric data for the Rural boundary layer aerosol if a calculation called for it.

The existing aerosol subroutines, which calculate aerosol phase functions, Legendre moments, and contributions to LOS segment optical depth, were also upgraded to take their values from the data structure when treating the Rural boundary aerosol. This is an improvement over MODTRAN's current treatment, in two ways. First, the existing Mie approximation for aerosol phase functions in single scatter was to interpolate over angle and frequency, from a fairly small, coarsely sampled basis set of representative aerosol Mie phase functions. The Mie functions from MODTRAN4P, calculated on finer grids of angles, wavelengths, and relative humidity, directly from model size distributions and material refractive index data, are closer to the physics and should be more accurate. Second, the DISORT treatment of multiple scatter in MODTRAN has used the analytic Henyey-Greenstein approximation for the scattering phase functions and their Legendre expansion moments. The difference between realistic

Mie phase functions and Henyey-Greenstein phase functions with the same asymmetry is illustrated in Figure 20; at left are the phase functions, and at right are the Legendre expansion moments for degree up to 16. The Henyey-Greenstein phase function is not an unreasonably bad approximation to the Mie phase function at sideward angles, but does not reproduce the peaks at the ends of the range, in particular the forward peak. This is because the Legendre expansion moments for the Henyey-Greenstein phase function are significantly smaller than those for the Mie phase function beginning at about degree $l = 5$, and decrease in magnitude much more precipitously with increasing degree; in the forward direction, as all the Legendre polynomials go to 1, the moments all add to produce the peak. The delta-M approximation compensates somewhat for this, by adding a delta-function in the forward direction, with strength determined from the magnitude of the first neglected expansion coefficient.

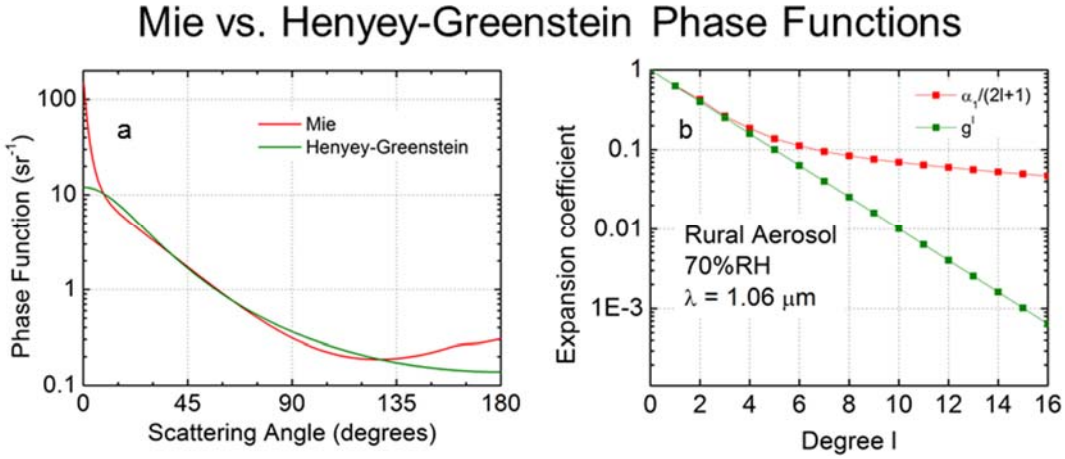

Figure 20. Comparison of Mie and Henyey-Greenstein Phase Functions with Identical Asymmetry Factors. At left, the phase functions themselves. At right, the Legendre expansion moments. The asymmetry factor $g = \alpha_1(1)/3$, where $\alpha_1(l) / (2l+1)$, for $l = 0, 1, \ldots$, are the Legendre moments of the Mie phase function.

The difference between the Henyey-Greenstein and Mie phase functions has a noticeable, but relatively small, effect in the Solar multiply scattered radiance calculation shown in Figure 21. The observer is at 2 km altitude, with the LOS reaching the ground at a 90° zenith angle; the Sun zenith angle is 45°, and the sensor-to-ground LOS is in the forward principal plane (0° relative azimuth).

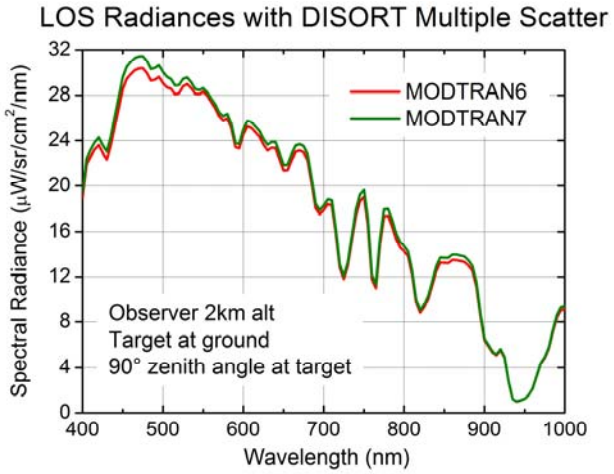

Figure 21. Comparison of MODTRAN6 LOS Radiance (using Henyey-Greenstein Phase Functions and Moments) to MODTRAN7 Result (using Mie) for an 8-stream DISORT Multiple Scatter Calculation.

After the preliminary software integration and testing, several polarimetric calculations were performed, as tests of the aerosol data structure, reader routines, and code changes, and to show the effects of single scatter from an unpolarized or partially polarized source. Two calculations were done for single Solar scatter and two for single Lunar scatter, with similar scattering geometries and the same spectral range. These are described in the next two subsections.

2.3.3 Single Scatter Solar Calculations

The solar single scatter calculations demonstrate the effect of single scatter from an unpolarized source, in a fully polarimetric calculation. The Rural aerosol was used as the boundary layer, with 23 km visibility, and with 72% average relative humidity. For both calculations, the Sun zenith angle was 45°; the sensor was at 1 km altitude, looking down. In the first calculation, the sensor nadir angle varies from +60° in the forward direction (on the same side of the nadir as the Sun), to -60°, in the reverse direction, with the Sun and sensor LOS both in the principal (vertical) plane. In the second calculation, the sensor LOS goes out of the principal plane; the nadir angle is fixed at 60°, and the azimuth angle is swept from -180° to +180°, to show nonzero values of the Stokes U (45°/135° linear polarization). Scattering geometries are shown in Figure 22 for the in-plane (left) and azimuth scan (right) cases. For both calculations, the spectral range was 400 to 700 nm, covering the visible regime, in which both Rayleigh and boundary aerosol scattering are significant. Plots will show the results at three wavelengths: Red (670 nm), Green (540 nm), and Blue (470 nm).

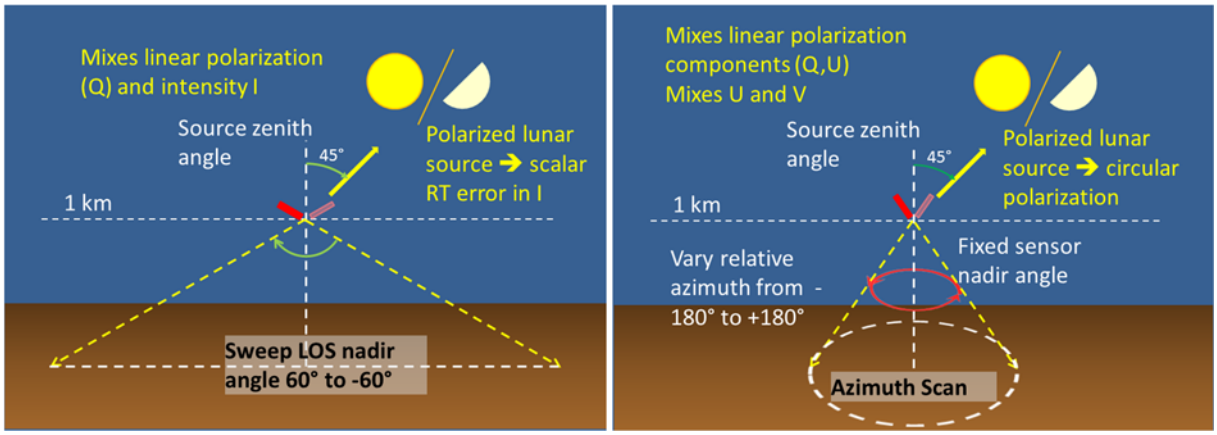

Figure 22. Source/Sensor Geometry for the Single Scatter Calculations. At left, the sensor-to-ground LOS is in the same plane as the path from scattering point to the Sun; the nadir angle is swept within the principal (vertical) plane. At right, the sensor nadir angle is fixed, and the relative azimuth of the sensor LOS is swept with respect to the direction to the Sun.

The nonzero Stokes components for the in-plane calculation are shown as functions of the LOS nadir angle in Figure 23 at left, and the degree of linear polarization at right. The Stokes components U and V are both zero. For single scatter from an ISM with either an unpolarized source, or a source that only has Q linear polarization, U must be zero in the principal plane, because there are no reference frame rotations. For single scattering from an ISM with an unpolarized source, V must always be zero. The scattering matrix element F_{12}, and thereefore Q, are exactly zero in the backscatter direction (nadir angle = -45°), and so the degree of polarization must also be zero there. The degree of linear polarization reaches 46.4% in the blue, and roughly 44% in both the red and green.

Figure 24 shows the nonzero polarization components for the single scatter Solar azimuth scan calculation (left), and the degree of polarization (right). Since the scattering plane is now generally not vertical, the reference frame rotation to the vertical plane mixes the Q and U linear polarization components; U is antisymmetric with respect to reflection about 0° relative azimuth (because the sense of rotation of the reference frame is reversed), whereas I and Q are symmetric.

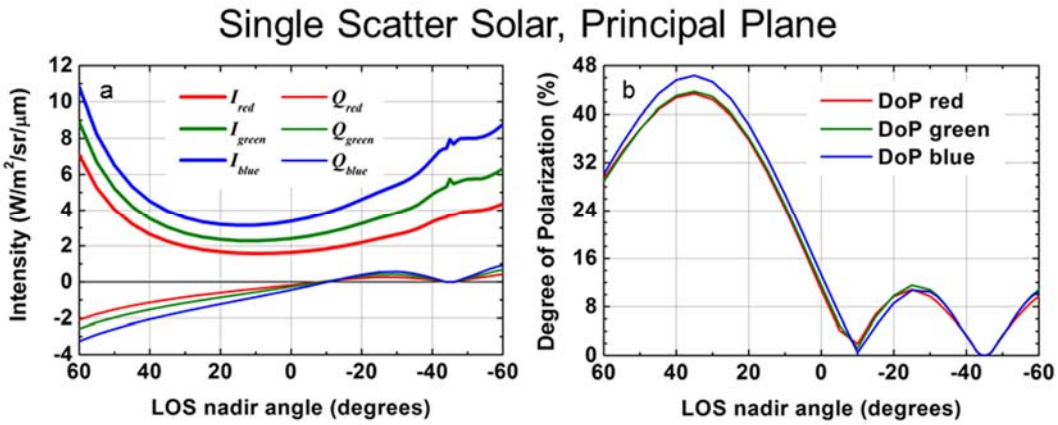

Figure 23. Results for Single Solar Scatter in the Vertical Plane. At left, the Stokes *I* (total intensity) and *Q* (0°/90° linear polarization) as functions of the sensor LOS nadir angle. At right, the degree of polarization.

The angle of polarization (AoP), *i.e.*, the major axis of the polarization ellipse with respect to the reference plane, or equivalently the angle of maximum linear polarization, is shown in Figure 24. Since in this case both *Q* and *U* components are generally nonzero, and since they have opposite reflection symmetries around 0° relative azimuth, the AoP is also antisymmetric in azimuth angle. The jump discontinuities in the AoP at roughly +/-135° occur because *Q* and *U* have coinciding zeroes, so that both the degree and angle of polarization are undefined there.

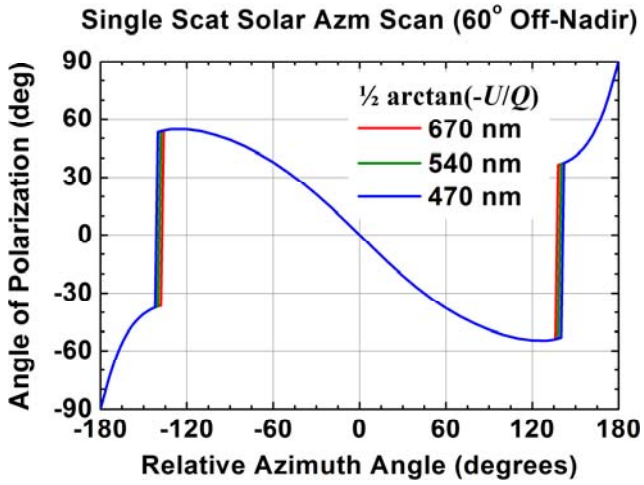

Figure 24. Angle of Polarization for Single Solar Scatter Azimuth Scan.

2.3.4 Single Scatter Lunar Calculations

The Lunar irradiance can be partially polarized, depending on the phase of the moon and the wavelength. The degree of linear polarization varies from roughly -1.2% to as much as +19%, with the maximum degree occurring somewhat after the last quarter; the maximum degree of polarization is largest in the near-UV and decreases with increasing wavelength, averaging roughly 8% across the visible spectrum [Pellicori, 1971]. The axis of polarization is either parallel or perpendicular to the scattering plane, *i.e.*, *with respect to the scattering plane*, the polarization component is all in the Stokes component *Q*. We expect the lunar single scatter to show a richer phenomenology than the solar case, due to the partial polarization of the source.

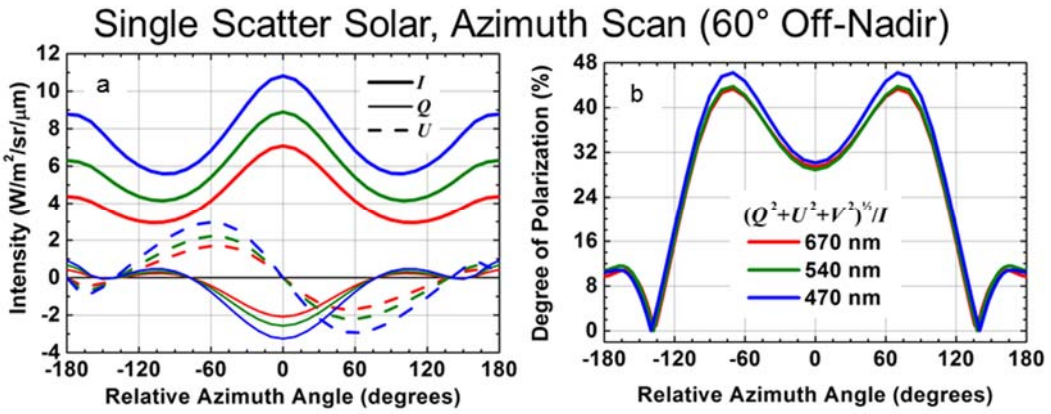

Figure 25. Results for Single Solar Scatter Azimuth Scan at 60° Nadir Angle. At left, the Stokes parameters *I*, Q, *U*, as functions of relative azimuth. At right, the degree of polarization.

Two singly-scattered lunar radiance calculations were performed, using the same atmosphere and spectral range, and similar source/sensor geometries as the solar calculations. For the first calculation, the sensor to ground LOS was in the same vertical plane as the source, and the sensor nadir angle was varied from 60° to -60°, just as in the solar case. For the second calculation, the sensor nadir angle was constant (but at a different value than was used for the Sun), and the relative azimuth varied from -180° to +180°. The sensor was looking down from 1 km altitude, through the Rural aerosol with 72% relative humidity and 23km visibility, for both calculations. The source zenith angle was 45° as before, but the source was the Moon at last-quarter, modeled as having 8% linear polarization entirely in the vertical plane (for computational convenience), so that the source Stokes vector was $\mathbf{I}_{\text{Moon}} = I_0 \, [\, 1,\ 0.08,\ 0,\ 0\,]^{\text{T}}$. The Sun/Moon/observer geometry is as shown in Figure 26, with the plane containing the Sun, Moon, and observer being vertical (the same as the polarization reference plane) at the observer's location.

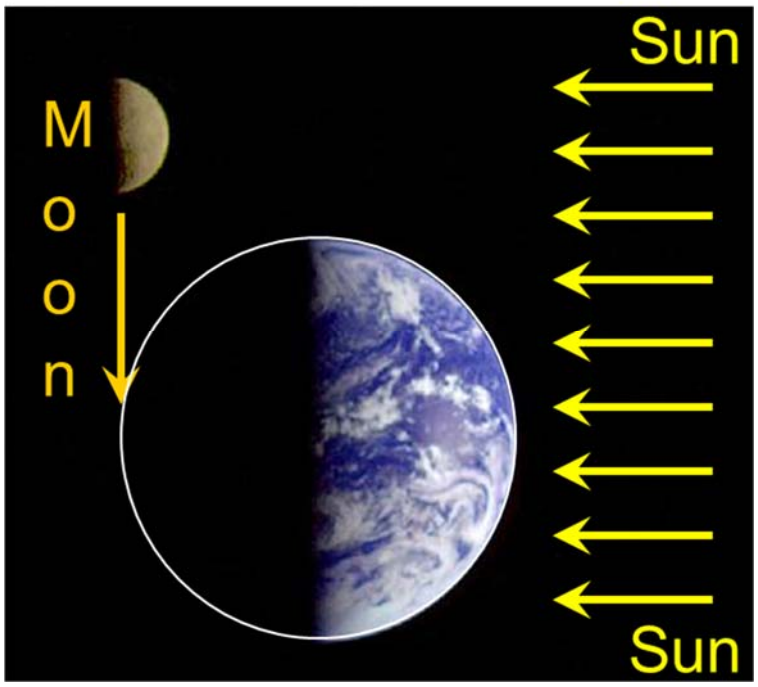

Figure 26. The Sun/Moon/observer geometry used for the Lunar single scattered radiance calculations. The plane containing the Sun, Moon, and observer is vertical at the observer's location.

One feature of single scatter from a source with partial linear polarization, not present for an unpolarized source, is that purely scalar RT will miscalculate the total radiance. This occurs because the off-diagonal scattering matrix element F_{12} mixes the incident polarization term Q with the total intensity I in the scattered Stokes vector, an effect not describable in scalar RT. The errors in total radiance between scalar and polarimetric calculations for our cases are shown in Figure 27; at left is the percent error for the nadir angle scan in the principal plane, and the panel at right shows it for the azimuth scan, with the sensor nadir angle fixed at 35°, the angle at which the error was maximized in the nadir angle scan. The scalar model error varies between roughly -1% and +4%.

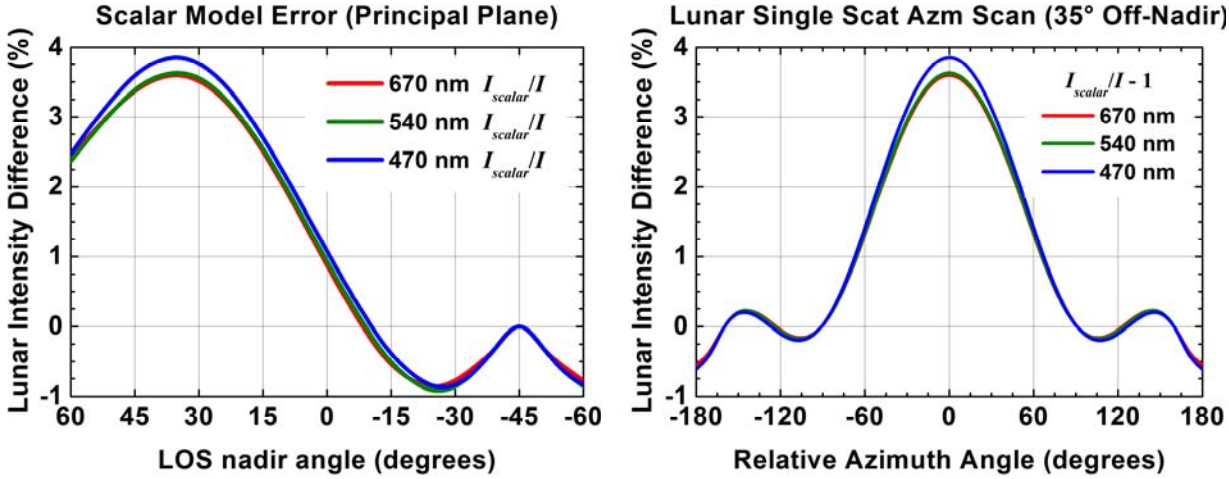

Figure 27. Percent Error in Scalar-Only Radiance Calculations for Lunar Single Scatter. At left, the variation of the scalar model error with nadir angle in the principal (vertical) plane. At right, the variation of the scalar model error with Sun/Sensor relative azimuth angle, with the nadir angle fixed at +35° (location of the maximum scalar model error in panel at left).

The nonzero Stokes components and the degree of polarization for the in-plane case are shown in Figure 28. Since the sensor LOS is in the principal (vertical) plane with the Moon, the Stokes U and V components are identically zero. The maximum degrees of linear polarization, which occur near 35° off-nadir, are 40% in the blue, and roughly 37% in the green and red. A local minimum occurs in the degree of polarization at the exact backscatter angle, -45°, where the F_{12} scattering matrix element goes to zero quadratically as the cosine of the scattering angle goes to -1.

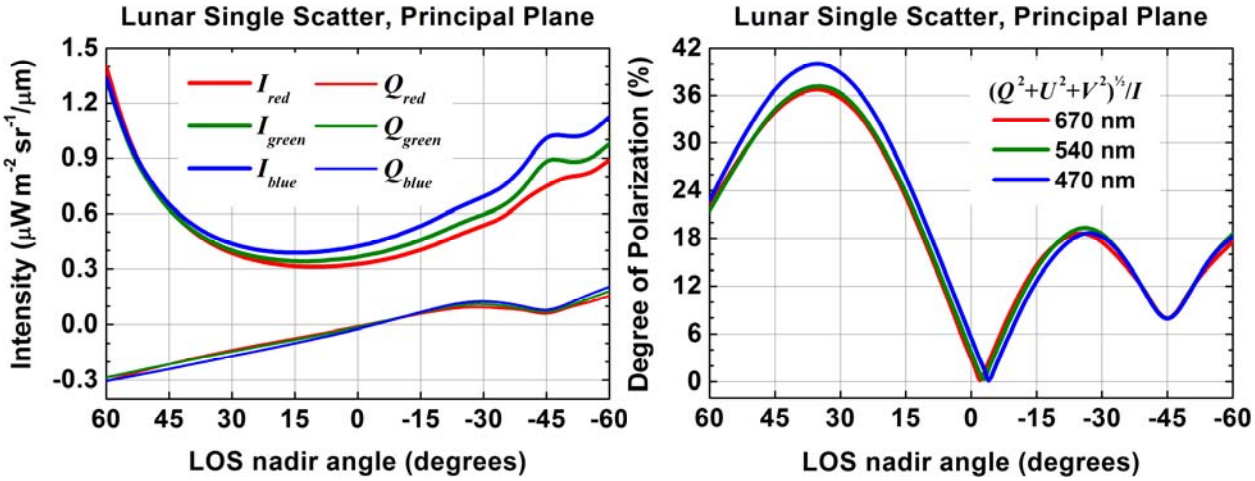

Figure 28. Results for Lunar Single Scatter Varying LOS Nadir Angle in the Principal Plane. At left, the nonzero Stokes components I and Q. At right, the degree of polarization.

The results for the azimuth scan are shown in Figure 29. The Stokes vector components are shown in the two panels on the left; the intensity *I* and linear polarization components *Q* and *U* are in panel (a) and the circular polarization *V* is shown in panel (b). The nonzero circular polarization appears when the sensor leaves the reference plane (which is also the plane of the incident polarization), because the scattering plane is different from the (vertical) reference plane; frame rotations into and out of the scattering plane mix the *Q* and *U* linear polarization components, and scattering from the aerosol mixes *U* and *V*. The circular polarization in this case is fairly weak; it is never above 1.3% of the total intensity. The total degree of polarization is shown in panel (c), and the angle of polarization is shown in panel (d). Due to the partial linear polarization of the source, the zeroes of the linear polarization components *Q* and *U* do not coincide (unlike what was seen in the solar scatter case). There are no zeroes in the degree of total polarization, nor in the degree of linear polarization (not shown), and the angle of polarization is a well-behaved function of the relative azimuth angle, with no discontinuities.

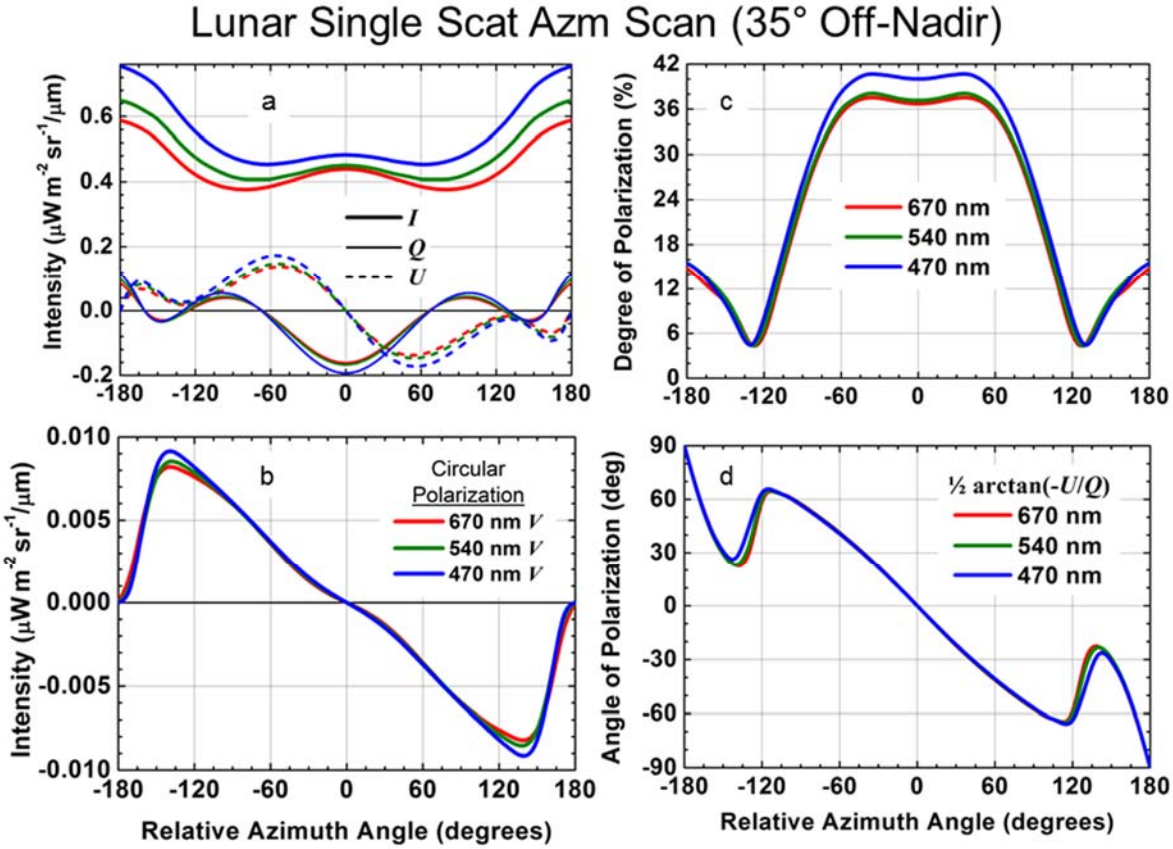

Figure 29. Results of Singly-Scattered Lunar Calculation with Azimuth Scan at 35° Sensor Nadir Angle. (a) The intensity *I* and linear polarization components *Q* and *U* of the Stokes vector vs. Sun/Sensor relative azimuth. (b) The circular polarization component *V*. (c) The degree of polarization. (d) The angle of polarization as a function of relative azimuth angle.

2.4 Implementation Plan for P-MCScene

A quick search on Google verifies that there is no shortage of Monte-Carlo based polarimetric radiative transfer models. The reason is clear. It is relatively straightforward to track changes in polarimetric state arising from individual atmospheric scattering or surface reflectance events. In addition, Monte-Carlo modeling provides the flexibility required to model complex structures and the 3D environment. Vectorizing 1D analytic scalar radiative transfer models and generalizing their polarimetric signature modeling to image real scenes is considerably more difficult.

Two challenges stand out for the polarimetric Monte-Carlo models. Monte-Carlo processing is notoriously slow. The standard deviation of the distribution of Monte-Carlo simulated results decreases proportional to the inverse square root of the number of trials. Thus, the number of trials must be increased by 100-fold to add one significant figure to the accuracy of the simulated result. Parallel processing enables more trials to be run; importance sampling techniques can reduce the standard deviation of the sampled distribution.

The larger problem from the perspective of the authors of this report is data specification and management. The primary goal of the P-MCScene effort is to generate polarimetric multi- and hyperspectral images of surface targets, facilities, operations, and materials of interest embedded in complex scenes. Even if simplifying assumptions are made such as (1) molecular and aerosol atmospheric constituents are modeled as horizontally homogeneous, *i.e.*, only dependent upon altitude, (2) 3D clouds, if present, are modeled with uniform optical properties, and/or (3) the ground surface is relatively uniform, the integration of these scene components into most Monte-Carlo simulation models is a major challenge. Furthermore, over-simplifying scene construction can lead to inaccurate scene structure and thereby nullify the usefulness of the simulation for the application at hand.

These problems have been solved for scalar MCScene. As described in the introduction of Section 2, SSI has demonstrated a method for generating spectral band images (consider, for example, a single color Landsat image) without having to sample the fine spectral structure of molecular absorption and emission. In addition, MODTRAN6 has been modified to automatically generate the atmospheric data required by MCScene. Finally, MCScene readily imports digital elevation map (DEM) and atmospherically corrected surface reflectance/emissivity data to characterize the surface. Even voxelized clouds are easily read into MCScene, such as the cumulus and cirrus cloud fields illustrated in Figure 7.

In the following sub-sections, methods for generalizing MCScene scene construction for application to polarimetric synthetic image simulation are described.

2.4.1 MODTRAN Generated Polarimetric Data

MODTRAN6 generates up to three classes of atmospheric data for MCScene: the first characterizes molecular absorption and the second (and optional third) characterize all other sources of atmospheric absorption and scatter. The MCScene database generation by MODTRAN is necessarily performed at a relatively high vertical resolution using 100 m layering from 0.0 to 50.1 km, a total of 501 atmospheric layers. The databases are defined for a given sensor altitude (a multiple of 100 meters), sensor polar angle (a multiple of 10°) and a sensor solar zenith (a multiple of 30°). Tables are generated at 1 nm spectral resolution for solar regime calculations (< ~4 μm); either 1.0 or 0.1 cm^{-1} spectral resolution data is generated for the thermal infrared (> ~4 μm). Spectral convolutions of the databases for specified sensor spectral response functions are performed within MCScene itself.

Each molecular absorption data file stores path transmittances for H_2O, O_3, the remaining ambient uniformly mixed gases, and, when requested, an auxiliary chemical. Standard model molecular profiles are scaled up and down to provide a wide range of column densities. As illustrated in Figure 30, molecular transmittances are stored for two types of paths: (1) direct above and below the horizon paths from the sensor to each altitude level, shown in **blue** and (2) L-shaped solar scatter paths with a direct sensor leg in **blue** and a direct solar leg in **red**. Within MCScene, photon trajectories are weighted by molecular transmittances determined by interpolating into the MODTRAN-generated tables based on molecular column densities and the trajectory minimum altitude. Molecular emissivities are computed as path length derivatives. Since the polarimetric version of MCScene, P-MCScene will model the atmosphere as a medium containing randomly-oriented mirror-imaged particles (ISM), molecular absorption coefficients will be scalars. This implies that the MCScene modeling of molecular attenuation by weighting photon trajectories will be completely applicable to the polarimetric Monte-Carlo simulation. In other words, no changes to the MODTRAN-generated MCScene molecular transmittance databases will be necessary.

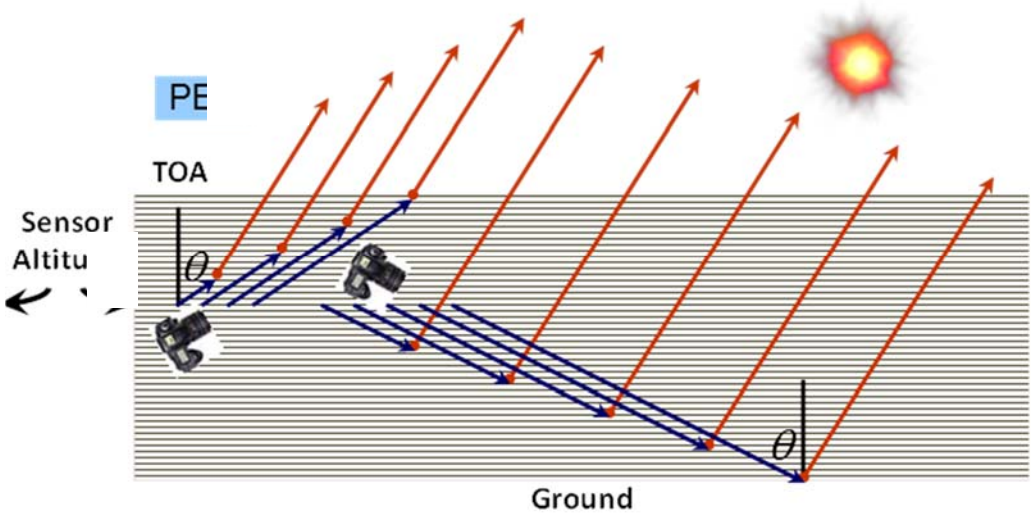

Figure 30. Paths for which MODTRAN-generated MCScene Molecular Transmittance Data is Generated. For a given elevation/depression angle, molecular transmittances are defined for direct sensor to altitude level paths (shown in **blue**), and for L-shaped solar scatter paths with a direct sensor leg in **blue** and a direct solar path leg in **red.**

All spectral band (1 nm, 1.0 cm^{-1}, or 0.1 cm^{-1}) extinction sources other than molecular absorption can be modeled as satisfying Beer's Law (remember that monochromatic radiation attenuates exponentially with column density, but that this Beer's Law relationship only extends to spectral bands if the spectral variability of the extinction varies smoothly across the band; at the specified resolutions, molecular absorption is the only source that exhibits strong spectral structure). The second MODTRAN-generated MCScene database contains Rayleigh scattering coefficients, and particulate (aerosol and cloud) extinction coefficients, scattering coefficients and scattering phase function asymmetry factors for each of the 501 atmospheric layers. The Rayleigh scattering phase function is simple $f_{Ray}(\Theta) = 3\ (1 + \cos^2\Theta\ ) / 4$. For polarization, the Rayleigh Stokes scattering matrix in the $[I_p, I_s, U, V]^T$ representation is diagonal:

$$\mathbf{F}_{Ray} = \frac{3}{2}\begin{pmatrix} \cos^2\Theta & 0 & 0 & 0 \\ 0 & 1 & 0 & 0 \\ 0 & 0 & \cos\Theta & 0 \\ 0 & 0 & 0 & \cos\Theta \end{pmatrix} \qquad \textbf{(23)}$$

If the scattering of aerosols and clouds is approximated with a Henyey-Greenstein scattering phase function, then the asymmetry factor defines its form. Since the particulate extinction and scattering coefficient will remain scalars in P-MCScene, just like the molecular absorption coefficients, no changes need to be made to the second MODTRAN-generated MCScene database.

The third MODTRAN-generated MCScene database, optional for the scalar model, defines angularly tabulated particulate scattering phase functions when the Henyey-Greenstein form is not used. Again, the data is generated for all 501 MODTRAN layers. To date, this file has only been used to define scattering phase functions for Mie (spherical) particles, but it could certainly be used to define scattering phase functions for any collection of ISM particles. For P-MCScene, Stokes scattering matrices are required. The MODTRAN6 option to angularly tabulate scattering phase functions for MCScene will be upgraded in MODTRAN7 to angularly tabulate Stokes scattering matrices for P-MCScene. As discussed in Section 2.3, MODTRAN7 will already be processing Stokes scattering matrix data, so generating the expanded spectral tables will be straightforward.

Within P-MCScene, a Stokes scattering matrix for a given spectral channel and altitude is needed for two operations each time a scattering event occurs. First, it is used to compute the Stokes vector solar scattering contribution. The scattering angle to the sun is easily determined and the Stokes scattering matrix quickly interpolated to that value. After the intensity terms have been summed, the scattering phase function, equal to the $F_{11}(\Theta)$ element of the Stokes scattering matrix, is sampled (integrated) to determine a new direction for the photon trajectory. Integration of scattering phase functions is too slow to be practical within P-MCScene's DSMC approach. This was as much of an issue for scalar MCScene when Mie scatterers were modeled as it will be for P-MCScene. The scalar MCScene solution will be applied to P-MCScene. In this approach, the full set of phase functions [or $F_{11}(\Theta)$ elements] for a given aerosol or cloud are expanded in terms of a small, fixed set of endmembers with positive abundances. These endmembers are preprocessed to facilitate rapid sampling. Whenever an actual scattering matrix needs to be sampled, a first random number is used to select an endmember based on the $F_{11}(\Theta)$ abundances. A second random number is mapped into a scattering angle for the selected endmember.

2.4.2 Surface Characterization

An automatable procedure is required for setting up a MCScene simulation that realistically represents a hyperspectral scene, with appropriate polarization and BRDF properties for the surface materials and terrain. The starting point will be measured hyperspectral image (HSI) data. To simulate a VNIR-SWIR HSI scene, P-MCScene will start by selecting VNIR-SWIR HSI data. To simulate a LWIR HSI scene, it would be best to start from LWIR data. However, as described below and in an SSI publication [Richtsmeier *et al.*, 2004], it is possible to use VNIR HSI to define surface materials for an LWIR or full-spectrum (VNIR-SWIR + LWIR) MCScene simulation.

For VNIR-SWIR HSI data, the first step will be to process the image to surface reflectance using FLAASH®, SSI's MODTRAN-based atmospheric correction algorithm. Either the IDL-language version of FLAASH contained in the well-known ENVI software package or the standalone C++ language FLAASH-C code [Perkins *et al.*, 2012] can be chosen. For LWIR HSI data, the processing would use FLAASH-IR [Adler-Golden *et al.*, 2012], the SSI MODTRAN-based algorithm for atmospheric correction and temperature-emissivity separation (TES). FLAASH-IR outputs both surface reflectance (or emissivity) spectra and a surface temperature map.

The next step is to assign surface materials to each pixel in the derived reflectance image. An efficient way to do this is with an endmember-finding and unmixing code. Two suitable methods are described in a recent SSI paper on mineral classification [Sundberg *et al.*, 2015]. The first is to use SMACC, the SSI fast, automated endmember code that finds in-scene endmember spectra and calculates their abundances with positivity and optional sum-to-unity constraints [Gruninger *et al.*, 2004]. The second is to use a sparse positivity-constrained least-squares algorithm, which limits the potential number of endmembers in each pixel to a small number such as two or three. The positivity and sparseness constraints ensure physically reasonable abundances. The endmembers are then matched to spectrally corresponding materials in the NEF database or to mixtures thereof. MCScene will then perform the scene simulation using the material BRDF spectra and their abundances, and, for the LWIR, the FLAASH-IR-derived surface temperatures.

For best accuracy with specular materials, and for consistency of the retrieval and forward simulation methods, the assignment of VNIR-SWIR endmembers to the NEF database materials should be based on spectrally interpolated NEF BRDFs calculated for the solar and observer angles in the original image. Using the NEF directional hemispherical reflectance (DHR) spectra to interpolate the BRDFs should provide better matches to the pure endmember amplitudes than simply using the NEF DHR spectra directly. For the LWIR, the NEF DHR spectrum is appropriate, as it is responsible for the surface emission component, which dominates the surface-leaving radiance.

Refinements and extensions of the above procedure can be developed as needed for particular applications. For example, an LWIR scene can be simulated starting from a VNIR-SWIR-based material map supplemented by a surface temperature map derived from empirical correlations [Richtsmeier *et al.*, 2004], heat transfer calculations, or a broadband LWIR imager. Combinations of VNIR-SWIR and LWIR band imagery are available for a number of sensors, including Landsat-8.

2.4.3 Polarimetric Radiative Transfer Algorithm

The P-MCScene method for computing high fidelity polarimetric hyperspectral images will be very similar to the approach scalar MCScene uses to compute high fidelity radiometric HSI. A scene is constructed as delineated above. An outer loop over sensor channels is performed in which MODTRAN atmospheric data is convolved with the current sensor channel spectral response function, unless that convolution has already been performed. In the latter case, the previously convolved and saved data is read in. Next, a loop over sensor pixels is initiated. If parallel processing is activated, pixels are partitioned among available processors.

For each spectral channel and sensor pixel, a reverse propagation DSMC calculation is performed. A flowchart of the processing, as illustrated in Figure 8, follows.

1. *Initialize trajectory*
2. Select a trajectory segment optical depth, $\tau = -\ln(\beta)$, where β is a random number on [0, 1] (In scalar and vector MCScene, this optical depth excludes molecular absorption).
3. **Stop** if photon exits the top-of-atmosphere
4. Traverse segment until a surface is hit or the optical depth τ is expended within the atmosphere
5. *Compute and sum solar and thermal Stokes component intensities*
6. Sample the atmospheric scattering phase function or the surface (*Maxwell-Beard*) scalar BRDF to determine the direction of the next photon trajectory segment
7. *Update trajectory weight and phase matrix product*
8. **Stop** if a user specified exit criterion is met
9. Return to Step 2

Here, italics have been used to denote steps or items which must be updated in order to model polarization.

In Step 1, initialization includes not only setting the trajectory weight to unity and its location and direction cosines to the sensor pixel values, but also setting an order of scattering/reflection 4 × 4 phase matrix, $\mathbf{Z}_0$, to the identity matrix. After a combination of N scattering or reflection events, the order N Stokes vector has the form

$$\begin{pmatrix} I \\ Q \\ U \\ V \end{pmatrix}_{sensor} = \mathbf{Z}_1\mathbf{Z}_2\cdots\mathbf{Z}_{N-1}\mathbf{Z}_N \begin{pmatrix} I \\ Q \\ U \\ V \end{pmatrix}_{source} = \mathbf{Z}_0\mathbf{Z}_1\mathbf{Z}_2\cdots\mathbf{Z}_{N-1}\mathbf{Z}_N \begin{pmatrix} I \\ Q \\ U \\ V \end{pmatrix}_{source} \quad \textbf{(24)}$$

With reverse MC, the $\mathbf{Z}_N$ phase matrix is computed last even though it is the first scattering or reflection event to occur chronologically, the $\mathbf{Z}_{N\text{-}1}$ phase matrix is computed second to last, and so on. Since matrix multiplication is not commutative, one cannot reverse propagate the source Stokes vector. Instead, one must store the product of phase matrices, $\mathbf{Z}_0\mathbf{Z}_1\mathbf{Z}_2\cdots$, as they are encountered.

For the initial optical depth, termination at Step 3 can only happen for paths that face the TOA. In that case, the initial optical depth is forced to be less than the escape optical depth and the photon weight is adjusted accordingly.

In Step 5, the product $\mathbf{Z}_0\mathbf{Z}_1\cdots\mathbf{Z}_{N\text{-}1}$ is post-multiplied by the thermal emission source Stokes vector to compute the Stokes thermal emission contribution. Similarly, $\mathbf{Z}_0\mathbf{Z}_1\cdots\mathbf{Z}_{N\text{-}1}$ is post-multiplied by the solar/lunar direction phase matrix and the solar/lunar source Stokes vector to compute the Stokes solar/lunar contribution. Each of these terms is weighted by the trajectory weight and the spectral channel molecular transmittance.

In Step 6, the direction of the next photon trajectory segment is computed. For atmospheric scatter, the process developed for scalar MCScene is completely applicable to P-MCScene. For surfaces, however, modified Maxwell-Beard BRDFs, described above in Section 2.1.1.2, are being introduced. Generally, the reflected photon direction would be computed by sampling the BRDF distribution for the fixed incident angle normalized by the directional hemispherical reflectance (DHR) in the direction of that incident angle. This would require integrating the MB scalar BRDF, which is difficult and slow. An alternative approach can be used for MB surfaces. One can sample the portion of the Gaussian or Cauchy microfacet angular probability distribution function, $p(\mu_N)$, that is visible to the incident photon. Here, $p(\mu_N)$ is assumed to be normalized such that $2\pi\int_{[0,1]} p(\mu_N)\,\mu_N\,d\mu_N = 1$. Given incident direction *outward* unit vector $\hat{\mathbf{s}}_i$ and microfacet unit normal $\hat{\mathbf{s}}_N$, the normalization integral over visible facets, η_{vis}, for the incoming Stokes vector equals

$$\begin{aligned}\eta_{vis} &= \int_0^1 p(\mu_N) \int_{\min(\Delta\phi)}^{\max(\Delta\phi)} \hat{\mathbf{s}}_i \bullet \hat{\mathbf{s}}_N \; d(\Delta\phi)\, d\mu_N \\ &= \int_0^1 p(\mu_N) \int_{\min(\Delta\phi)}^{\max(\Delta\phi)} \left[\mu_i\,\mu_N + \sqrt{\left(1-\mu_i^2\right)\left(1-\mu_N^2\right)}\,\cos\Delta\phi \right] d(\Delta\phi)\, d\mu_N\end{aligned} \tag{25}$$

Here, $\min(\Delta\phi)$ and $\max(\Delta\phi)$ are $-\pi$ and π if the facet with cosine normal μ_N is visible with incident direction $-\hat{\mathbf{s}}_i$ at all azimuth angles. When $(1-\mu_i^2)\,(1-\mu_N^2)$ exceeds $\mu_i^2\,\mu_N^2$, then the relative azimuth range is restricted, i.e. the term is square bracket must not be negative. Thus

$$\begin{aligned}\eta_{vis} &= \int_{\sqrt{1-\mu_i^2}}^1 p(\mu_N) \int_{-\pi}^{\pi} \left[\mu_i\,\mu_N + \sqrt{\left(1-\mu_i^2\right)\left(1-\mu_N^2\right)}\,\cos\Delta\phi \right] d(\Delta\phi)\, d\mu_N \\ &+ \int_0^{\sqrt{1-\mu_i^2}} p(\mu_N) \int_{-\arccos\left(-\mu_i\mu_N \Big/ \sqrt{\left(1-\mu_i^2\right)\left(1-\mu_N^2\right)}\right)}^{\arccos\left(-\mu_i\mu_N \Big/ \sqrt{\left(1-\mu_i^2\right)\left(1-\mu_N^2\right)}\right)} \left[\mu_i\,\mu_N + \sqrt{\left(1-\mu_i^2\right)\left(1-\mu_N^2\right)}\,\cos\Delta\phi \right] d(\Delta\phi)\, d\mu_N \\ &= \mu_i + 2\int_0^{\sqrt{1-\mu_i^2}} \left[\sqrt{1-\mu_i^2-\mu_N^2} - \mu_i\,\mu_N \arctan\left(\frac{\sqrt{1-\mu_i^2-\mu_N^2}}{\mu_i\,\mu_N} \right) \right] p(\mu_N)\, d\mu_N\end{aligned} \tag{26}$$

Not unsurprisingly, all facets are visible to the incident photon only when μ_i is 1. The η_{vis} integrals can be tabulated prior to the initiation of the MC processing. Given a random number β between 0 and 1, the micro-facet surface normal, μ_N^*, is computed from the equation

$$\beta = \begin{cases} \dfrac{2\pi\,\mu_i}{\eta_{vis}} \displaystyle\int_{\mu_N^*}^1 \mu_N\, p(\mu_N)\, d\mu_N \quad \textit{if} \quad \beta \le \dfrac{2\pi\,\mu_i}{\eta_{vis}} \displaystyle\int_{\sqrt{1-\mu_i^2}}^1 \mu_N\, p(\mu_N)\, d\mu_N \quad ; \quad \textit{otherwise} \\ \dfrac{2\pi\,\mu_i}{\eta_{vis}} \displaystyle\int_{\mu_N^*}^1 \mu_N\, p(\mu_N)\, d\mu_N + \dfrac{2}{\eta_{vis}} \displaystyle\int_{\mu_N^*}^{\sqrt{1-\mu_i^2}} \left[\sqrt{1-\mu_i^2-\mu_N^2} - \mu_i\,\mu_N \arctan\left(\dfrac{\sqrt{1-\mu_i^2-\mu_N^2}}{\mu_i\,\mu_N} \right) \right] p(\mu_N)\, d\mu_N \end{cases} \tag{27}$$

Given a second random number β', the relative azimuth $\Delta\phi^*$ is determined from

$$\beta' = \begin{cases} \dfrac{\Delta\phi^* + \pi}{2\pi} + \sqrt{\left(1-\mu_i^2\right)\left(1-\mu_N^2\right)}\,\dfrac{\sin\Delta\phi^*}{2\pi\,\mu_i\,\mu_N} & \text{if} \quad \mu_N^* > \sqrt{1-\mu_i^2} \quad ; \quad \text{otherwise} \\ \dfrac{1}{2} + \dfrac{\mu_i\,\mu_N\Delta\phi^* + \sqrt{\left(1-\mu_i^2\right)\left(1-\mu_N^2\right)}\,\sin\Delta\phi^*}{2\pi + 2\sqrt{1-\mu_i^2-\mu_N^2} - 2\mu_i\,\mu_N \arctan\left(\dfrac{\sqrt{1-\mu_i^2-\mu_N^2}}{\mu_i\,\mu_N}\right)} \end{cases} \qquad \textbf{(28)}$$

The values (μ_N^*, $\Delta\phi^*$) define the orientation of the microfacet that the incident photon randomly hit. Another random number is selected to determine if the photon is reflected or transmitted. If it is transmitted, it is modeled as volumetrically scattered. Some of the reflected photons will be directed "downward" into the macrofacet. These photons can be modeled as undergoing an additional reflection.. For reflected photons directed back into the atmosphere, a trajectory weight must be applied to account for possible shadowing or obscuration.

One final sampling issue is that MCScene invokes importance sampling to improve MC convergence by preferentially selecting photons directed towards the sun when modeling solar intensities. MCScene does this by sampling from a distribution that favors the solar direction 50% of the time. For the surface reflection problem, the solar direction distribution will be the defined as the MB surface whose macrofacet is oriented specularly to the sun.

In Step 7, the product of phase matrices, $\mathbf{Z}_0\mathbf{Z}_1\cdots\mathbf{Z}_{N-1}$, is post-multiplied by $\mathbf{Z}_N$. It is noted here that these phase matrices, defined by $\mathbf{Z}(\Omega, \Omega') = \mathbf{R}(\pi - \beta)\,\mathbf{F}(\Theta)\,\mathbf{R}(\alpha)$ at the end of the introduction to Section 2.2, are normalized such that the F_{11} element of $\mathbf{F}(\Theta)$ equals 1. Here, $\mathbf{F}(\Theta)$ is the Stokes scattering matrix for atmospheric scattering events, or the pBRDF for surface reflectance events. Since the new directions are computed by directly sampling either the atmospheric scattering phase function or the surface scalar BRDF, the trajectory is not weighted by their values. In scalar MCScene, this is equivalent to a multiplication by 1. In P-MCScene the normalized phase matrices must be computed to determine the final polarization state. The effect of the rotations, $\mathbf{R}(\pi - \beta)$ and $\mathbf{R}(\alpha)$, is described in Appendix A.

2.5 Validation Field Measurement Plan

A modest measurement program is being proposed in collaboration with the Remote Sensing and Exploitation (RSE) group at Sandia National Laboratories (SNL) to validate both MODTRAN7 and P-MCScene. There are three primary goals. The first objective is to evaluate the accuracy of simulations when the environment and the surface target pBRDF are well characterized. These measurements would be used to quantify residuals and compare them to the standard errors due to uncertainties in measurement conditions. The current measurements underway by SNL may be perfectly suitable for these validations. The second objective is to determine "how much error is introduced by the modeling protocol for spectrally interpolating between laser wavelength (monochromatic) surface pBRDF data?" The goal here will be to consider a material from the NEF Data System, and compare simulated intensities computed with spectrally interpolated pBRDF data to direct measurements. In addition, specific measurements would be made to directly retrieve polarimetric BRDF information. In this way, the spectrally interpolated pBRDF parameterization itself could be directly compared to the measured pBRDF parameters. The third and final objective is measurement of spectral indices of refraction. If the spectral dependence of the index of refraction can be measured for a number of materials of interest, then this information can be used to improve the spectral interpolation of the pBRDF's.

2.5.1 SNL Measurement Program

Details of the current measurement program in the RSE group at SNL are provided in Section 2.1.3.3 and are not repeated here. However, it is important to emphasize that both the current SNL measurement program and the proposed DOE SBIR Phase II polarimetric modeling efforts will benefit from our collaboration.

2.5.2 Recommendations for pBRDF Retrievals

As noted in Section 2.1.3.3, SNL has suggested a willingness to conduct tailored measurements of Maxwell-Beard pBRDF parameters. These spectral Vis/SWIR linear polarization measurements could be conducted at SNL either in the laboratory or outside, under ambient conditions. Three measurement configurations are proposed in the following sub-sections. Optimally, the surface materials of interest could be placed on a two-gimbal system to provide yaw and pitch variability, as illustrated in Figure 31. A single gimbal device varying the pitch would suffice, but would require manual positioning of the target in the principal scattering plane. Without a gimbal, primitive techniques could be used to orient the target materials and measure the incline.

Figure 31. Illustration of a Two-gimbal Device Providing Yaw and Pitch Variability**.**

2.5.2.1 Surface Roughness Measurements

Surface roughness is equated to the angular variability of surface normals. If a sensor is co-aligned with a collimated source, such as the sun, then there is no shadowing. If a target is rotated in the principal plane, as illustrated in Figure 32, then the strength of the reflected signal should be proportional to the fraction of specularly oriented micro-facets. This configuration measures the Maxwell-Beard microfacet angular probability distribution function, $p(\mu_N)$, described in Section 2.1.1.2. Similar measurements can be made for a horizontal target by repositioning the sensor as the sun traverses the sky throughout the day (or as the collimated laboratory source is moved). With the latter procedure, one must model or measure any variability of the irradiance.

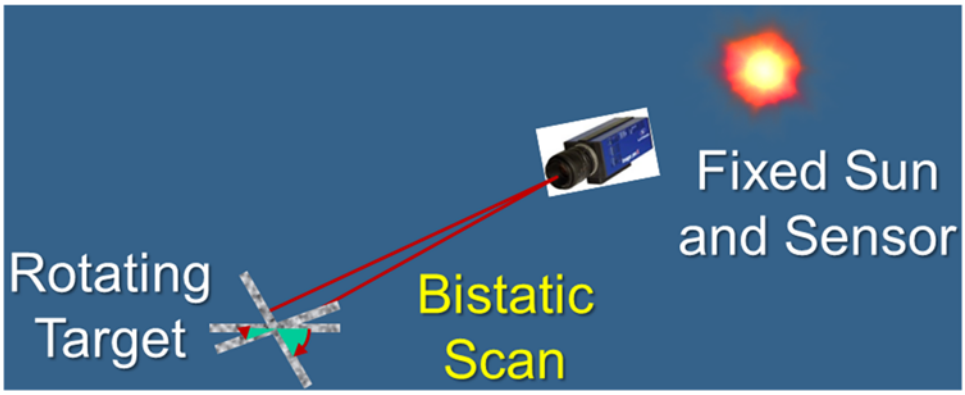

Figure 32. Illustration of Bistatic Scan Measurement Configuration**.**

2.5.2.2 Specular Scan Measurements

Spectral index of refraction can be determined from Brewster angle measurements. The Brewster angle is the angle at which the *p* (parallel) linear polarization component is minimized. This can be determined by performing specular scans of the spectral polarization. An idealized arrangement is illustrated in Figure 33. In the figure, the orientation of the target material in the principal plane is varied in coordination with the movement of the spectral polarimetric sensor, so that specular reflectances can be mapped. This is referred to as an idealized arrangement because it would be difficult to perform these measurements rapidly enough to consider the sun fixed. Optimally, however, these measurements could be performed inside the laboratory in the RSE group at SNL. With a strong collimated source, the controlled conditions of the laboratory environment would be ideal.

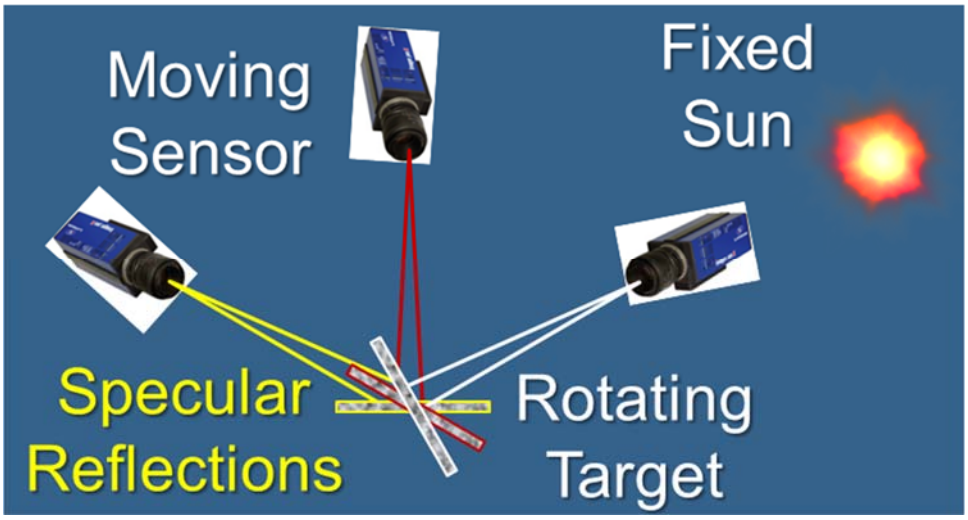

Figure 33. Illustration of Specular Reflection Measurement Configuration**.**

2.5.2.3 Fixed Incident Angle Principal Plane Measurements

If the surface normal distribution and the index of refraction of a target material are both well characterized, one can predict the principal plane reflectance for a fixed incident angle if masking effects (shadowing and obscuration) are negligible. Often, masking is not negligible, so measuring the principal plane reflectance can quantify the extent of shadowing and obscuration. In Figure 34, these measurements are depicted with a horizontal target material and a scanning sensor arrangement. As before, these measurements could be made either in a laboratory or in the ambient environment.

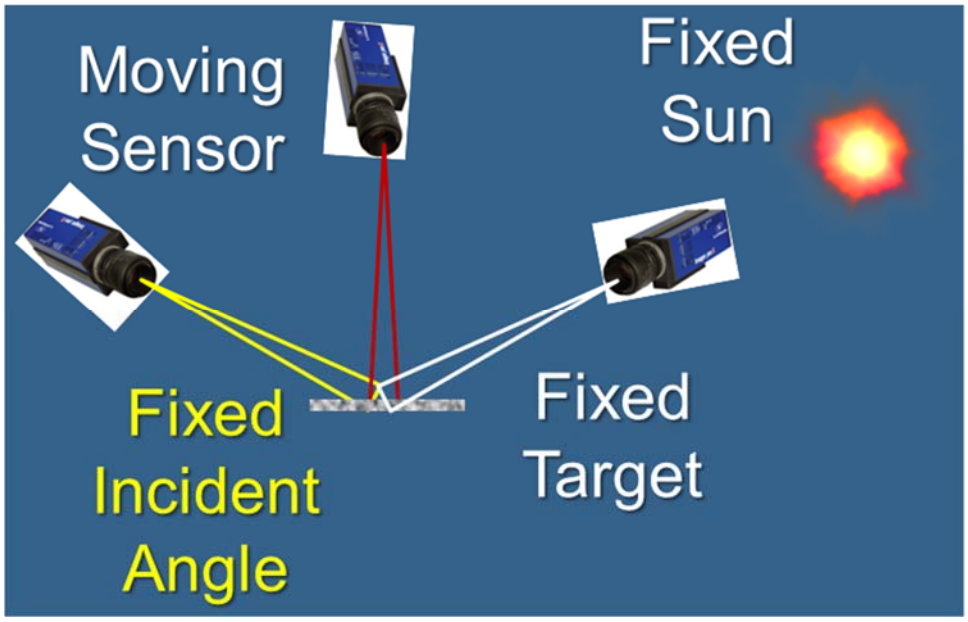

Figure 34. Illustration of the Fixed Incident Angle Principle Plane Measurement Configuration**.**

3. SUMMARY AND CONCLUSIONS

The DOE Phase I entitled "Development and Validation of a Polarimetric-MCScene 3D Atmospheric Radiation Model" was an ambitious and successful effort. Phase I was designed to set the groundwork for vectorizing MODTRAN6 and MCScene, demonstrating a clear pathway to the ultimate Phase II goal of fully validated polarimetric models. This has been accomplished. In particular, methods for modeling ground targets, facilities, operations, and materials of interest were detailed. The specific Phase I tasks were to

1. assess the accuracy and applicability of current available polarimetric databases;
2. formulate the approach for upgrading MODTRAN6 to compute polarization;
3. integrate polarimetric-MODTRAN4 (MODTRAN4P) components into MODTRAN7;
4. develop a design and implementation plan for P-MCScene; and
5. plan a validation field measurement program.

Each of these tasks was successfully completed. State-of-the-art atmospheric scatter and surface reflectance data sources were downloaded. Tools for generating custom aerosols were also made available. Field measurement data sources to be used for validation were identified, and data requests initiated. An approach for upgrading MODTRAN6 to MODTRAN7 was formulated that includes (1) defining data ingestion, (2) incorporating Stokes scattering matrices and polarimetric reflectance (pBRDF) data, and (3) integration of the VDISORT3 multiple scattering model tailored for MODTRAN7. MODTRAN4P aerosol scattering data has already been integrated into the preliminary MODTRAN7 model, which computes single scatter solar and lunar Stokes vectors. Test calculations with MODTRAN7 demonstrated that MODTRAN6 total intensity values for lunar single scatter were in error by over 4% since polarimetric effects are ignored. A design and implementation plan for P-MCScene was developed. A major component of this plan is an automated methodology for scene construction including defined Stokes scattering matrices for atmospheric particulates and Maxwell-Beard pBRDFs for surfaces. A validation field measurement program was planned in collaboration with the Remote Sensing and Exploitation group at SNL. The focus of the validation efforts are quantifying the accuracy of MODTRAN7 and P-MCScene simulations, and evaluating and upgrading the surface pBRDF parameterizations.

Questions that were to be answered by the Phase I effort were:

a. Which MODTRAN4P strategies, routines and data are applicable to P-MODTRAN6?
b. What changes to MCScene and its MODTRAN-generated databases are needed to accommodate polarization?
c. What is the availability of polarimetric aerosol and surface data?

Each of these questions has been thoroughly answered. MODTRAN4P aerosol scattering data and Stokes matrix input data checking have already been imported into MODTRAN7. MODTRAN7 will be using a very different vectorization strategy from that used by MODTRAN4P, so most of the MODTRAN4P software is of little benefit. Two of the three MODTRAN-generated MCScene data files are already P-MCScene compatible. The third file contains angular scattering phase function data, tabulated as a function of spectral frequency and altitude layer. This file must be updated to contain the 6 ISM Stokes matrix elements instead of the single $F_{11}(\Theta)$ element. A modest number of scene construction and radiative transfer changes need to be made to MCScene for polarimetric HSI/MSI scene simulation. These have all been delineated. Finally, state-of-the-art polarimetric surface and aerosol data has been downloaded for use in MODTRAN7 and P-MCScene.

4. ACKNOWLEDGEMENTS

Many individuals provided their expertise and assistance in support of this effort. First and foremost, we thank Drs. Victoria Franques and Steven Sharpe for providing guidance on the issues of greatest concern to the DOE Office of Defense Nuclear Nonproliferation Research and Development (NA-22). Drs. Michael I. Mishchenko, Yoshihide Takano, Kuo-Nan Liou, and Knut Stamnes all helped clarify subtleties regarding polarimetric radiative transfer. In particular, we thank Dr. Knut Stamnes for providing guidance on the VDISORT3 model, and Dr. Jeannette van den Bosch for providing an advance copy of the software. Drs. Ping Wang and Zhaokai Meng are acknowledged for providing access to their cirrus cloud and mineral dust data libraries. Finally, we thank Drs. Joao Romano, Tom Caudill, Julia Craven, and Jeffrey Mercier for providing information on their polarimetric measurement programs, which will provide critical validation data for the MODTRAN7 and P-MCScene simulation models.

REFERENCES

Adler-Golden, S., S. Richtsmeier, R. Panfili, X. Jin, J.W. Duff, J.G. Shanks, and A. Dudkin, "Next Generation Terrain and Cloud Background Models for System Studies," Spectral Sciences, Inc., Report No. SSI-TR-635, Phase II Final Report, prepared for United States Army Space and Missile Defense Command under Contract No. W9113M-10-C-0081 (2012).

Baum, B.A., P. Yang, A.J. Heymsfield, S. Platnick, M.D. King, and S.T. Bedka, "Bulk scattering models for the remote sensing of ice clouds. Part II: Narrowband models," J. Appl. Meteor., **44**, 1896–1911 (2005).

Berk, A., J. van den Bosch, F. Hawes, T. Perkins, P.F. Conforti, G.P. Anderson, R.G. Kennett, and P.K. Acharya, "MODTRAN® 6.0.0.2 User's Manual," Spectral Sciences Inc., Report No. SSI-TR-685, software deliverable prepared for United States Air Force Research Laboratory Space Vehicles Directorate under Contract No. FA9453-12-C0262 (2016).

Chandrasekhar, S., "Radiative Transfer," (Oxford, Oxford University Press, 1950); Dover reprint edition (New York, Dover Publications, 1960).

Collins-Sussman, B., B.W. Fitzpatrick, and C.M. Pilato, "Version Control with Subversion for Subversion 1.7 (Compiled from r5129)," http://svnbook.red-bean.com/en/1.7/svn-book.pdf (2016).

Fenn, R. W., S.A. Clough, W.O. Gallery, R.E. Good, F.X. Kneizys, J.D. Mill Lt. Col. USAF, L.S. Rothman, E.P. Shettle, and F.E. Volz, "Optical and Infrared Properties of the Atmosphere," Handbook of Geophysics and the Space Environment, Adolph S. Jursa, Ed., 4th edition, ADA 167000, chapter 18 (Air Force Geophysics Laboratory, 1985).

Fetrow, M.P., D. Wellems, S.H. Sposato, K.P. Bishop, T.R. Caudill, M.L. Davis, and E.R. Simrell, "Results of a new polarization simulation," *Proc. SPIE* 4481, Polarization Analysis and Measurement IV, 149 (January 11, 2002), doi:10.1117/12.452902.

Garcia, R.D.M., and C.E. Siewert, "The F_N Method for Radiative Transfer Models that Include Polarization Effects," J. Quant. Spectrosc. Radiat. Transfer, **41**(2), 117-145 (1989).

Gruninger, J., A.J. Ratkowski, and M. L. Hoke, "The sequential maximum angle convex cone (SMACC) endmember model," *Proc. SPIE* 5425, Algorithms and Technologies for Multispectral, Hyperspectral, and Ultraspectral Imagery X, Sylvia S. Shen and Paul E. Lewis, Chairs/Editors, 1-14 (August 12, 2004), doi: 10.1117/12.543794.

Henyey, L.C., and J. L. Greenstein, "Diffuse radiation in the galaxy," Astrophys. J. **93**, 70 (1941).

Kokhanovsky, A.A., V.P. Budak, C. Cornet, M. Duan, C. Emde, I.L. Katsev, D.A. Klyukov, S.V. Korkin, L. C-Labonnote, B. Mayer, Q. Min, T. Nakajima, Y. Ota, A.S. Prikhach, V.V. Rozanov, T. Yokota, and E.P. Zege, "Benchmark results in vector atmospheric radiative transfer," J. Quant. Spectrosc. Radiat. Transfer, **111**, 1931-1946 (2010).

Liou, K.N., "An Introduction to Atmospheric Radiation," 2nd ed. (Academic Press, California, 2002).

Macke, A., personal communication to A. Berk (2001).

Maxwell, J.R., J. Beard, S. Weiner, D. Ladd, and S. Ladd, "Bidirectional reflectance model validation and utilization," Tech. Rpt. AFAL-TR-73-303, Environmental Research Institute of Michigan (ERIM), (October 1973).

Meng, Z., P. Yang, G.W. Kattawar, L. Bi, K.N. Liou, and I. Laszlo, "Single-scattering properties of tri-axial ellipsoidal mineral dust aerosols: A database for application to radiative transfer calculations," J. Aer. Sci., **41**, 501–512 (2010).

Mishchenko, M.I., "Transfer of polarized infrared radiation in optically anisotropic media: application to horizontally oriented ice crystals: comment," J. Opt. Soc. Am. A, **11**, pp. 1376-1377 (1994), doi: 10.1364/JOSAA.11.001376.

Mishchenko, M.I., and L.D. Travis, "Capabilities and limitations of a current FORTRAN implementation of the T-matrix method for randomly oriented rotationally symmetric scatterers," J. Quant. Spectrosc. Radiat. Transfer **60**, 309-324 (1998).

Mishchenko, M.I., L.D. Travis, and A.A. Lacis, *Scattering, Absorption, and Emission of Light by Small Particles*, (Cambridge University Press, Cambridge, 2002). Third electronic release (2006), available at http://www.giss.nasa.gov/staff/mmishchenko/books.html .

Mishchenko, M.I., spher.f (Aug. 6, 2005), http://www.giss.nasa.gov/staff/mmishchenko/ftpcode/spher.f .

Mishchenko, M.L., L.D. Travis, and A.A. Lacis, *Multiple Scattering of Light by Particles*, (Cambridge University Press, Cambridge, 2006).

Pellicori, S.F., "Polarizing Properties of Pulverized Materials with Special Reference to the Lunar Surface," Applied Optics **10**, 270-285 (1971).

Perkins, T., S.M. Adler-Golden, M.W. Matthew, A. Berk, L.S. Bernstein, J. Lee, and M. Fox, "Speed and accuracy improvements in FLAASH atmospheric correction of hyperspectral imagery," Opt. Eng. **51**(11), 111707, doi:10.1117/1.OE.51.11.111707 (2012).

Plass, G.N., "Models for Spectral Band Absorption," J. Opt. Soc. Am. **48**, 690-703 (1958).

Plass, G.N., "Useful Representations for Measurements of Spectral Band Absorption," J. Opt. Soc. Am. **50**, 868-875 (1960).

Priest, R.G., and S.R. Meier. "Polarimetric microfacet scattering theory with applications to absorptive and reflective surfaces," Optical Engineering, **41**(5):988–993 (2002).

Richtsmeier, S., A. Berk, S.M. Adler-Golden, and L.S. Bernstein, "A 3D Radiative-Transfer Hyperspectral Image Simulator for Algorithm Validation," Proceedings of ISSSR 2001, Quebec City, Canada (June 2001).

Richtsmeier, S., R.L. Sundberg, A. Berk, S. Adler-Golden, and R. Haren, "Full Spectrum Scene Simulation," *Proc SPIE* 5425, Algorithms and Technologies for Multispectral, Hyperspectral, and Ultraspectral Imagery X, 530-537 (August 12, 2004).

Robertson, D.C., F.T. Hawes, A. Berk, F. Bien, J.A. Conant, and M. Hoke, "Forward and Inverse Radiation Transport Modeling for End to End Analysis of Hyperspectral Imagery, Final Report: Development of Polarization Option to MODTRAN4," Contract No. F19628-02-C-0078 (2007).

Romano, J.M., M. Felton, D. Chenault, and B. Sohr, "Polarimetric imagery collection experiment," *Proc. SPIE* 7696, Automatic Target Recognition XX; Acquisition, Tracking, Pointing, and Laser Systems Technologies XXIV; and Optical Pattern Recognition XXI, 769611 (2010), doi: 10.1117/12.849911.

Rosario, D., J. Romano, and C. Borel-Donohue, "Spectral and Polarimetric Imagery Collection Experiment (SPICE) Longwave Infrared Spectral Dataset," Army Research Laboratory, ARL-TR-7051 (2014).

Rothman, L.S., I.E. Gordon, A. Barbe, D. Chris Benner, P.F. Bernath, M. Birk, V. Boudon, L.R. Brown, A. Campargue, J.-P. Champion, K. Chance, L.H. Coudert, V. Dana, V.M. Devi, S. Fally, J.-M. Flaud, R.R. Gamache, A. Goldman, D. Jacquemart, I. Kleiner, N. Lacome, W.J. Lafferty, J.-Y. Mandin, S.T. Massie, S.N. Mikhailenko, C.E. Miller, N. Moazzen-Ahmadi, O.V. Naumenko, A.V. Nikitin, J. Orphal, V.I. Perevalov, A. Perrin, A. Predoi-Cross, C.P. Rinsland, M. Rotger, M. Simeckova, M.A.H. Smith, K. Sung, S.A. Tashkun, J. Tennyson, R.A. Toth, A.C. Vandaele, and J. Vander Auwera, "The HITRAN 2008 molecular spectroscopic database," J. Quant. Spectrsosc. Radiat. Transfer **110**, 533-572 (2009).

Rothman, L.S., I.E. Gordon, Y. Babikov, A. Barbe, D. Chris Benner, P.F. Bernath, M. Birk, L. Bizzochi, V. Boudon, L.R. Brown, A. Campargue, K. Chance, E.A. Cohen, L.H. Coudert, V.M. Devi, B.J. Drouin, A. Fayt, J.-M. Flaud, R.R. Gamache, J.J. Harrison, J.-M. Hartmann, C. Hill, J.T. Hodges, D. Jacquemart, A. Jolly, J. Lamouroux, R.J. Le Roy, G. Li, D.A. Long, O.M. Lyulin, C.J. Mackie, S.T. Massie, S.N. Mikhailenko, H.S.P. Mueller, O.V. Naumenko, A.V. Nikitin, J. Orphal, V.I. Perevalov, A.

Perrin, E.R. Polovtseva, C. Richard, M.A.H. Smith, E. Starikova, K. Sung, S. Tashkun, J. Tennyson, G. C. Toon, Vl. G. Tyuterev, and G. Wagner, "The HITRAN2012 molecular spectroscopic database," J. Quant. Spectrsosc. Radiat. Transfer **130**, 4-50 (2013).

Schulz F.M., K. Stamnes, and F. Weng, "VDISORT: An Improved and Generalized Discrete Ordinate Method for Polarized (Vectro) Radiative Transfer," J. Quant. Spectrosc. Rad. Transfer, **61**, 105-122, (1999), doi:10.1016/S0022-4073(97)00215-X.

Sharpe, SW, TJ Johnson, RL Sams, PM Chu, GC Rhoderick and PA Johnson, "Gas-Phase Databases for Quantitative Infrared Spectroscopy," Appl. Spectrosc., 58, 1452-1461 (2004).

Shell, J.R., "Polarimetric Remote Sensing in the Visible to Near Infrared," Doctoral Dissertation, Rochester Institute of Technology, 2005.

Shettle, E.P., and R.W. Fenn, "Models of the Aerosols of the Lower Atmosphere and the Effects of Humidity Variations on Their Optical Properties," AFRL TR-79-0214, ADA 085951 (1979).

Siewert, C.E., "A discrete-ordinates solution for radiative-transfer models that include polarization effects," J. Quant. Spectrosc. Radiat. Transfer **64**, 227-254 (2000).

Stamnes, K., S.-C. Tsay, W.J. Wiscombe, and K. Jayaweera, "Numerically stable algorithm for discrete-ordinate-method radiative transfer in multiple scattering and emitting layered media,", Applied Optics **27**, 2502-2509 (1988).

Stamnes, K., and J.J. Stamnes, "Radiative Transfer in Coupled Environmental Systems: An Introduction to Forward and Inverse Modeling," (Wiley-VCH, Weinheim, Germany, 2015).

Stamnes, K., S.-C. Tsay, W.J. Wiscombe, and I. Laszlo, "DISORT, a General-Purpose Fortran Program for Discrete-Ordinate-Method Radiative Transfer in Scattering and Emitting Layered Media: Documentation of Methodology," report (2000), available from ftp://climate.gsfc.nasa.gov/pub/wiscombe/Multiple_Scatt/ .

Sundberg, R., S. Adler-Golden, and P. Conforti, "Long-wavelength infrared hyperspectral data "mining" at Cuprite, NV," *Proc. SPIE* 9611, Imaging Spectrometry XX, 961107 (September 1, 2015); doi:10.1117/12.2187061; http://dx.doi.org/10.1117/12.2187061.

Takano, Y., and K.N. Liou, "Transfer of polarized infrared radiation in optically anisotropic media: application to horizontally oriented ice crystals: reply to comment," J. Opt. Soc. Am. A, **11**, p. 1378 (1994).

Torrance, K.E., and E.M. Sparrow, "Theory for off-specular reflection from roughened surfaces," J. Opt. Soc. Am., **57**(9):1105–1114 (1967).

Wiscombe, W.J., "The Delta-M Method: Rapid Yet Accurate Radiative Flux Calculations for Strongly Asymmetric Phase Functions," J. Atmos. Sci. **34**, 1408-1422 (1977).

Yang, P., L. Bi, B.A. Baum, K.-N. Liou, G.W. Kattawar, M.I. Mishchenko, and B. Cole, "Spectrally Consistent Scattering, Absorption, and Polarization Properties, of Atmospheric Ice Crystals at Wavelengths from 0.2 to 100 μm," J. Atmos. Sci., **70**, 330-347 (2013).

Appendix A: Computing Stokes Phase Matrices from *ISM* (Macroscopically *I*sotropic Mirror Symmetric Scattering *M*edium) Stokes Scattering Matrices

1. Introduction

Much of this text is taken verbatim from the book of Michael I. Mishchenko, Larry D. Travis, and Andrew A. Lacis (MTL) entitled, *Multiple Scattering of Light by Particles: Radiative Transfer and Coherent Backscattering* (Cambridge University Press, 2006, Cambridge). This text will be highlighted in dark blue.

2. From MTL, Section 2.6: Coherency matrix and Stokes parameters

"… Assuming that the medium is homogeneous and has no dispersion and losses, we specify the direction of propagation of a plane of electromagnetic wave by a unit vector **n** or, equivalently, by a couplet $\{\theta, \varphi\}$, where $\theta \in [0, \pi]$ is the polar (zenith) angle measured from the positive z-axis and $\varphi \in [0, 2\pi)$ is the azimuth angle measured from the positive x-axis in the clock-wise direction when looking in the direction of the positive z-axis. Since the component of the electric field vector along the direction of propagation **n** is equal to zero, the electric field at the observation point can be expressed as

$$\mathbf{E} = \mathbf{E}_\theta + \mathbf{E}_\varphi \quad ,$$

where $\mathbf{E}_\theta$ and $\mathbf{E}_\varphi$ are the θ- and φ-components of the electric field vector, respectively. The component

$$\mathbf{E}_\theta = E_\theta \hat{\boldsymbol{\theta}} \quad ,$$

lies in the meridional plane (i.e., the plane through **n** and the z-axis), whereas the component

$$\mathbf{E}_\varphi = E_\varphi \hat{\boldsymbol{\varphi}} \quad ,$$

is perpendicular to the plane [In the microwave remote-sensing literature, $\mathbf{E}_\theta$ and $\mathbf{E}_\varphi$ are often denoted as $\mathbf{E}_\mathrm{v}$ and $\mathbf{E}_\mathrm{h}$ and called the vertical and horizontal electric-field vector components, respectively]. $\boldsymbol{\theta}$ and $\boldsymbol{\varphi}$ are the corresponding unit vectors such that

$$\hat{\mathbf{n}} = \hat{\boldsymbol{\theta}} \times \hat{\boldsymbol{\varphi}} \quad .$$

…"

"Consider a plane electromagnetic wave propagating in a homogenous medium without dispersion and losses and given by:

$$\mathbf{E}(\mathbf{r},t) = \mathbf{E}_0 \exp\left(\mathrm{i} k \hat{\mathbf{n}} \cdot \mathbf{r} - \mathrm{i}\omega t\right) \qquad \textbf{(2.6.1)}$$

with a real k. The simplest complete set of linearly independent quadratic combinations of the electric field vector with nonzero time averages consists of the following four quantities:

$$E_\theta(\mathbf{r},t)\left[E_\theta(\mathbf{r},t)\right]^* = E_{0\theta} E_{0\theta}^* \,, \quad E_\theta(\mathbf{r},t)\left[E_\varphi(\mathbf{r},t)\right]^* = E_{0\theta} E_{0\varphi}^* \,,$$

$$E_\varphi(\mathbf{r},t)\left[E_\theta(\mathbf{r},t)\right]^* = E_{0\varphi} E_{0\theta}^* \,, \quad E_\varphi(\mathbf{r},t)\left[E_\varphi(\mathbf{r},t)\right]^* = E_{0\varphi} E_{0\varphi}^* \,,$$

The products of these quantities and ½ $\sqrt{(\varepsilon/\mu)}$ have the dimension of monochromatic energy flux …."

"…The Stokes parameters I, Q, U, and V are then defined as the elements of a 4×1 Stokes column vector **I** as follows:

$$\mathbf{I}=\begin{bmatrix} I \\ Q \\ U \\ V \end{bmatrix}=\frac{1}{2}\sqrt{\frac{\varepsilon}{\mu}}\begin{bmatrix} E_{0\theta}E_{0\theta}^{*}+E_{0\varphi}E_{0\varphi}^{*} \\ E_{0\theta}E_{0\theta}^{*}-E_{0\varphi}E_{0\varphi}^{*} \\ -E_{0\theta}E_{0\varphi}^{*}-E_{0\varphi}E_{0\theta}^{*} \\ \mathrm{i}\left(E_{0\varphi}E_{0\theta}^{*}-E_{0\theta}E_{0\varphi}^{*}\right) \end{bmatrix} . \tag{2.6.4}$$

…."

3. From MTL, Section 2.8: Rotation transformation rule for the Stokes parameters

"The Stokes parameters of a plane electromagnetic wave are always defined with respect to a reference plane containing the direction of wave propagation. If the reference plane is rotated about the direction of propagation then the Stokes parameters are modified according to a rotation transformation rule, which can be derived as follows. Consider a rotation of the coordinate axes θ and φ through an angle $0 \le \eta < 2\pi$ in the *clockwise* direction when looking in the direction of propagation (MTL Fig. 2.8.1). The transformation rule for rotation of a two-dimensional coordinate system yields

$$E'_{0\theta} = E_{0\theta}\cos\eta + E_{0\varphi}\sin\eta\,, \tag{2.8.1}$$

$$E'_{0\varphi} = -E_{0\theta}\sin\eta + E_{0\varphi}\cos\eta\,, \tag{2.8.2}$$

where the primes denote the electric-field vector components with respect to the new reference frame. It then follows from MTL Eq. (2.6.4) that the rotation transformation rule for the Stokes column vector is

$$\mathbf{I}' = \frac{1}{2}\sqrt{\frac{\varepsilon}{\mu}}\begin{bmatrix} \left|E_{0\theta}\cos\eta + E_{0\varphi}\sin\eta\right|^2 + \left|-E_{0\theta}\sin\eta + E_{0\varphi}\cos\eta\right|^2 \\ \left|E_{0\theta}\cos\eta + E_{0\varphi}\sin\eta\right|^2 - \left|-E_{0\theta}\sin\eta + E_{0\varphi}\cos\eta\right|^2 \\ \left(E_{0\theta}\cos\eta + E_{0\varphi}\sin\eta\right)\left(E_{0\theta}^{*}\sin\eta - E_{0\varphi}^{*}\cos\eta\right) + \left(E_{0\theta}\sin\eta - E_{0\varphi}\cos\eta\right)\left(E_{0\theta}^{*}\cos\eta + E_{0\varphi}^{*}\sin\eta\right) \\ \mathrm{i}\left[\left(E_{0\theta}\cos\eta + E_{0\varphi}\sin\eta\right)\left(E_{0\theta}^{*}\sin\eta - E_{0\varphi}^{*}\cos\eta\right) - \left(E_{0\theta}\sin\eta - E_{0\varphi}\cos\eta\right)\left(E_{0\theta}^{*}\cos\eta + E_{0\varphi}^{*}\sin\eta\right)\right] \end{bmatrix}$$

$$= \frac{1}{2}\sqrt{\frac{\varepsilon}{\mu}}\begin{bmatrix} E_{0\theta}E_{0\theta}^{*} + E_{0\varphi}E_{0\varphi}^{*} \\ \left(\cos^2\eta - \sin^2\eta\right)E_{0\theta}E_{0\theta}^{*} + 2\sin\eta\cos\eta\left(E_{0\theta}E_{0\varphi}^{*} + E_{0\varphi}E_{0\theta}^{*}\right) - \left(\cos^2\eta - \sin^2\eta\right)E_{0\varphi}E_{0\varphi}^{*} \\ 2\sin\eta\cos\eta\,E_{0\theta}E_{0\theta}^{*} - \left(\cos^2\eta - \sin^2\eta\right)\left(E_{0\theta}E_{0\varphi}^{*} + E_{0\varphi}E_{0\theta}^{*}\right) - 2\sin\eta\cos\eta\,E_{0\varphi}E_{0\varphi}^{*} \\ \mathrm{i}\left(E_{0\varphi}E_{0\theta}^{*} - E_{0\theta}E_{0\varphi}^{*}\right) \end{bmatrix}$$

$$= \frac{1}{2}\sqrt{\frac{\varepsilon}{\mu}}\begin{bmatrix} E_{0\theta}E_{0\theta}^{*} + E_{0\varphi}E_{0\varphi}^{*} \\ \cos 2\eta\left(E_{0\theta}E_{0\theta}^{*} - E_{0\varphi}E_{0\varphi}^{*}\right) + \sin 2\eta\left(E_{0\theta}E_{0\varphi}^{*} + E_{0\varphi}E_{0\theta}^{*}\right) \\ \sin 2\eta\left(E_{0\theta}E_{0\theta}^{*} - E_{0\varphi}E_{0\varphi}^{*}\right) - \cos 2\eta\left(E_{0\theta}E_{0\varphi}^{*} + E_{0\varphi}E_{0\theta}^{*}\right) \\ \mathrm{i}\left(E_{0\varphi}E_{0\theta}^{*} - E_{0\theta}E_{0\varphi}^{*}\right) \end{bmatrix}$$

$$= \frac{1}{2}\sqrt{\frac{\varepsilon}{\mu}}\begin{bmatrix} 1 & 0 & 0 & 0 \\ 0 & \cos 2\eta & -\sin 2\eta & 0 \\ 0 & \sin 2\eta & \cos 2\eta & 0 \\ 0 & 0 & 0 & 1 \end{bmatrix}\begin{bmatrix} E_{0\theta}E_{0\theta}^{*} + E_{0\varphi}E_{0\varphi}^{*} \\ E_{0\theta}E_{0\theta}^{*} - E_{0\varphi}E_{0\varphi}^{*} \\ -E_{0\theta}E_{0\varphi}^{*} - E_{0\varphi}E_{0\theta}^{*} \\ \mathrm{i}\left(E_{0\varphi}E_{0\theta}^{*} - E_{0\theta}E_{0\varphi}^{*}\right) \end{bmatrix} \tag{i}$$

$$\mathbf{I}' = \mathbf{L}(\eta)\mathbf{I} \quad , \tag{2.8.3}$$

where

$$\mathbf{L}(\eta) = \begin{bmatrix} 1 & 0 & 0 & 0 \\ 0 & \cos 2\eta & -\sin 2\eta & 0 \\ 0 & \sin 2\eta & \cos 2\eta & 0 \\ 0 & 0 & 0 & 1 \end{bmatrix} . \tag{2.8.4}$$

…."

4. From MTL, Section 11.3: Phase matrix

"Knowledge of the scattering matrix averaged over particle states $\langle \mathbf{F}(\Theta) \rangle_\xi$ can be used to calculate the average Stokes phase matrix for an ISM. Assume that $0 < \Delta\varphi \equiv \varphi^{sca} - \varphi^{inc} < \pi$ and consider the phase matrices $\langle \mathbf{Z}(\theta^{\rm sca}, \varphi^{\rm sca}; \theta^{\rm inc}, \varphi^{inc}) \rangle_\xi$ and $\langle \mathbf{Z}(\theta^{\rm sca}, \varphi^{inc}; \theta^{\rm inc}, \varphi^{\rm sca}) \rangle_\xi$. The second matrix involves the same polar angles of incident and scattered beams as the first, but the azimuth angles are switched, as indicated in their respective scattering geometries; these are shown in MTL Figs. 11.3.1(a) and (b). The phase matrix links the Stokes vectors of the incident and scattered beams, specified relative to their respective meridional planes. Therefore, to compute the Stokes vector of the scattered beam with respect to its meridional plane, we must:

- Calculate the Stokes vector of the incident bean with respect to the scattering plane.
- Multiply it by the scattering matrix, thereby obtaining the Stokes vector of the scattered beam with respect to the scattering plane.
- Compute the Stokes vector of the scattered beam with respect to its meridional plane (Chandrasekhar, 1950).

This procedure involves two rotations of the reference plane, as shown in MTL Figs. 11.3.1(a) and (b), and yields [From MTL Eq. (2.8.4), $\mathbf{L}(\eta) = \mathbf{L}(\eta \pm \pi)$; the ISM scattering matrix is defined in MTL Eq. (11.2.1)]

$$\left\langle \mathbf{Z}\left(\theta^{sca}, \varphi^{sca}; \theta^{inc}, \varphi^{inc}\right) \right\rangle_\xi = \mathbf{L}(-\sigma_2) \left\langle F(\Theta) \right\rangle_\xi \mathbf{L}(\pi - \sigma_1)$$

$$\left\langle \mathbf{Z}\left(\theta^{sca}, \varphi^{sca}; \theta^{inc}, \varphi^{inc}\right) \right\rangle_\xi = \mathbf{L}(-\sigma_2) \left\langle F(\Theta) \right\rangle_\xi \mathbf{L}(-\sigma_1) =$$

$$\begin{bmatrix} 1 & 0 & 0 & 0 \\ 0 & \cos 2\sigma_2 & \sin 2\sigma_2 & 0 \\ 0 & -\sin 2\sigma_2 & \cos 2\sigma_2 & 0 \\ 0 & 0 & 0 & 1 \end{bmatrix} \begin{bmatrix} \langle F_{11}(\Theta)\rangle_\xi & \langle F_{12}(\Theta)\rangle_\xi & 0 & 0 \\ \langle F_{12}(\Theta)\rangle_\xi & \langle F_{22}(\Theta)\rangle_\xi & 0 & 0 \\ 0 & 0 & \langle F_{33}(\Theta)\rangle_\xi & \langle F_{34}(\Theta)\rangle_\xi \\ 0 & 0 & -\langle F_{34}(\Theta)\rangle_\xi & \langle F_{44}(\Theta)\rangle_\xi \end{bmatrix} \begin{bmatrix} 1 & 0 & 0 & 0 \\ 0 & \cos 2\sigma_1 & \sin 2\sigma_1 & 0 \\ 0 & -\sin 2\sigma_1 & \cos 2\sigma_1 & 0 \\ 0 & 0 & 0 & 1 \end{bmatrix} \tag{ii}$$

$$\left\langle \mathbf{Z}\left(\theta^{sca}, \varphi^{sca}; \theta^{inc}, \varphi^{inc}\right) \right\rangle_\xi =$$

$$\begin{bmatrix} 1 & 0 & 0 & 0 \\ 0 & \cos 2\sigma_2 & \sin 2\sigma_2 & 0 \\ 0 & -\sin 2\sigma_2 & \cos 2\sigma_2 & 0 \\ 0 & 0 & 0 & 1 \end{bmatrix} \begin{bmatrix} \langle F_{11}(\Theta)\rangle_\xi & \cos 2\sigma_1 \langle F_{12}(\Theta)\rangle_\xi & \sin 2\sigma_1 \langle F_{12}(\Theta)\rangle_\xi & 0 \\ \langle F_{12}(\Theta)\rangle_\xi & \cos 2\sigma_1 \langle F_{22}(\Theta)\rangle_\xi & \sin 2\sigma_1 \langle F_{22}(\Theta)\rangle_\xi & 0 \\ 0 & -\sin 2\sigma_1 \langle F_{33}(\Theta)\rangle_\xi & \cos 2\sigma_1 \langle F_{33}(\Theta)\rangle_\xi & \langle F_{34}(\Theta)\rangle_\xi \\ 0 & \sin 2\sigma_1 \langle F_{34}(\Theta)\rangle_\xi & -\cos 2\sigma_1 \langle F_{34}(\Theta)\rangle_\xi & \langle F_{44}(\Theta)\rangle_\xi \end{bmatrix} \tag{iii}$$

$$\left\langle \mathbf{Z}\left(\theta^{sca},\varphi^{sca};\theta^{inc},\varphi^{inc}\right)\right\rangle_{\xi} =$$

$$\begin{bmatrix} \langle F_{11}(\Theta)\rangle_{\xi} & C_1\langle F_{12}(\Theta)\rangle_{\xi} & S_1\langle F_{12}(\Theta)\rangle_{\xi} & 0 \\ C_2\langle F_{12}(\Theta)\rangle_{\xi} & C_2C_1\langle F_{22}(\Theta)\rangle_{\xi} - S_2S_1\langle F_{33}(\Theta)\rangle_{\xi} & C_2S_1\langle F_{22}(\Theta)\rangle_{\xi} + S_2C_1\langle F_{33}(\Theta)\rangle_{\xi} & S_2\langle F_{34}(\Theta)\rangle_{\xi} \\ -S_2\langle F_{12}(\Theta)\rangle_{\xi} & -S_2C_1\langle F_{22}(\Theta)\rangle_{\xi} - C_2S_1\langle F_{33}(\Theta)\rangle_{\xi} & -S_2S_1\langle F_{22}(\Theta)\rangle_{\xi} + C_2C_1\langle F_{33}(\Theta)\rangle_{\xi} & C_2\langle F_{34}(\Theta)\rangle_{\xi} \\ 0 & S_1\langle F_{34}(\Theta)\rangle_{\xi} & -C_1\langle F_{34}(\Theta)\rangle_{\xi} & \langle F_{44}(\Theta)\rangle_{\xi} \end{bmatrix} \quad \textbf{(11.3.1)}$$

$$\left\langle \mathbf{Z}\left(\theta^{sca},\varphi^{inc};\theta^{inc},\varphi^{sca}\right)\right\rangle_{\xi} = \mathbf{L}(\sigma_2-\pi)\langle F(\Theta)\rangle_{\xi}\mathbf{L}(\sigma_1)$$

$$\left\langle \mathbf{Z}\left(\theta^{sca},\varphi^{inc};\theta^{inc},\varphi^{sca}\right)\right\rangle_{\xi} = \mathbf{L}(\sigma_2)\langle F(\Theta)\rangle_{\xi}\mathbf{L}(\sigma_1) =$$

$$\begin{bmatrix} 1 & 0 & 0 & 0 \\ 0 & \cos2\sigma_2 & -\sin2\sigma_2 & 0 \\ 0 & \sin2\sigma_2 & \cos2\sigma_2 & 0 \\ 0 & 0 & 0 & 1 \end{bmatrix} \begin{bmatrix} \langle F_{11}(\Theta)\rangle_{\xi} & \langle F_{12}(\Theta)\rangle_{\xi} & 0 & 0 \\ \langle F_{12}(\Theta)\rangle_{\xi} & \langle F_{22}(\Theta)\rangle_{\xi} & 0 & 0 \\ 0 & 0 & \langle F_{33}(\Theta)\rangle_{\xi} & \langle F_{34}(\Theta)\rangle_{\xi} \\ 0 & 0 & -\langle F_{34}(\Theta)\rangle_{\xi} & \langle F_{44}(\Theta)\rangle_{\xi} \end{bmatrix} \begin{bmatrix} 1 & 0 & 0 & 0 \\ 0 & \cos2\sigma_1 & -\sin2\sigma_1 & 0 \\ 0 & \sin2\sigma_1 & \cos2\sigma_1 & 0 \\ 0 & 0 & 0 & 1 \end{bmatrix} \quad \textbf{(iv)}$$

$$\left\langle \mathbf{Z}\left(\theta^{sca},\varphi^{inc};\theta^{inc},\varphi^{sca}\right)\right\rangle_{\xi} =$$

$$\begin{bmatrix} 1 & 0 & 0 & 0 \\ 0 & \cos2\sigma_2 & -\sin2\sigma_2 & 0 \\ 0 & \sin2\sigma_2 & \cos2\sigma_2 & 0 \\ 0 & 0 & 0 & 1 \end{bmatrix} \begin{bmatrix} \langle F_{11}(\Theta)\rangle_{\xi} & \cos2\sigma_1\langle F_{12}(\Theta)\rangle_{\xi} & -\sin2\sigma_1\langle F_{12}(\Theta)\rangle_{\xi} & 0 \\ \langle F_{12}(\Theta)\rangle_{\xi} & \cos2\sigma_1\langle F_{22}(\Theta)\rangle_{\xi} & -\sin2\sigma_1\langle F_{22}(\Theta)\rangle_{\xi} & 0 \\ 0 & \sin2\sigma_1\langle F_{33}(\Theta)\rangle_{\xi} & \cos2\sigma_1\langle F_{33}(\Theta)\rangle_{\xi} & \langle F_{34}(\Theta)\rangle_{\xi} \\ 0 & -\sin2\sigma_1\langle F_{34}(\Theta)\rangle_{\xi} & -\cos2\sigma_1\langle F_{34}(\Theta)\rangle_{\xi} & \langle F_{44}(\Theta)\rangle_{\xi} \end{bmatrix} \quad \textbf{(v)}$$

$$\left\langle \mathbf{Z}\left(\theta^{sca},\varphi^{inc};\theta^{inc},\varphi^{sca}\right)\right\rangle_{\xi} =$$

$$\begin{bmatrix} \langle F_{11}(\Theta)\rangle_{\xi} & C_1\langle F_{12}(\Theta)\rangle_{\xi} & -S_1\langle F_{12}(\Theta)\rangle_{\xi} & 0 \\ C_2\langle F_{12}(\Theta)\rangle_{\xi} & C_2C_1\langle F_{22}(\Theta)\rangle_{\xi} - S_2S_1\langle F_{33}(\Theta)\rangle_{\xi} & -C_2S_1\langle F_{22}(\Theta)\rangle_{\xi} - S_2C_1\langle F_{33}(\Theta)\rangle_{\xi} & -S_2\langle F_{34}(\Theta)\rangle_{\xi} \\ S_2\langle F_{12}(\Theta)\rangle_{\xi} & S_2C_1\langle F_{22}(\Theta)\rangle_{\xi} + C_2S_1\langle F_{33}(\Theta)\rangle_{\xi} & -S_2S_1\langle F_{22}(\Theta)\rangle_{\xi} + C_2C_1\langle F_{33}(\Theta)\rangle_{\xi} & C_2\langle F_{34}(\Theta)\rangle_{\xi} \\ 0 & -S_1\langle F_{34}(\Theta)\rangle_{\xi} & -C_1\langle F_{34}(\Theta)\rangle_{\xi} & \langle F_{44}(\Theta)\rangle_{\xi} \end{bmatrix} \quad \textbf{(11.3.2)}$$

where

$$C_i = \cos2\sigma_i\,, \quad S_i = \sin2\sigma_i\,, \quad i = 1, 2 \quad , \qquad \textbf{(11.3.3)}$$

and the rotation matrix **L** is defined by MTL Eq. (2.8.4). (Recall that a rotation angle is positive if the rotation is performed in the clockwise direction when one is looking in the direction of propagation; see MTL Section 2.8.) The scattering angle Θ and the reference plane rotation angles σ_1 and σ_2 can be calculated from θ^{sca}, θ^{inc}, φ^{sca}, and φ^{inc} using the cosine rule in spherical trigonometry:

$$\cos\Theta = \cos\theta^{sca}\cos\theta^{inc} + \sin\theta^{sca}\sin\theta^{inc}\cos\left(\varphi^{sca} - \varphi^{inc}\right) \quad , \qquad \textbf{(11.3.4)}$$

$$\cos\sigma_1 = \frac{\cos\theta^{sca} - \cos\theta^{inc}\cos\Theta}{\sin\theta^{inc}\sin\Theta} \quad \textit{and} \tag{11.3.5}$$

$$\cos\sigma_2 = \frac{\cos\theta^{inc} - \cos\theta^{sca}\cos\Theta}{\sin\theta^{sca}\sin\Theta} \quad . \tag{11.3.6}$$

…."

5. Computing Rotation Angles σ_1 and σ_2 (MTL Section 11.3 Phase matrix)

Since the scattering angle Θ is symmetric with regards to interchange of the zenith angles, θ^{inc} and θ^{sca}, the expression for rotation angle σ_2 can always be obtained from the expression for σ_1:

$$\sigma_1 \equiv \sigma_1\left(\theta^{inc}, \theta^{sca}, \Delta\varphi\right) \quad \textit{and} \quad \sigma_2 \equiv \sigma_2\left(\theta^{inc}, \theta^{sca}, \Delta\varphi\right) = \sigma_1\left(\theta^{sca}, \theta^{inc}, \Delta\varphi\right) \tag{vi}$$

For the remainder of this document, expressions will be derived involving σ_1 only; the analogous expressions involving σ_2 will simply be defined by switching θ^{inc} and θ^{sca}.

The expression for the cos σ_1, MTL Eq. (11.3.5) can be rewritten to eliminate sin θ^{inc} from the denominator, thereby removing the singularity problem that arises when sin θ^{inc} is zero:

$$\cos\sigma_1 = \frac{\cos\theta^{sca} - \cos\theta^{inc}\left(\cos\theta^{sca}\cos\theta^{inc} + \sin\theta^{sca}\sin\theta^{inc}\cos\Delta\varphi\right)}{\sin\theta^{inc}\sin\Theta}$$

$$= \frac{\cos\theta^{sca}\sin^2\theta^{inc} - \sin\theta^{sca}\cos\theta^{inc}\sin\theta^{inc}\cos\Delta\varphi}{\sin\theta^{inc}\sin\Theta} = \frac{\cos\theta^{sca}\sin\theta^{inc} - \sin\theta^{sca}\cos\theta^{inc}\cos\Delta\varphi}{\sin\Theta} \tag{vii}$$

$$= \frac{\cos\theta^{sca}\sin\theta^{inc} - \sin\theta^{sca}\cos\theta^{inc} + \sin\theta^{sca}\cos\theta^{inc}\left(1-\cos\Delta\varphi\right)}{\sin\Theta} = \frac{2\sin\theta^{sca}\cos\theta^{inc}\sin^2\frac{\Delta\varphi}{2} - \sin\Delta\theta}{\sin\Theta}$$

$$\cos\sigma_2 = \frac{2\sin\theta^{inc}\cos\theta^{sca}\sin^2\frac{\Delta\varphi}{2} + \sin\Delta\theta}{\sin\Theta} \tag{viii}$$

where

$$\Delta\theta \equiv \theta^{sca} - \theta^{inc} \tag{ix}$$

The definition of the cosine terms remains problematic when sin Θ is near zero. This will occur when the incident and scattering directions are nearly parallel [cos Θ ≈ +1] and when these vectors are nearly anti-parallel [cos Θ ≈ –1].

One could compute the sin Θ as $\sqrt{(1 - \cos^2\Theta)}$, substitute that result into Eqs. (vii) and (viii), and then determine sin σ_1 as $\sqrt{(1 - \cos^2\sigma_1)}$ [The angles of *proper* spherical triangles in spherical trigonometry are (by convention) less than π]. However, that can be numerically problematic when $\cos^2\Theta$ is near 1, and, as it turns out, a simple form can be derived for sin σ_1. In terms of $\Delta\varphi$ and $\Delta\theta$, the cosine and sine of the scattering angle Θ can be written

$$\begin{aligned}\cos\Theta &= \cos\theta^{sca}\cos\theta^{inc} + \sin\theta^{sca}\sin\theta^{inc}\cos\Delta\varphi \\ &= \cos\theta^{sca}\cos\theta^{inc} + \sin\theta^{sca}\sin\theta^{inc} - \sin\theta^{sca}\sin\theta^{inc}\left(1-\cos\Delta\varphi\right) \\ &= \cos\Delta\theta - 2\sin\theta^{sca}\sin\theta^{inc}\sin^2\frac{\Delta\varphi}{2}\end{aligned} \tag{x}$$

$$\sin\Theta = \left|\sqrt{\sin^2\Delta\theta + 4\cos\Delta\theta\sin\theta^{sca}\sin\theta^{inc}\sin^2\frac{\Delta\varphi}{2} - 4\sin^2\theta^{sca}\sin^2\theta^{inc}\sin^4\frac{\Delta\varphi}{2}}\right| \tag{xi}$$

Inserting this expression into the denominator of Eq. (vii), one obtains:

$$\cos\sigma_1 = \frac{2\sin\theta^{sca}\cos\theta^{inc}\sin^2\frac{\Delta\varphi}{2} - \sin\Delta\theta}{\sqrt{\sin^2\Delta\theta + 4\cos\Delta\theta\sin\theta^{sca}\sin\theta^{inc}\sin^2\frac{\Delta\varphi}{2} - 4\sin^2\theta^{sca}\sin^2\theta^{inc}\sin^4\frac{\Delta\varphi}{2}}} \tag{xii}$$

The cosine-squared expression has common terms in the numerator and denominator:

$$\cos^2\sigma_1 = \frac{\sin^2\Delta\theta - 4\sin\Delta\theta\sin\theta^{sca}\cos\theta^{inc}\sin^2\frac{\Delta\varphi}{2} + 4\sin^2\theta^{sca}\cos^2\theta^{inc}\sin^4\frac{\Delta\varphi}{2}}{\sin^2\Delta\theta + 4\cos\Delta\theta\sin\theta^{sca}\sin\theta^{inc}\sin^2\frac{\Delta\varphi}{2} - 4\sin^2\theta^{sca}\sin^2\theta^{inc}\sin^4\frac{\Delta\varphi}{2}} \tag{xiii}$$

A simple expression can now be derived for the sine-squared of σ_1 and σ_2:

$$\begin{aligned}\sin^2\sigma_1 &= 1 - \frac{\sin^2\Delta\theta - 4\sin\Delta\theta\sin\theta^{sca}\cos\theta^{inc}\sin^2\frac{\Delta\varphi}{2} + 4\sin^2\theta^{sca}\cos^2\theta^{inc}\sin^4\frac{\Delta\varphi}{2}}{\sin^2\Delta\theta + 4\cos\Delta\theta\sin\theta^{sca}\sin\theta^{inc}\sin^2\frac{\Delta\varphi}{2} - 4\sin^2\theta^{sca}\sin^2\theta^{inc}\sin^4\frac{\Delta\varphi}{2}} \\ &= \frac{4\sin\theta^{sca}\left(\cos\Delta\theta\sin\theta^{inc} + \sin\Delta\theta\cos\theta^{inc}\right)\sin^2\frac{\Delta\varphi}{2} - 4\sin^2\theta^{sca}\left(\sin^2\theta^{inc} + \cos^2\theta^{inc}\right)\sin^4\frac{\Delta\varphi}{2}}{\sin^2\Delta\theta + 4\cos\Delta\theta\sin\theta^{sca}\sin\theta^{inc}\sin^2\frac{\Delta\varphi}{2} - 4\sin^2\theta^{sca}\sin^2\theta^{inc}\sin^4\frac{\Delta\varphi}{2}} \\ &= \frac{4\sin\theta^{sca}\sin\left(\theta^{inc} + \Delta\theta\right)\sin^2\frac{\Delta\varphi}{2} - 4\sin^2\theta^{sca}\sin^4\frac{\Delta\varphi}{2}}{\sin^2\Theta} = \frac{4\sin^2\theta^{sca}\sin^2\frac{\Delta\varphi}{2}\cos^2\frac{\Delta\varphi}{2}}{\sin^2\Theta} \\ &= \frac{\sin^2\theta^{sca}\sin^2\Delta\varphi}{\sin^2\Theta}\end{aligned} \tag{xiv}$$

$$\sin^2\sigma_2 = \frac{\sin^2\theta^{inc}\sin^2\Delta\varphi}{\sin^2\Theta} \tag{xv}$$

It is of interest to consider some special cases, using the expressions of Eqs. (vii), (viii), (x), (xi), (xiv). and (xv). If the scattered photon direction is in the same meridional (vertical) half-plane as the incident direction ($\Delta\varphi = 0$), then

For $\Delta\varphi = 0$

$$\sin\Theta = \sin\left|\Delta\theta\right|$$

$$\sin^2\sigma_1 = 0 \quad and \quad \cos\sigma_1 = \frac{-\sin\Delta\theta}{\sin\left|\Delta\theta\right|} \quad \Rightarrow \quad \sigma_1 = \begin{cases} \pi & if\ \theta^{sca} > \theta^{inc} \\ 0 & if\ \theta^{inc} > \theta^{sca} \end{cases} \qquad \textbf{(xvi)}$$

$$\sin^2\sigma_2 = 0 \quad and \quad \cos\sigma_2 = \frac{\sin\Delta\theta}{\sin\left|\Delta\theta\right|} \quad \Rightarrow \quad \sigma_2 = \begin{cases} 0 & if\ \theta^{sca} > \theta^{inc} \\ \pi & if\ \theta^{inc} > \theta^{sca} \end{cases}$$

If the scattered photon direction is in the opposite meridional (vertical) half-plane as the incident direction ($\Delta\varphi = \pi$), then

For $\Delta\varphi = \pi$

$$\cos\Theta = \cos\Delta\theta - 2\sin\theta^{sca}\sin\theta^{inc} = \cos\theta^{sca}\cos\theta^{inc} - \sin\theta^{sca}\sin\theta^{inc} = \cos\left(\theta^{sca} + \theta^{inc}\right)$$

$$\cos\Theta = -\cos\left(\theta^{sca} + \theta^{inc} - \pi\right) \quad ; \quad \sin\Theta = \sin\left|\theta^{sca} + \theta^{inc} - \pi\right| \qquad \textbf{(xvii)}$$

$$\sin^2\sigma_1 = 0 = \sin^2\sigma_2 \quad and \quad \cos\sigma_1 = \frac{\cos\theta^{sca}\sin\theta^{inc} + \sin\theta^{sca}\cos\theta^{inc}}{\sin\left|\theta^{sca} + \theta^{inc} - \pi\right|} = \frac{\sin\left(\theta^{sca} + \theta^{inc}\right)}{\sin\left|\theta^{sca} + \theta^{inc} - \pi\right|} = \cos\sigma_2$$

$$\Rightarrow \quad \sigma_1 = \sigma_2 = \begin{cases} 0 & if\ \theta^{sca} + \theta^{inc} < \pi \\ \pi & if\ \theta^{inc} + \theta^{sca} > \pi \end{cases}$$

Eqs. (xii) and (xiii) verify that no rotation is required if the scattering plane is already a meridional plane.

If the incident and scattered zenith angles are identical ($\Delta\theta = 0$; $\theta^{sca} = \theta^{inc}$), then

For $\Delta\theta = 0$

$$\cos\Theta = 1 - 2\sin^2\theta^{inc}\sin^2\frac{\Delta\varphi}{2}$$

$$\sin\Theta = 2\sin\theta^{inc}\sin\frac{\Delta\varphi}{2}\sqrt{1 - \sin^2\theta^{inc}\sin^2\frac{\Delta\varphi}{2}}$$

$$\sin^2\sigma_1 = \sin^2\sigma_2 = \frac{\sin^2\theta^{inc}\sin^2\Delta\varphi}{\sin^2\Theta} = \frac{\cos^2\frac{\Delta\varphi}{2}}{1 - \sin^2\theta^{inc}\sin^2\frac{\Delta\varphi}{2}} \quad and$$

$$\cos\sigma_1 = \cos\sigma_2 = \frac{\cos\theta^{inc}\sin\theta^{inc}\left(1 - \cos\Delta\varphi\right)}{2\sin\theta^{inc}\sin\frac{\Delta\varphi}{2}\sqrt{1 - \sin^2\theta^{inc}\sin^2\frac{\Delta\varphi}{2}}} = \frac{\cos\theta^{inc}\sin\frac{\Delta\varphi}{2}}{\sqrt{1 - \sin^2\theta^{inc}\sin^2\frac{\Delta\varphi}{2}}} \qquad \textbf{(xviii)}$$

If the incident and scattered zenith angles sum to π ($\theta^{sca} + \theta^{inc} = \pi$), as with back scattering, then

$$\underline{\textbf{For } \boldsymbol{\theta}^{\textbf{sca}} + \boldsymbol{\theta}^{\textbf{inc}} = \boldsymbol{\pi}}$$

$$\cos\Theta = \cos\left(\pi - 2\,\theta^{inc}\right) - 2\sin\left(\pi - \theta^{inc}\right)\sin\theta^{inc}\sin^2\frac{\Delta\varphi}{2} = -\cos\left(2\,\theta^{inc}\right) - 2\sin^2\theta^{inc}\sin^2\frac{\Delta\varphi}{2}$$

$$\cos\Theta = -1 + 2\sin^2\theta^{inc}\cos^2\frac{\Delta\varphi}{2} \quad ; \quad \sin\Theta = 2\sin\theta^{inc}\cos\frac{\Delta\varphi}{2}\sqrt{1-\sin^2\theta^{inc}\cos^2\frac{\Delta\varphi}{2}}$$

$$\sin^2\sigma_1 = \frac{\sin^2\left(\pi-\theta^{inc}\right)\sin^2\Delta\varphi}{2\sin^2\theta^{inc}\cos^2\frac{\Delta\varphi}{2}\left(1-\sin^2\theta^{inc}\cos^2\frac{\Delta\varphi}{2}\right)} = \frac{\sin^2\frac{\Delta\varphi}{2}}{1-\sin^2\theta^{inc}\cos^2\frac{\Delta\varphi}{2}} = \sin\sigma_2 \quad \textit{and}$$

$$\cos\sigma_1 = \frac{\cos\left(\pi-\theta^{inc}\right)\sin\theta^{inc} - \sin\left(\pi-\theta^{inc}\right)\cos\theta^{inc}\cos\Delta\varphi}{2\sin\theta^{inc}\cos\frac{\Delta\varphi}{2}\sqrt{1-\sin^2\theta^{inc}\cos^2\frac{\Delta\varphi}{2}}} = \frac{-\cos\theta^{inc}\left(1+\cos\Delta\varphi\right)}{2\cos\frac{\Delta\varphi}{2}\sqrt{1-\sin^2\theta^{inc}\cos^2\frac{\Delta\varphi}{2}}}$$

$$\cos\sigma_1 = \frac{-\cos\theta^{inc}\cos\frac{\Delta\varphi}{2}}{\sqrt{1-\sin^2\theta^{inc}\cos^2\frac{\Delta\varphi}{2}}} = -\cos\sigma_2 \qquad \textbf{(xix)}$$

At first, it seems problematic that the $\Delta\varphi = 0$ expression for the $\sin^2\sigma_1$, Eq. (xvi), is zero, but when the $\Delta\theta = 0$ expression for the $\sin^2\sigma_1$, Eq. (xviii) is evaluated at $\Delta\varphi = 0$, one obtains $\sin^2\sigma_1$ equals one! However, the $(\Delta\theta, \Delta\varphi) = (0, 0)$ corresponds to forward scattering, and the σ_i are not uniquely defined. The same issue arises with backscatter. When $\Delta\varphi = \pi$, Eq. (xviii), the $\sin^2\sigma_1$ equals 0, but setting $\Delta\varphi$ to π in Eq. (xix) gives $\sin^2\sigma_1 = 1$.

In MTL Eqs. (11.3.1) and (11.3.2), the circular quantities that arise are functions of the rotation angles doubled, $\sin 2\sigma_i$ and $\cos 2\sigma_i$. The expressions for $\cos\sigma_i$ and $\sin^2\sigma_i$ in Eqs. (vii), (viii), (xiv), and (xv) are simple enough that one can evaluate these double angle formulas explicitly. Furthermore, the denominator of the double angle expressions is the square of $\sin\Theta$. Thus, no square root must be taken. Thus, $\cos 2\sigma_i$ and $\sin^2 2\sigma_i$ can defined directly in terms of the incident zenith and azimuth angles θ^{inc} and φ^{inc}, and scattering zenith and azimuth angles θ^{sca} and φ^{sca}.

$$\sin^2\Theta = \sin^2\Delta\theta + 4\cos\Delta\theta\sin\theta^{sca}\sin\theta^{inc}\sin^2\frac{\Delta\varphi}{2} - 4\sin^2\theta^{sca}\sin^2\theta^{inc}\sin^4\frac{\Delta\varphi}{2}$$

$$\cos 2\sigma_1 = 1 \quad \textit{and} \quad \sin 2\sigma_1 = 0 \quad \textit{if } \sin^2\Theta = 0\,; \quad \textit{otherwise}$$

$$\cos 2\sigma_1 = \cos^2\sigma_1 - \sin^2\sigma_1 = \frac{\left(2\sin\theta^{sca}\cos\theta^{inc}\sin^2\frac{\Delta\varphi}{2} - \sin\Delta\theta\right)^2 - \left(\sin\theta^{sca}\sin\Delta\varphi\right)^2}{\sin^2\Theta} \qquad \textbf{(xx)}$$

$$\sin^2 2\sigma_1 = \left(2\sin\sigma_1\cos\sigma_1\right)^2 = \frac{4\sin^2\theta^{sca}\sin^2\Delta\varphi\left(2\sin\theta^{sca}\cos\theta^{inc}\sin^2\frac{\Delta\varphi}{2} - \sin\Delta\theta\right)^2}{\sin^4\Theta}$$

From symmetry, the expressions for $\cos 2\sigma_2$ and $\sin^2 2\sigma_2$ are also obtained:

$$\cos 2\sigma_2 = 1 \quad \textit{and} \quad \sin 2\sigma_2 = 0 \quad \textit{if } \sin^2\Theta = 0; \quad \textit{otherwise}$$

$$\cos 2\sigma_2 = \frac{\left(2\sin\theta^{inc}\cos\theta^{sca}\sin^2\frac{\Delta\varphi}{2} + \sin\Delta\theta\right)^2 - \left(\sin\theta^{inc}\sin\Delta\varphi\right)^2}{\sin^2\Theta} \qquad \textbf{(xxi)}$$

$$\sin^2 2\sigma_2 = \frac{4\sin^2\theta^{inc}\sin^2\Delta\varphi\left(2\sin\theta^{inc}\cos\theta^{sca}\sin^2\frac{\Delta\varphi}{2} + \sin\Delta\theta\right)^2}{\sin^4\Theta}$$

Given that the range of $\Delta\varphi$, σ_1, and σ_2 have all been restricted to (0, π), one could certainly write the expressions for $\sin 2\sigma_1$ and $\sin 2\sigma_2$ rather than the square of each of these terms. We choose not to do that, because the range of these variables is to be extended in the next section and the $\sin 2\sigma_1$ and $\sin 2\sigma_2$ expressions written here would be incorrect given that extension.

6. Combining $\langle \mathbf{Z}(\theta^{sca}, \varphi^{sca}; \theta^{inc}, \varphi^{inc})\rangle_\xi$ and $\langle \mathbf{Z}(\theta^{sca}, \varphi^{inc}; \theta^{inc}, \varphi^{sca})\rangle_\xi$ into a single expression

Separate expression were derived for $\langle \mathbf{Z}(\theta^{sca}, \varphi^{sca}; \theta^{inc}, \varphi^{inc})\rangle_\xi$ and $\langle \mathbf{Z}(\theta^{sca}, \varphi^{inc}; \theta^{inc}, \varphi^{sca})\rangle_\xi$ in MTL, Eqs. (11.3.1 and 11.3.2), with $0 < \Delta\varphi \equiv \varphi^{sca} - \varphi^{inc} < \pi$. The analysis also restricts σ_1 and σ_2 to be between 0 and π. With this approach, one need only determine expressions for $\cos\sigma_1$ and $\cos\sigma_2$ [MTL Eqs. (11.3.4) and (11.3.5)]; the $\sin\sigma_i$ equals to $|\sqrt{(1 - \cos^2\sigma_i)}|$ for i= 1, 2.

Computationally, it is considerably more convenient to have a single expression for the phase matrix, $\langle \mathbf{Z}(\theta^{sca}, \varphi^{sca}; \theta^{inc}, \varphi^{inc})\rangle_\xi$, with the domains of $\Delta\varphi$, σ_1, and σ_2 all expanded to range from $-\pi$ to π. According to the convention that the electromagnetic wave rotation angle is positive if the rotation is performed in the clockwise direction when one is looking in the direction of propagation (MTL Section 2.8), MTL Figs. 11.3.1(a) and (b) indicate that σ_1 and σ_2 will be positive when $\Delta\varphi$ is negative, and vice versa. The implication is that the square root of Eqs. (xiv) and (xv) are:

$$\sin\sigma_1 = -\frac{\sin\theta^{sca}\sin\Delta\varphi}{\sin\Theta} \quad \textit{and} \quad \sin\sigma_2 = -\frac{\sin\theta^{inc}\sin\Delta\varphi}{\sin\Theta} \qquad \textbf{(xxii)}$$

The expressions for $\cos\sigma_1$ and $\cos\sigma_2$, with $\Delta\theta \equiv \theta^{sca} - \theta^{inc}$, remain unchanged:

$$\cos\sigma_1 = \frac{2\sin\theta^{sca}\cos\theta^{inc}\sin^2\frac{\Delta\varphi}{2} - \sin\Delta\theta}{\sin\Theta} \qquad \textbf{(vii)}$$

$$\cos\sigma_2 = \frac{2\sin\theta^{inc}\cos\theta^{sca}\sin^2\frac{\Delta\varphi}{2} + \sin\Delta\theta}{\sin\Theta} \qquad \textbf{(viii)}$$

One can now define $\langle \underline{\mathbf{Z}}(\theta^{sca}, \varphi^{sca}; \theta^{inc}, \varphi^{inc})\rangle_\xi$ with $-\pi < \Delta\varphi \equiv \varphi^{sca} - \varphi^{inc} < \pi$.

$$\left\langle \underline{\mathbf{Z}}\left(\theta^{sca},\varphi^{sca};\theta^{inc},\varphi^{inc}\right)\right\rangle_{\xi} \equiv \mathbf{L}(\sigma_2)\left\langle F(\Theta)\right\rangle_{\xi}\mathbf{L}(\sigma_1) =$$

$$\begin{bmatrix} \langle F_{11}(\Theta)\rangle_{\xi} & C_1\langle F_{12}(\Theta)\rangle_{\xi} & -S_1\langle F_{12}(\Theta)\rangle_{\xi} & 0 \\ C_2\langle F_{12}(\Theta)\rangle_{\xi} & C_2C_1\langle F_{22}(\Theta)\rangle_{\xi} - S_2S_1\langle F_{33}(\Theta)\rangle_{\xi} & -C_2S_1\langle F_{22}(\Theta)\rangle_{\xi} - S_2C_1\langle F_{33}(\Theta)\rangle_{\xi} & -S_2\langle F_{34}(\Theta)\rangle_{\xi} \\ S_2\langle F_{12}(\Theta)\rangle_{\xi} & S_2C_1\langle F_{22}(\Theta)\rangle_{\xi} + C_2S_1\langle F_{33}(\Theta)\rangle_{\xi} & -S_2S_1\langle F_{22}(\Theta)\rangle_{\xi} + C_2C_1\langle F_{33}(\Theta)\rangle_{\xi} & C_2\langle F_{34}(\Theta)\rangle_{\xi} \\ 0 & -S_1\langle F_{34}(\Theta)\rangle_{\xi} & -C_1\langle F_{34}(\Theta)\rangle_{\xi} & \langle F_{44}(\Theta)\rangle_{\xi} \end{bmatrix} \quad \textbf{(xxiii)}$$

The variables C_1, S_1, C_2, and S_2 are given by:

$$\sin^2\Theta = \sin^2\Delta\theta + 4\cos\Delta\theta\sin\theta^{sca}\sin\theta^{inc}\sin^2\frac{\Delta\varphi}{2} - 4\sin^2\theta^{sca}\sin^2\theta^{inc}\sin^4\frac{\Delta\varphi}{2}$$

$$C_1 \equiv \cos 2\sigma_1 = 1,\ S_1 \equiv \sin 2\sigma_1 = 0,\ C_2 \equiv \cos 2\sigma_2 = 1,\ \textit{and}\ S_2 \equiv \sin 2\sigma_2 = 0 \quad \textit{if}\ \sin^2\Theta = 0;\quad \textit{otherwise}$$

$$\cos 2\sigma_1 = \cos^2\sigma_1 - \sin^2\sigma_1 = \frac{\left(2\sin\theta^{sca}\cos\theta^{inc}\sin^2\frac{\Delta\varphi}{2} - \sin\Delta\theta\right)^2 - \left(\sin\theta^{sca}\sin\Delta\varphi\right)^2}{\sin^2\Theta}$$

$$\sin 2\sigma_1 = 2\sin\sigma_1\cos\sigma_1 = \frac{-2\sin\theta^{sca}\sin\Delta\varphi\left(2\sin\theta^{sca}\cos\theta^{inc}\sin^2\frac{\Delta\varphi}{2} - \sin\Delta\theta\right)}{\sin^2\Theta}$$

$$\cos 2\sigma_2 = \frac{\left(2\sin\theta^{inc}\cos\theta^{sca}\sin^2\frac{\Delta\varphi}{2} + \sin\Delta\theta\right)^2 - \left(\sin\theta^{inc}\sin\Delta\varphi\right)^2}{\sin^2\Theta}$$

$$\sin 2\sigma_2 = \frac{-2\sin\theta^{inc}\sin\Delta\varphi\left(2\sin\theta^{inc}\cos\theta^{sca}\sin^2\frac{\Delta\varphi}{2} + \sin\Delta\theta\right)}{\sin^2\Theta} \quad \textbf{(xxiv)}$$

The final line of Eq. (xxiii) is the expression from MTL Eq. (11.3.2).

7. MODTRAN Incident and Scattering Angle

The scattering and incident angle couplets, (θ^{sca}, φ^{sca}) and (θ^{inc}, φ^{inc}), are defined for the photon trajectory. Within MODTRAN, the opposite convention is used. For example, when modeling single scatter solar, MODTRAN defines the incident ray, originating from the sun, by the direction to the sun. Similarly, the scattered ray is defined by the sensor pointing direction. Thus, the MODTRAN scattering and incident angle couplets, ($\theta_{\text{m}}^{\text{sca}}$, $\varphi_{\text{m}}^{\text{sca}}$) and ($\theta_{\text{m}}^{\text{inc}}$, $\varphi_{\text{m}}^{\text{inc}}$), are defined as follows:

$$\theta_m^{sca} = \pi - \theta^{sca} \quad ,\quad \varphi_m^{sca} = -\varphi^{sca} \quad ,\quad \theta_m^{inc} = \pi - \theta^{inc} \quad ,\quad \varphi_m^{inc} = -\varphi^{inc} \quad ,$$

$$\Delta\theta_m \equiv \theta_m^{sca} - \theta_m^{inc} = -\Delta\theta \quad ,\quad \Delta\varphi_m \equiv \varphi_m^{sca} - \varphi_m^{inc} = -\Delta\varphi \quad \textit{and} \quad \textbf{(xxv)}$$

$$\sin^2\Theta = \sin^2\Delta\theta_m + 4\cos\Delta\theta_m\sin\theta_m^{sca}\sin\theta_m^{inc}\sin^2\frac{\Delta\varphi_m}{2} - 4\sin^2\theta_m^{sca}\sin^2\theta_m^{inc}\sin^4\frac{\Delta\varphi_m}{2}$$

The variables C_1, S_1, C_2, and S_2 defined in terms of the MODTRAN angles are given by:

$$\cos 2\sigma_1 = \cos^2\sigma_1 - \sin^2\sigma_1 = \frac{\left(2\sin\theta_m^{sca}\cos\theta_m^{inc}\sin^2\frac{\Delta\varphi_m}{2} - \sin\Delta\theta_m\right)^2 - \left(\sin\theta_m^{sca}\sin\Delta\varphi_m\right)^2}{\sin^2\Theta}$$

$$\sin 2\sigma_1 = 2\sin\sigma_1\cos\sigma_1 = \frac{2\sin\theta_m^{sca}\sin\Delta\varphi_m\left(2\sin\theta_m^{sca}\cos\theta_m^{inc}\sin^2\frac{\Delta\varphi_m}{2} - \sin\Delta\theta_m\right)}{\sin^2\Theta}$$

$$\cos 2\sigma_2 = \frac{\left(2\sin\theta_m^{inc}\cos\theta_m^{sca}\sin^2\frac{\Delta\varphi_m}{2} + \sin\Delta\theta_m\right)^2 - \left(\sin\theta_m^{inc}\sin\Delta\varphi_m\right)^2}{\sin^2\Theta} \qquad \textbf{(xxvi)}$$

$$\sin 2\sigma_2 = \frac{2\sin\theta_m^{inc}\sin\Delta\varphi_m\left(2\sin\theta_m^{inc}\cos\theta_m^{sca}\sin^2\frac{\Delta\varphi_m}{2} + \sin\Delta\theta_m\right)}{\sin^2\Theta}$$

Comparing Eqs. (xxiv) and (xxvi), $C_i(\theta_m^{sca}, \varphi_m^{sca}; \theta_m^{inc}, \varphi_m^{inc}) = C_i(\theta^{sca}, \varphi^{sca}; \theta^{inc}, \varphi^{inc})$, and $S_i(\theta_m^{sca}, \varphi_m^{sca}; \theta_m^{inc}, \varphi_m^{inc}) = -S_i(\theta^{sca}, \varphi^{sca}; \theta^{inc}, \varphi^{inc})$ for $i = 1, 2$.

8. Single Scatter Solar

This document has focused on determining the general form of the ISM phase matrix. The single scatter solar radiance obtained after applying this transformation to the unpolarized solar irradiance with Stokes vector, $\boldsymbol{I}_0 = (I_0, 0, 0, 0)^T$, is illustrated here (note that the rotation matrix $\mathbf{L}(\pi - \sigma_1)$ has no effect on the unpolarized incident beam):

$$\mathbf{I}' = \left\langle \underline{\mathbf{Z}}\left(\theta^{sca}, \varphi^{sca}; \theta^{inc}, \varphi^{inc}\right)\right\rangle_\xi \mathbf{I}_0 = \mathbf{L}(\sigma_2)\langle F(\Theta)\rangle_\xi \mathbf{L}(\sigma_1)\mathbf{I}_0 = \mathbf{L}(\sigma_2)\langle F(\Theta)\rangle_\xi \mathbf{I}_0$$

$$= \begin{bmatrix} 1 & 0 & 0 & 0 \\ 0 & \cos 2\sigma_2 & -\sin 2\sigma_2 & 0 \\ 0 & \sin 2\sigma_2 & \cos 2\sigma_2 & 0 \\ 0 & 0 & 0 & 1 \end{bmatrix} \begin{bmatrix} \langle F_{11}(\Theta)\rangle_\xi & \langle F_{12}(\Theta)\rangle_\xi & 0 & 0 \\ \langle F_{12}(\Theta)\rangle_\xi & \langle F_{22}(\Theta)\rangle_\xi & 0 & 0 \\ 0 & 0 & \langle F_{33}(\Theta)\rangle_\xi & \langle F_{34}(\Theta)\rangle_\xi \\ 0 & 0 & -\langle F_{34}(\Theta)\rangle_\xi & \langle F_{44}(\Theta)\rangle_\xi \end{bmatrix} \mathbf{I}_0 \qquad \textbf{(xxvii)}$$

$$\mathbf{I}' = \begin{bmatrix} \langle F_{11}(\Theta)\rangle_\xi & \langle F_{12}(\Theta)\rangle_\xi & 0 & 0 \\ \cos 2\sigma_2 \langle F_{12}(\Theta)\rangle_\xi & \cos 2\sigma_2 \langle F_{22}(\Theta)\rangle_\xi & -\sin 2\sigma_2 \langle F_{33}(\Theta)\rangle_\xi & -\sin 2\sigma_2 \langle F_{34}(\Theta)\rangle_\xi \\ \sin 2\sigma_2 \langle F_{12}(\Theta)\rangle_\xi & \sin 2\sigma_2 \langle F_{22}(\Theta)\rangle_\xi & \cos 2\sigma_2 \langle F_{33}(\Theta)\rangle_\xi & \cos 2\sigma_2 \langle F_{34}(\Theta)\rangle_\xi \\ 0 & 0 & -\langle F_{34}(\Theta)\rangle_\xi & \langle F_{44}(\Theta)\rangle_\xi \end{bmatrix} \mathbf{I}_0$$

$$= \begin{bmatrix} \langle F_{11}(\Theta)\rangle_\xi \\ \cos 2\sigma_2 \langle F_{12}(\Theta)\rangle_\xi \\ \sin 2\sigma_2 \langle F_{12}(\Theta)\rangle_\xi \\ 0 \end{bmatrix} I_0$$

$$= \begin{cases} \begin{bmatrix} \langle F_{11}(\Theta)\rangle_\xi \\ \langle F_{12}(\Theta)\rangle_\xi \\ 0 \\ 0 \end{bmatrix} I_0 \quad if \quad \sin^2 \Theta = 0; \quad otherwise \\ \begin{bmatrix} \langle F_{11}(\Theta)\rangle_\xi \\ \left\{ \left(2\sin\theta^{inc} \cos\theta^{sca} \sin^2 \dfrac{\Delta\varphi}{2} + \sin\Delta\theta \right)^2 - \left(\sin\theta^{inc} \sin\Delta\varphi \right)^2 \right\} \dfrac{\langle F_{12}(\Theta)\rangle_\xi}{\sin^2 \Theta} \\ -2\sin\theta^{inc} \sin\Delta\varphi \left(2\sin\theta^{inc} \cos\theta^{sca} \sin^2 \dfrac{\Delta\varphi}{2} + \sin\Delta\theta \right) \dfrac{\langle F_{12}(\Theta)\rangle_\xi}{\sin^2 \Theta} \\ 0 \end{bmatrix} I_0 \end{cases} \quad \textbf{(xxviii)}$$